The Pennsylvania State University

The Graduate School

College of Earth and Mineral Sciences

**INTEGRATED TIME-LAPSE SEISMIC ANALYSIS OF THE TWO G-SAND
FACIES, POPEYE FIELD, OFFSHORE GULF OF MEXICO**

A Thesis in

Geosciences

by

Beth Yuvancic Strickland

Submitted in Partial Fulfillment
of the Requirements
for the Degree of

Master of Science

December 2003

I grant The Pennsylvania State University the non-exclusive right to use this work for the University's own purposes and to make single copies of the work available to the public on a not-for-profit basis if copies are not otherwise available.

Beth Yuvancic Strickland

The thesis of Beth Yuvancic Strickland was reviewed and approved* by the following:

Peter B. Flemings
Associate Professor of Geosciences
Thesis Advisor

Sridhar Anandakrishnan
Associate Professor of Geosciences

Charles Ammon
Associate Professor of Geosciences

Turgay Ertekin
Professor of Petroleum and Natural Gas Engineering

Peter Deines
Professor of Geochemistry
Associate Head for Graduate Programs and Research

*Signatures are on file in the Graduate School

ABSTRACT

The RM reservoir of the G-sand in the Popeye field (Green Canyon 116, Gulf of Mexico) exhibits amplitude dimming where water has replaced gas beneath the current gas-water contact in the massive facies. Above the current gas-water contact and in the overlying laminated facies, brightening is present. The RN reservoir displays dimming in both the massive and laminated facies due to water-sweep as gas is extracted from the reservoir and condensate forms around the A3 wellbore. Dimming related to compaction of sands is also imaged in the massive facies aquifer region east of the RM reservoir. Gassmann fluid substitution and reservoir simulation support downdip amplitude dimming and updip amplitude brightening, but some brightening in the laminated facies within the RM reservoir cannot be explained, and may be caused by inefficient water-sweep. The two facies are imaged by one seismic loop, but show different time-lapse effects on the base and the top of the seismic loop. The different seismic response of the laminated and massive facies indicates different drainage behavior from the two facies.

TABLE OF CONTENTS

LIST OF FIGURES

LIST OF TABLES

PREFACE

This thesis is composed of a primary research chapter and three appendices. The main chapter, "Integrated Time-lapse Seismic Analysis of the Two G-sand Facies, Popeye Field, Offshore Gulf of Mexico", is my individual research topic. I perform time-lapse seismic analysis of the Popeye Field in order to image differences in the G-sand reflection character after four years of production. This method allows the imaging of differences within the two G-sand facies, revealing different production characteristics between the two facies. The time-lapse differences are related to results from a reservoir simulation of the Popeye field performed by Eric Kuhl, and to Gassmann fluid substitution results, performed in collaboration with Tin-Wai Lee, in order to develop a drainage model for the field. This drainage model is strongly based on interpretations and understandings derived from the development of the geologic model, which is detailed in the next thesis chapter.

Appendix A (pages 37-50) details the derivation and application of Weiner match filters. I then present the application of the match filter on individual seismic traces.

Appendix B (page 51 and insert in back pocket) is a joint collaboration with Tin-Wai Lee. Gassmann fluid substitution modeling was performed at four well locations in Popeye field, as such modeling is relevant to the separate research of both individuals. This appendix also appears as an appendix to the Master's thesis of Tin-Wai Lee.

Appendix C (page 52 and insert in back pocket) is the paper "Integration of Geologic Model and Reservoir Simulation, Popeye Field, Green Canyon 116". It is the result of multi-disciplinary group collaboration of the Petroleum Geosystems Initiative Team 2 members, of which I am a part. This paper fully characterizes the G-sand at Popeye field, presents a geologic model, and details how geologic uncertainties inherent

in the geologic model affect predicted production modeled in a reservoir simulation. This paper was presented and published at the 53rd annual meeting of the Gulf Coast Association of Geological Societies in Baton Rouge, Louisiana. Geosystems team-members Eric Kuhl, Tin-Wai Lee, and Benjamin Seldon collaborated with me on this paper; we were advised by Peter Flemings and Turgay Ertekin.

ACKNOWLEDGEMENTS

INTRODUCTION

Production of pore fluids from a reservoir can affect pressure, temperature, and pore-fluid composition, all of which influence the acoustic properties of the rocks (Nur, 1989; Wang et al., 1991; Batzle and Wang, 1992; Wang, 2001). Time-lapse (4D) seismic analysis is used to monitor the migration of hydrocarbons and other fluids during production or injection, to image and predict bypassed pay, to map reservoir compartments, to develop strategies to accelerate production, and to determine if faults transmit fluids (Koster et al., 2000; Fanchi, 2001; Lumley, 2001, 2002). Time-lapse seismic analysis has also been integrated with reservoir simulation to quantitatively describe amounts and locations of produced reserves (Lygren et al., 2003; Waggoner et al., 2003) and to depict saturation changes due to production (Sengupta et al., 2003).

Recent studies have imaged fluid-contact movement and quantified the repeatability of seismic surveys taken at different times and with different azimuths. Behrens et al. (2001) demonstrated that datasets not acquired for time-lapse purposes can image production-related differences and find bypassed reserves. Burkhart et al. (2000) imaged seismic changes caused by five years of production at the South Timbalier Block 295 field. Pressure reduction due to production within the K8 reservoir resulted in gas-cap expansion, and water-sweep of oil caused dimming of the K40 reservoir updip of the original oil-water contact. Hoover et al. (1999) used the time-lapse differences imaged by Burkhart et al. (2000) to refine the K40 sand geologic model at the South Timbalier Block 295 field. Kaleta (2001) examined gas production from two reservoir sands at Kileaua field (Green Canyon 6), and interpreted amplitude dimming near a producing well as an increase in condensate saturation due to a 9.65 MPa pressure drop. Swanston et al. (2003) determined that seismic surveys of similar

orientation used in a time-lapse analysis of Bullwinkle field (Green Canyon 65) produced the best results.

This analysis of the Popeye field is performed with poststack data. We utilize a post-stack normalization approach, developed by Burkhart et al. (2000) and utilized by Swanston et al. (2003). After normalization we difference amplitude extraction maps to image contact movements in the two G-sand facies, gas expansion due to pressure reduction, and dimming associated with aquifer compaction. These results are compared to reservoir simulation outputs and fluid-substituted synthetic seismic traces in order to produce a drainage model for the Popeye field.

POPEYE FIELD

Regional Setting

The Popeye field is located on the Gulf of Mexico continental shelf (Fig. 1). It is in the northern, proximal, part of a larger minibasin that includes the Genesis field (Green Canyon 205/161) on the western flank (Rafalowski et al., 1996; Varnai et al., 1998). Gas and condensate are produced from the Late Pliocene G-sand, at 3500 m depth. The field is on the southern, downthrown, side of a regional growth fault (Dean et al., 2000). Smaller faults and a channel compartmentalize the G-sand into four reservoirs: the RM and RN in the west and the RA and RB in the northeast (Fig. 2). Large negative seismic amplitudes delineate gas accumulations in the structural highs of these compartments (Figs. 2, 3); the gas-water contacts are generally parallel to depth-structure contours.
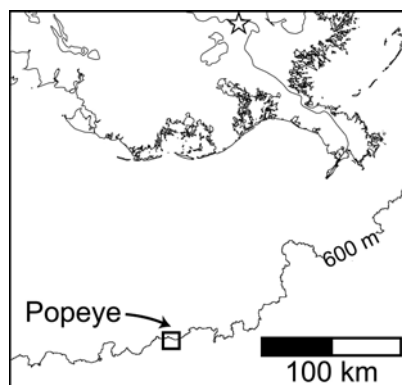
Figure 1: Popeye Field is located 225 km southwest of New Orleans, LA (marked with star), in 600 m water depth.

_____

The G-sand

The G-sand consists of a laminated facies (G_L) and an underlying massive facies (G_M) that average 23 m in total gross thickness (Fig. 4). The G_L is a very fine-grained, high porosity (25 – 30 %) sandstone that is interbedded with silty shale. The G_M is a fine-grained sandstone with no internal structure and high porosity (30 – 35 %). It has a clean, blocky log signature with a sharp base (Fig. 4). The G_M facies are an amalgamated sheet sand, overlain by the levee-overbank deposits that comprise the G_L facies (Appendix C).

In seismic data, the G-sand is imaged by a trough at the top of the G_L and a peak at the base of the G_M in zero-phase data (Fig. 4). In the RM compartment, the thick G_L shales upwards, and produces synthetic seismograms that show a broad, asymmetric trough whose minima is below the top of the G_L and a narrow peak that aligns with the base of the G_M (Fig. 4). In the RN reservoir there is little impedance contrast between the G_L and the overlying shales, and strong contrasts between the G_M and underlying shales (Fig. 4). As a result, the G_L produces a weak negative reflection at the top of the

G-sand, while the G_M base produces a strong positive reflection. The sharp G-sand base contact produces large amplitude reflections in reservoirs (Fig. 4). The G-sand Base amplitude reflection is greater than the G-sand Top reflection throughout the field (Figs. 5A, 6A).
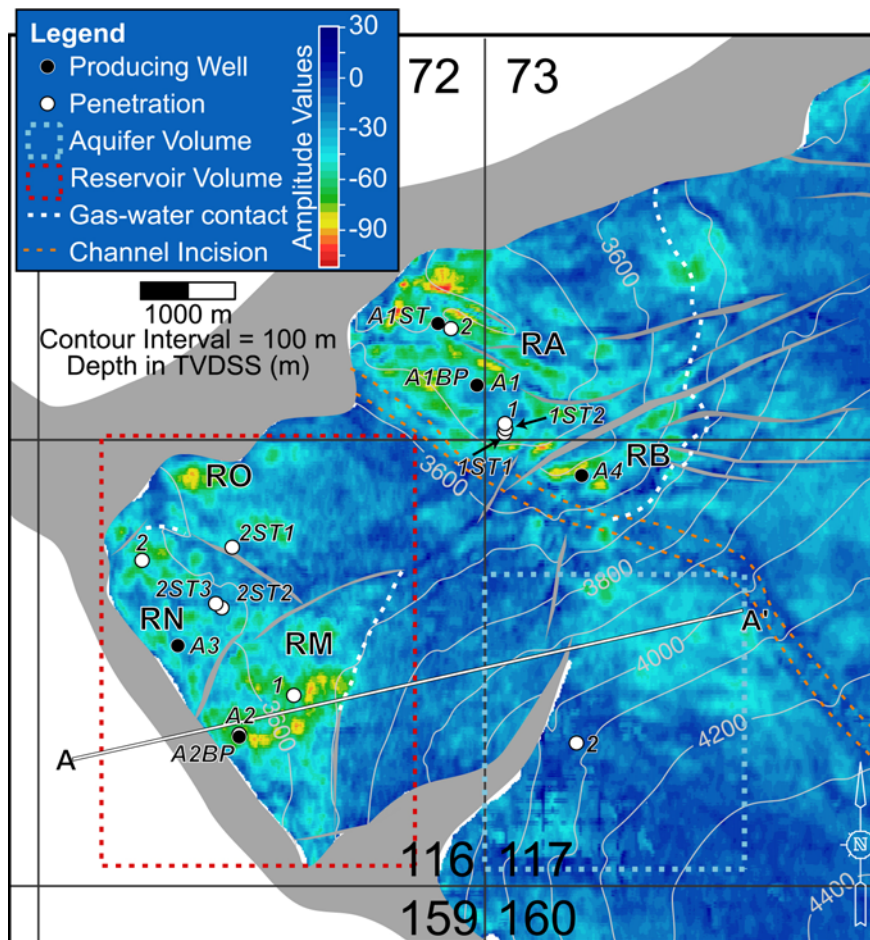
Figure 2: Amplitude-extraction of the G-sand at Popeye Field, overlain with depth-structure contours in true-vertical subsea depth (TVDSS) to the top of the G-sand. The Reservoir and Aquifer Volumes used in normalizations are outlined. Cross-section A-A' is displayed in Figure 3.
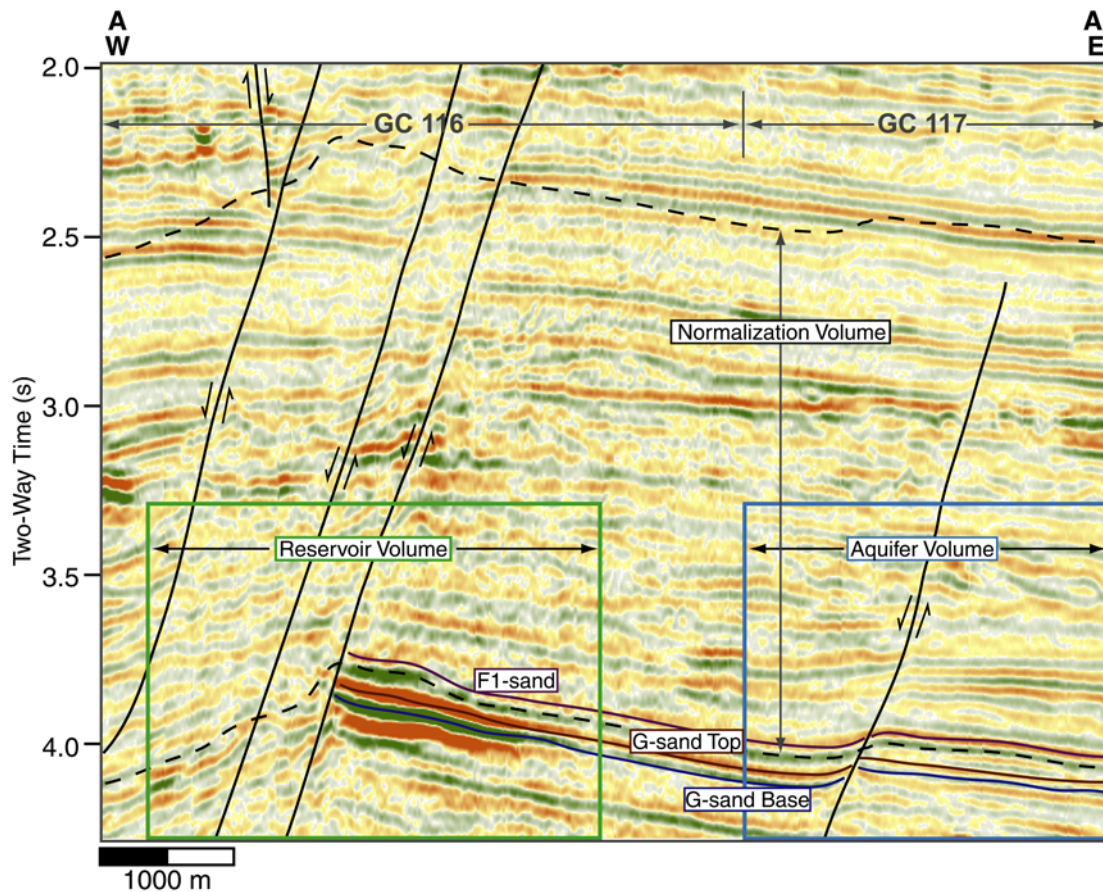
Figure 3: Seismic cross-section showing the Normalization Volume (1500 ms window), the Reservoir Volume, the Aquifer Volume, and interpreted horizons. Reds are negative values (troughs) and greens are positive values (peaks). The Normalization Window is used to derive the spatially variant match filters and to amplitude balance the two datasets. Line A-A' is located in Figure 2.

3D Seismic Surveys

We consider two east-west oriented seismic datasets: the first was acquired in 1990 and the second in 2000, after four years of production. The 2000 data were reprocessed to eliminate long-offset receivers, so that they were similar to the 1990 data. The reflection coefficients of the 2000 survey were integrated into a running-summation format (Deshpande et al., 1997; Pfeiffer et al., 2000) whereas the 1990

survey is in zero-phase form. Tables 1 and 2 summarize the acquisition and processing

parameters of the two datasets.

_____

Table 1: Acquisition parameters for the two seismic surveys.

	1990 survey	**2000 survey**
Orientation	90°	90°
Acquisition technique	Multivessel, dual airgun array, flip-flop, 2 streamers	4 streamers
Fold	40	48
Source(s)	Dual airgun array	Airgun
Source volume	3762 in^3	4180 in^3
Shot interval	25 m (82 ft)	37.5 m (123 ft)
Group (receiver) interval	25 m (82 ft)	25 m (82 ft)
Cable length	4000 m (13,123 ft)	7200 m[a] (23,622 ft)
Sampling interval	2 ms[b]	2 ms[b]
Record length	8 s	13 s
Final bin size	12.5 x 20 m (41 x 66 ft)	25 x 20 m (82 x 66 ft)

[a] Trimmed to 5800 m when reprocessed
[b] After digitization, survey was resampled to 4 ms.

_____
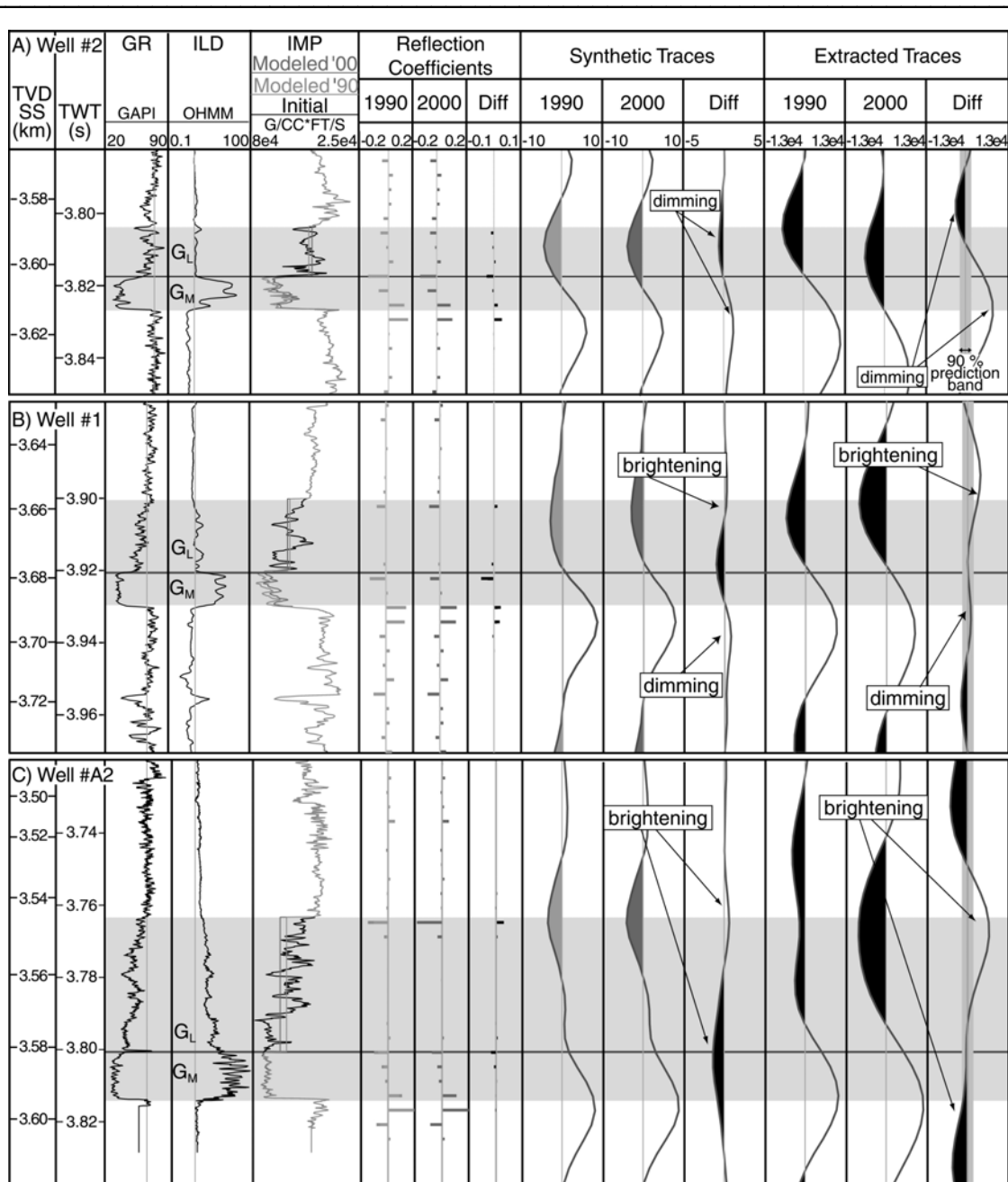
Figure 4: Gamma-ray (GR) and resistivity (ILD) well logs, impedance logs (IMP), reflection coefficients (RFC) derived from the impedance logs, and synthetic and extracted seismic traces from the 1990 and normalized 2000 datasets in the time domain in A) Well #2, B) Well #1 and C) Well #A2. We model the effective (averaged) acoustic properties of the G_L facies in RFCs and synthetic traces. Well locations are shown in Figures 2, 5, and 6.
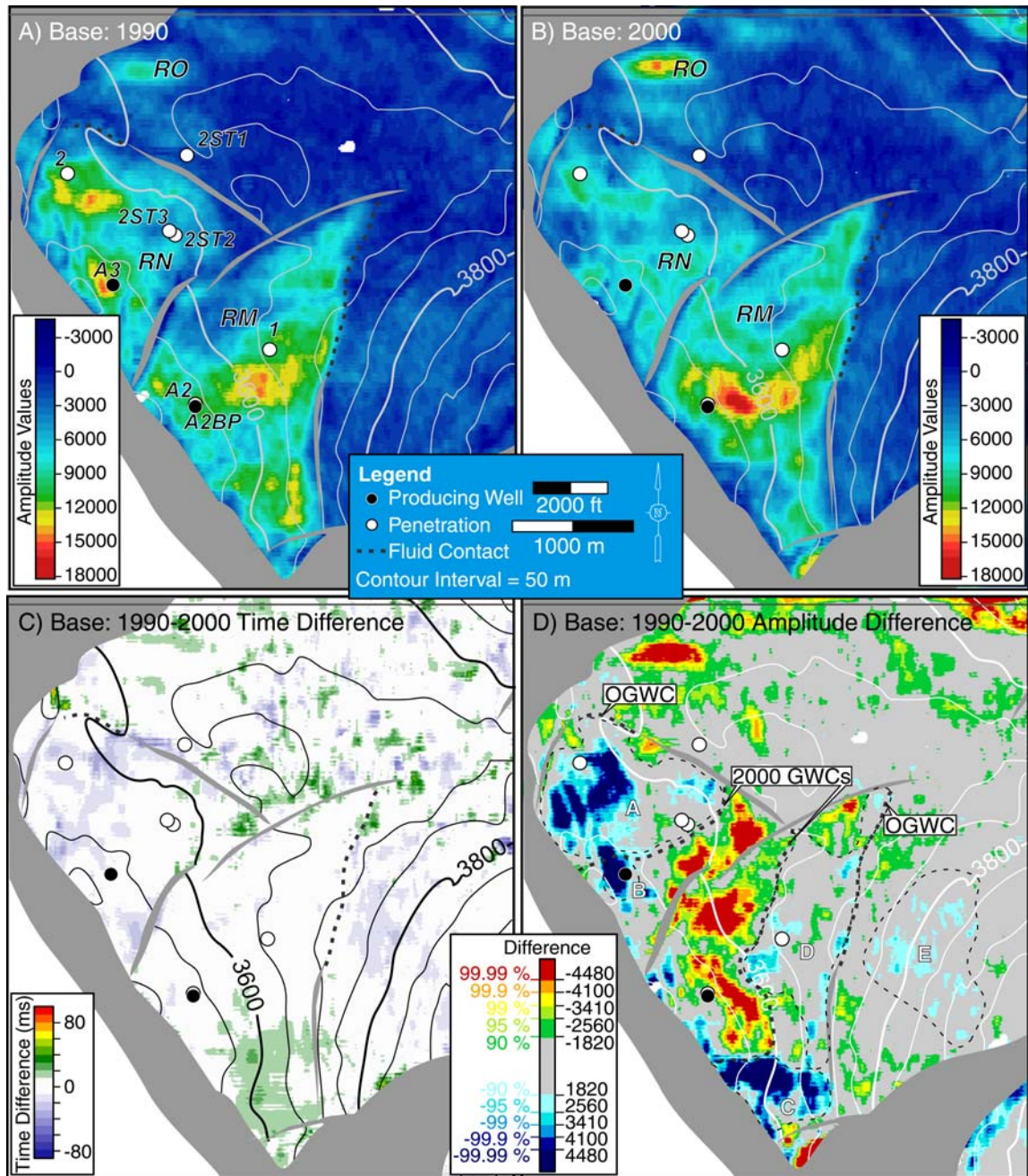
Figure 5: Amplitude maps constructed on the G-sand Base within the A) 1990 and B) 2000 datasets. C) Time-difference between the 1990 and 2000 G-sand Base horizons. D) Amplitude-difference map of G-sand Base amplitudes, calculated by subtracting the 2000 Base amplitude maps from the 1990 Base amplitude map. Difference values are displayed in terms of the prediction bands derived with the Normalization Volume cross-plot (Fig. 8A), indicating the statistical significance of differences. Areas A, B, C, D and E are explained in text.
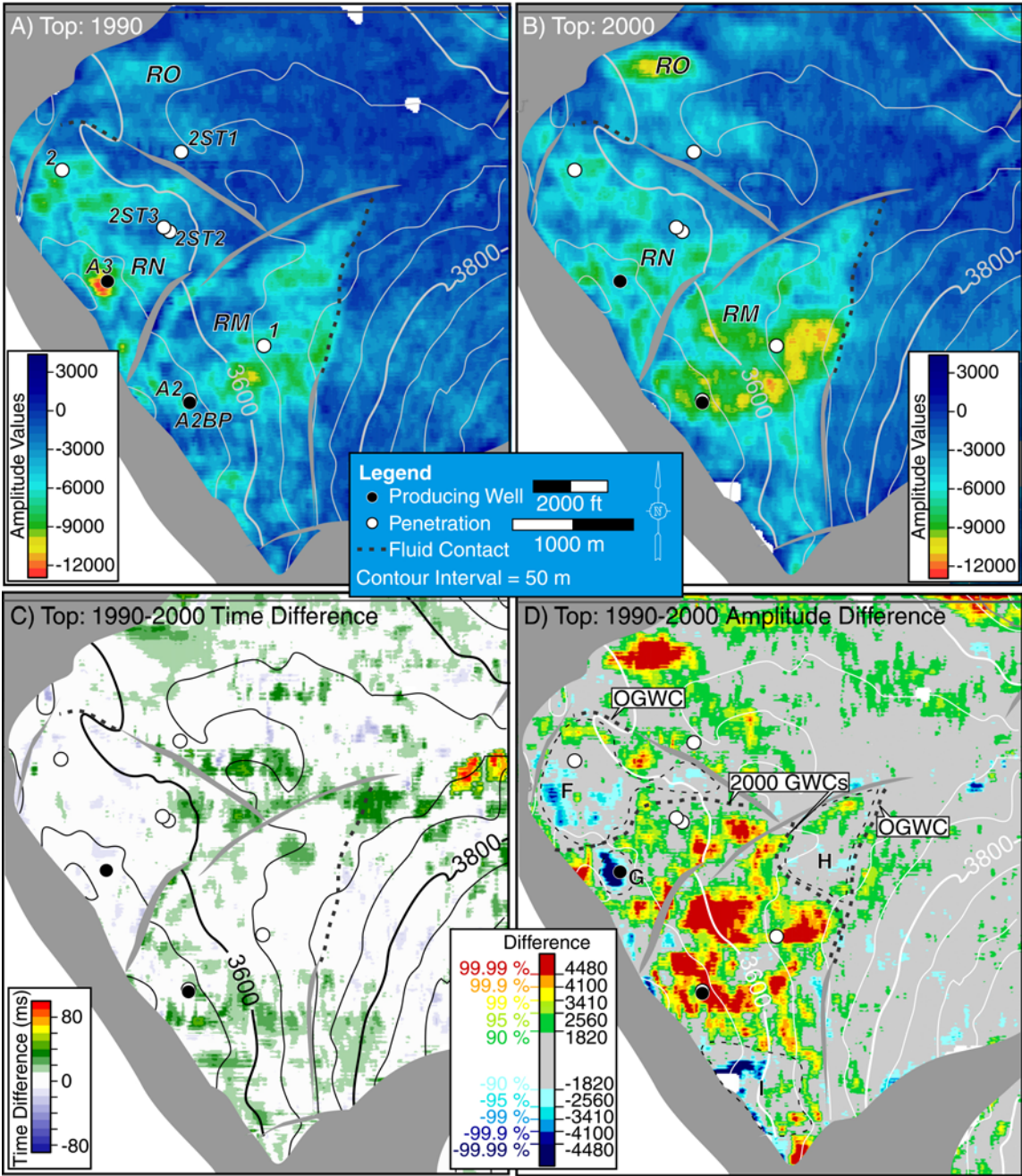
Figure 6: Amplitude maps constructed on the G-sand Top within the A) 1990 and B) 2000 datasets. C) Time-difference between the 1990 and 2000 G-sand Top horizons. D) Amplitude-difference map of G-sand Top amplitudes constructed and displayed as described in Figure 5. Areas F, G, H and I are explained in text.

Table 2: Processing and reprocessing flows for the two seismic surveys.

1990 survey	Reprocessed 2000 survey
Navigation merge	Bin data
Designature	Remove detectable spikes
Amplitude recovery and trace editing	Normal moveout (NMO) correction
Deconvolution (320 ms operator)	3D Dip-moveout (DMO)
3D binning	Inverse NMO
3D DMO velocity analysis (800 x 800 m)	Infill traces
Normal moveout correction	NMO
3D DMO	Resample CDP gathers from 150 m offset to 50 m offset spacing
3D stack (12.5 x 40 m bins)	Inverse NMO
Cross-line interpolation (12.5 x 20 m bins)	Transform from time to frequency domain
Two pass migration	Circular migration, first in crossline direction, then in inline direction
Bandpass filter and final scaling	Integrate RFCs
	Convert data from frequency to time domain
	Remove gain applied during migration
	Bandpass filter, NMO, and final stack

NORMALIZATION METHODOLOGY

We performed poststack normalization to minimize acquisition and processing differences between datasets (Ross et al., 1996). The normalization flow incorporated regridding the datasets to a common CDP spacing (Berni et al., 1997; Rickett and Lumley, 1998; Burkhart et al., 2000; Johnston et al., 2000; Rickett and Lumley, 2001; Swanston et al., 2003), phase rotation (Ross et al., 1996), static shifts in time and space (Rickett and Lumley, 1998; Burkhart et al., 2000; Johnston et al., 2000; Behrens et al., 2001; Swanston et al., 2003), match filtering (Rickett and Lumley, 1998; Burkhart et al.,

2000; Behrens et al., 2001; Swanston et al., 2003) and amplitude balancing of the two volumes (Ross et al., 1996; Rickett and Lumley, 1998; Burkhart et al., 2000; Swanston et al., 2003) (Table 3).

_____

Table 3: Cross-equalization flow to normalize 1990 and 2000 datasets.

Process	Parameters
Regrid	1990 CDPs to 2000 CDP spacing
Bandpass filter	Corner frequencies of 0-8-20-30
Phase rotation	90° rotation of 2000 data
Static shifts	2000 data shifted: 16 ms down 50 m south 40 m west
Match filter	Individual 400 ms filters Derived in 1500 ms window above G-sand Spatially variant
Amplitude balancing	Compared Normalization Volumes

_____

We used a double interpolation method (Landmark Graphics Corporation, 2003) to regrid (in inline and crossline directions) the more densely populated 1990 dataset to the CDP locations of the more sparsely populated 2000 dataset. The two datasets were bandpass filtered and the 2000 data were phase rotated 90° to better match the phase of the 1990 data. To determine the optimal static shift, the 1990 dataset was cross-correlated with the 2000 dataset; the 2000 dataset was shifted in time and position (Table 3). Weiner match filters (Robinson and Treitel, 1967) (Appendix A) were subsequently used to correct differences in phase, time, frequency, and amplitude between datasets. The spatially variant match filters were derived in a 1500 ms window above the G-sand reflection (Normalization Volume, Fig. 3) and applied to corresponding traces within the 2000 data.

The amplitude distribution within the Normalization Volumes were compared; the 2000 amplitude distribution was then normalized to the 1990 distribution using the equation

$$\hat{y}_i = \left(\frac{\sigma_x}{\sigma_y}\right)\left(y_i - \left(\bar{y} - \frac{\sigma_y \bar{x}}{\sigma_x}\right)\right) \tag{1}$$

where y_i are incremental samples of the 2000 dataset, σ_x and σ_y are the standard deviations of the 1990 (x) and 2000 (y) datasets, $\bar{x}$ and $\bar{y}$ are the means of the datasets and $\hat{y}_i$ are the incremental samples of the normalized 2000 dataset (Table 4). This equation also describes the geometric-mean regression line (GMRL) from Burkhart et al. (2000), later used in cross-plots. After amplitude balancing, the Normalization Volumes contain similar averages and distributions of amplitude values (Table 5), which allows direct comparison of the 1990 (x) and the normalized 2000 ($\hat{y}$) dataset.

STATISTICAL ANALYSIS

The correlation between the datasets is evaluated with the correlation coefficient, r, where

$$r = \frac{\sigma_{x\hat{y}}}{\sigma_x \cdot \sigma_{\hat{y}}}, \tag{2}$$

where $\sigma_{x\hat{y}}$ is the covariance of x and $\hat{y}$ (Burkhart et al., 2000). Correlation is also expressed with the RMS ratio (RR), where

$$RR = \frac{RMS(x - \hat{y})}{\frac{1}{2}(RMS(x) - RMS(\hat{y}))} \tag{3}$$

and

Table 4: Nomenclature.

x	Set of all values in 1990 data
x_i	Value of x at i[th] location
$\bar{x}$	Mean of x
σ_x	Standard deviation of x
y	Set of all values in 2000 data
y_i	Value of y at i[th] location
$\bar{y}$	Mean of y
σ_y	Standard deviation of y
$\hat{y}$	Set of all values in 2000 data after normalization
$\hat{y}_i$	Value of $\hat{y}$ at i[th] location
$\sigma_{\hat{y}}$	Standard deviation of $\hat{y}$
$\sigma_{x\hat{y}}$	Covariance between x and $\hat{y}$
r	Correlation coefficient
σ_p	Scatter of data from GMRL in cross-plot
BCF	Billion cubic feet
G_L	Laminated facies of the G-sand
G_M	Massive facies of the G-sand
GMRL	Geometric mean regression line
GWC	Gas-water contact
MMSCF	Million standard-cubic feet
MMSTB	Million stock-tank barrels
OGWC	Original gas-water contact
$P_{reservoir}$	Reservoir pressure (MPa)
RFT	Repeat formation test
RMS	Root-mean square
RR	RMS ratio
S_g	Gas saturation (%)
TVDSS	True-vertical depth below the sea-surface
V_p	P-wave velocity through rock
Z	Acoustic impedance of rock
% ΔZ	Per cent change in acoustic impedance
ΔS_g	Gas saturation change
ρ_{bulk}	Bulk rock density
Φ_{sand}	Porosity of sand

Table 5: Filter-derivation window statistics before and after amplitude balancing.

	Mean	Standard deviation
1990 window (x)	0.6807	1104.3406
2000 window (y)	-0.0581	906.2211
2000 window ($\hat{y}$)	0.8214	1104.3406

$$RMS(x) = \sqrt{\frac{\sum_{i=1}^{n}\left(x_i^2\right)}{n}} \tag{4}$$

and the number of samples in *x* is defined by n within the interval of *i* =1 to *n* (Kragh and Christie, 2001). The RMS ratio is related to the correlation coefficient through

$$r = 1 - \frac{1}{2}RR^2 \tag{5}$$

when the datasets have equivalent signal-to-noise ratios (Swanston, 2001).

STATISTICAL COMPARISON OF VOLUMES

To gauge the success of the normalization, we compare the statistical properties of the 1990 and 2000 datasets within the Aquifer Volume and the Reservoir Volume. The Aquifer Volume is defined as the regions of the G-sand with continuous reflections downdip of the reservoirs; the Reservoir Volume incorporates the RM, RN, and RO reservoirs (Fig. 2). The 1990 and 2000 datasets are compared with a single correlation coefficient and with a 16-ms moving window of correlation (Fig. 7). The correlation of the Aquifer and Reservoir Volumes increases after each normalization step. The final Aquifer Volumes demonstrate greater correlation than the final Reservoir Volumes (0.74 vs. 0.61) (Fig. 7).
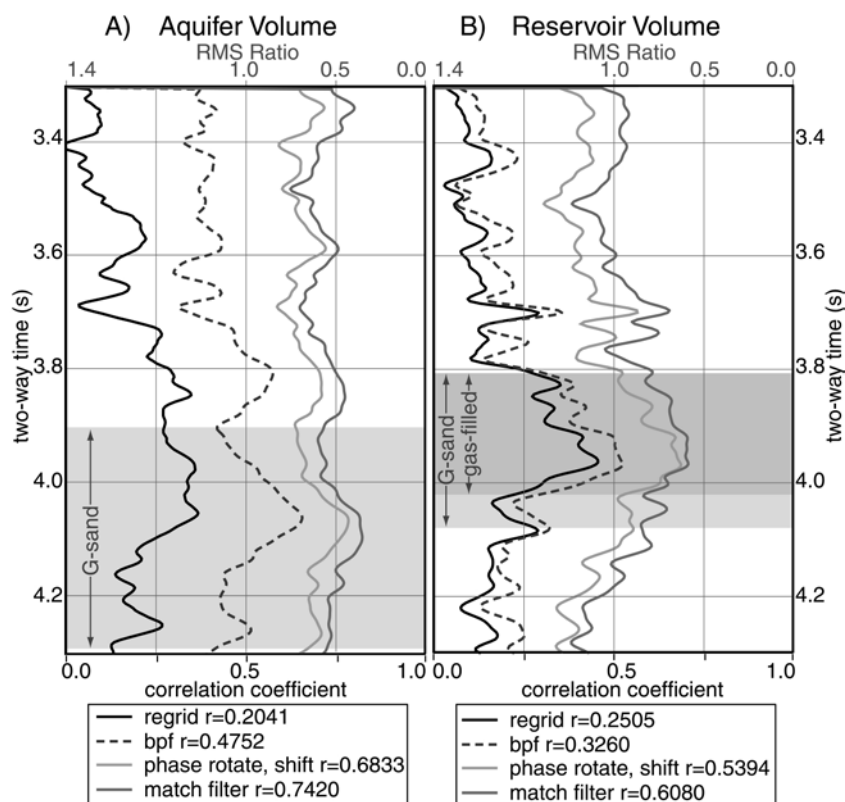
Figure 7: Cross-correlation (equation 2) on the primary axis and RMS ratio (equations 3 and 5) on the secondary axis, calculated over a 16-ms moving interval within the A) Aquifer Volume and B) the Reservoir Volume. Plots compare the 1990 and 2000 aquifer volumes after regridding (regrid), bandpass filtering (bpf), 90° phase rotation and static shifts (phase-rotate and shift), and after application of spatially-variant match filters (match filter) (Table 4). Grey regions indicate extent of the G-sand within the respective volumes. Dark grey region within (B) represents the vertical extent of gas-saturated sand.

Initially, the Aquifer Volume has lower correlation than the Reservoir Volume (0.20 vs. 0.25), but the Aquifer Volume correlation dramatically increases with the application of the bandpass filter (0.48 vs. 0.33) (Fig. 7). The increased correlation between the Aquifer Volumes may be because this volume has fewer faults than the Reservoir Volume (Fig. 3). The 2000 data image faulted offsets more clearly than the 1990 data; this difference is apparent even after the two datasets are bandpass filtered to the same frequency bandwidth. The low correlation between the two Reservoir

Volumes may also be attributed to production-related changes. The match filter application improves correlation between the 1990 and 2000 datasets similar amounts in each volume comparison (~10 % increase) (Fig. 7). The volume comparisons contain higher correlations within time intervals that incorporate the G-sand (Fig. 7). Swanston et al. (2003) interpreted that a similar trend at Bullwinkle Field was due to improved signal-to-noise ratios in regions where larger amplitudes are present.

We cross-plot values from the Normalization Volume used to derive the spatially variant match filters (Fig. 8A). The 1990 and 2000 datasets have the same averages and distributions of amplitude values (Table 5), therefore the geometric-mean regression line (GMRL , Equation 1) has a slope of one (Fig. 8A). This indicates that the 1990 and 2000 datasets are amplitude balanced. The prediction bands overlain on the cross-plot are defined by the scatter of the data (σ_p) from the GMRL; there is little scatter of data outside of the 99.99 % prediction bands (Fig. 8A). There is a 90 % probability that a random sample will lie within the 90 % prediction band (Burkhart et al., 2000). Data from the F1-sand (Fig. 3) within the Reservoir Volume are plotted in the same manner. The GMRL of the F1-sand horizon has a slope lower than that of the Normalization Volume; however, there is little scatter of the F1-sand horizon outside of the prediction bands derived from the Normalization Window cross-plot (Fig. 8B).

The G-sand Base cross-plot has a GMRL similar to that of the Normalization Volume GMRL (Fig. 8C). Data are scattered outside both of the 99.99 % prediction bands. We interpret this to reveal that the G-sand Base horizon both brightens and dims between 1990 and 2000. The G-sand Top cross-plot shows data scatter primarily below the 99.99 % prediction band; additionally, the Top GMRL has a slope higher than that of the Normalization Volume GMRL (Fig. 8D). These both indicate that the G-sand Top is brightening through time.
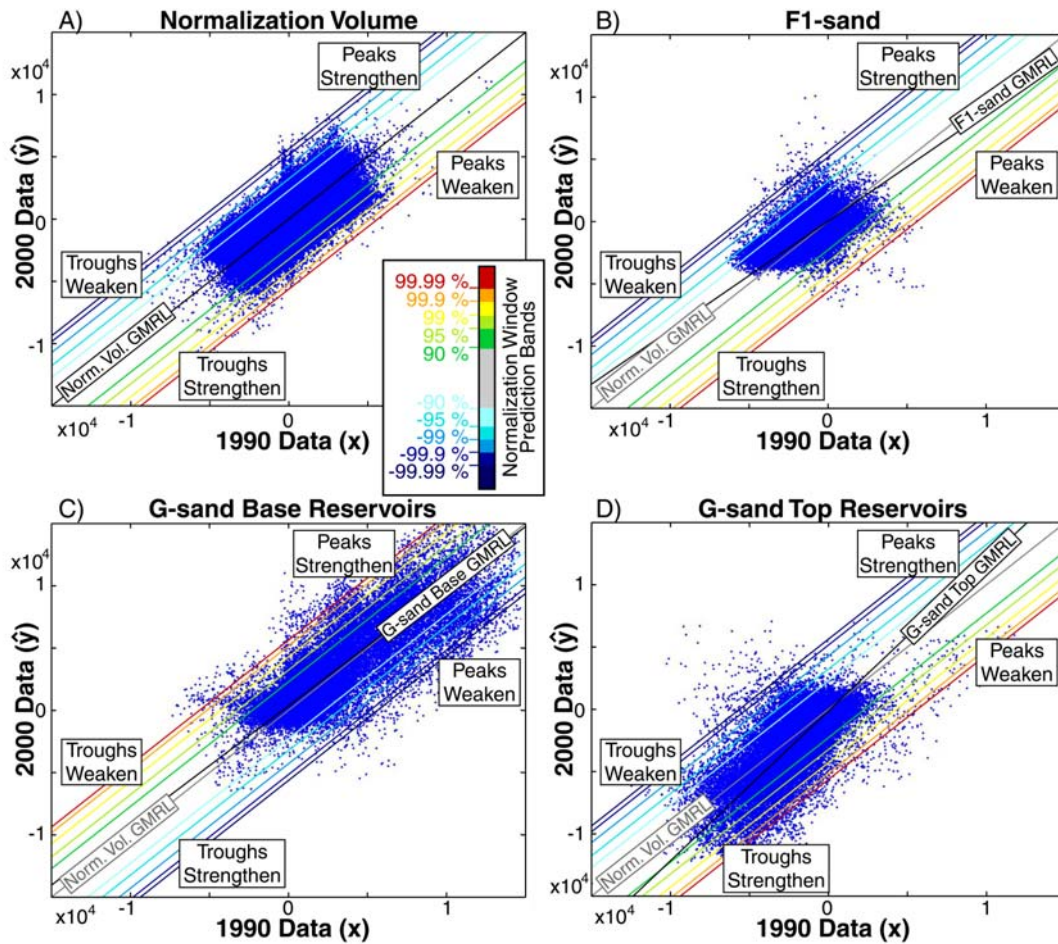
Figure 8: Cross-plot of 1990 (x) and 2000 amplitudes ($\hat{y}$) taken from the A) Normalization Volume (Fig. 3), and from the B) F1-sand Horizon, C) G-sand Base Horizon and D) G-sand Top Horizon, all within the Reservoir Volume. Colored lines on cross-plots are derived using the scatter of the Normalization Volume cross-plot. A probability of 90 % exists that a random sample from the cross-plots will fall within the 90 % prediction bands, if no changes in rock or fluid properties have occurred. The G-sand Base prediction bands are opposite in color than the other plots because the Base reflection is a peak; the F1-sand and G-sand Top reflections are troughs.

AMPLITUDE-DIFFERENCE MAPS

The Base amplitude-difference map exhibits dimming in the downdip regions of the RN and RM reservoirs (Fig. 5D). The dimming is particularly significant in the RN reservoir and the southern RM reservoir (Areas A, B, and C, Fig. 5D), where the many amplitude values outside the 99.99 % prediction bands most likely record changes in rock and fluid properties. Elsewhere (Area D, eastern Area A), the amplitude difference is smaller, with a 99 % probability that the change is not due to noise in the data. Brightening (> 99.99 %) occurs in the eastern portion of the RN reservoir and the updip (western) area of the RM reservoir (Fig. 5D).

The Top amplitude-difference map displays weak dimming (90 – 99 %) within the downdip area of the RN reservoir (Area F, Fig. 6A). This dimming is less than that of Area A within the Base amplitude-difference map (90 – 99 % vs. > 99.99 %). Brightening occurs in the updip and eastern areas of the RN reservoir. The majority of the RM reservoir brightens greatly (> 99.99 %), with a small area of scattered minor dimming in the northwest (Area H, Fig. 6D). The southern area of the reservoir shows some dimming, surrounded by an area of no change.

The RO reservoir exhibits brightening (> 99.99 %) in both Top and Base amplitude-difference maps (Figs. 5D, 6D). Aquifer regions show low magnitude (≤ ±90 %), scattered dimming and brightening in the Top amplitude-difference map (Fig. 6D). The aquifer region west of the RM reservoir (Area E) dims (90 – 95 %) within the Base difference map (Fig. 5D).

RESERVOIR SIMULATION RESULTS

A reservoir simulation was performed to model production-related changes in saturation, gas-in-place, and pressure. The rock properties, structure and isopach maps used in the reservoir model are described in Appendix C. The G_M and G_L were modeled as two separate layers and as a result, the gas-water contacts (GWCs) in each layer migrate updip at different rates (Figs. 9C, 9D, 10).

Sand thickness in both G_M and G_L facies varies laterally; the net sand in both facies thickens to the western margins of both reservoirs (Figs. 9A, 9B). The amount of gas initially in place is controlled by sand thickness, pressure, and other rock properties (see Appendix C for a complete description). Because reservoir pressures do not vary significantly, the amount of gas-in-place is strongly dependent on sand thickness. The largest volumes of initial gas-in-place occur in the western margins of the RM and RN reservoirs, where net sand is thickest (Figs. 9A, 9B, 9C, 9D).

During production, as the contacts migrate between the initial and 2000 positions, water replaces gas within pore spaces. The simulation predicts GWC movement parallel to structure (compare Figs. 9C, 9D with contours on Fig. 5), because of constant rock properties within each facies (Appendix C). The GWCs within the RM and RN/RO reservoirs move west and updip between 1996 and 2000 (Figs. 9E, 9F, 10).

Areas between initial and 2000 GWCs, where water has replaced gas in the pore space, correspond to regions of largest gas-in-place difference (Figs. 9E, 9F). Because the amount of gas-in-place is dependent on net sand thickness, the thicker reservoir areas have larger gas-in-place differences (Fig. 9C, 9D, 9E, 9F, 10C). The southern RM reservoir has more than 250 MMSCF/reservoir-simulation block removed from each layer in water-swept zones between 1996 and 2000 (Fig. 9C, 9D, 9E, 9F, 10C). The

water-swept areas of the RN and RO reservoirs have small differences because thin reservoir sands limit the amount of gas initially in place (Figs. 9C, 9D, 9E, 9F, 10F). The area to the north of the RN reservoir, updip of the 2000 GWC, exhibits no change in the amount of gas-in-place because the area has not been swept by water (Fig. 9D).

The amount of gas-in-place decreases updip of the 2000 GWCs (Figs 9C, 9D, 10C, 10F). This is due to production-driven pressure reduction causing gas expansion of the updip reserves (Figs. 9C, 9D). In these regions, a smaller amount of gas occupies the same pore space.

FLUID SUBSTITUTION

We predict acoustic changes using Gassmann fluid substitution (Gassmann, 1951). Differences due to production within the G_M and G_L facies are generalized into three regions: 1) downdip of the OGWC, in the aquifer region of the G-sand, 2) the area where water replaces gas as the GWC moves updip, and 3) updip of the 2000 GWC, where gas saturation does not change. We model that all three regions experience the same average pressure change of 15.17 MPa, and that when water-swept, the initial to residual gas saturation decreases from 90 to 22 % in the G_M facies and from 80 to 23 % in the G_L facies (Table 6). Initial conditions are based on petrophysical measurements and 2000 conditions are averaged from reservoir simulation.
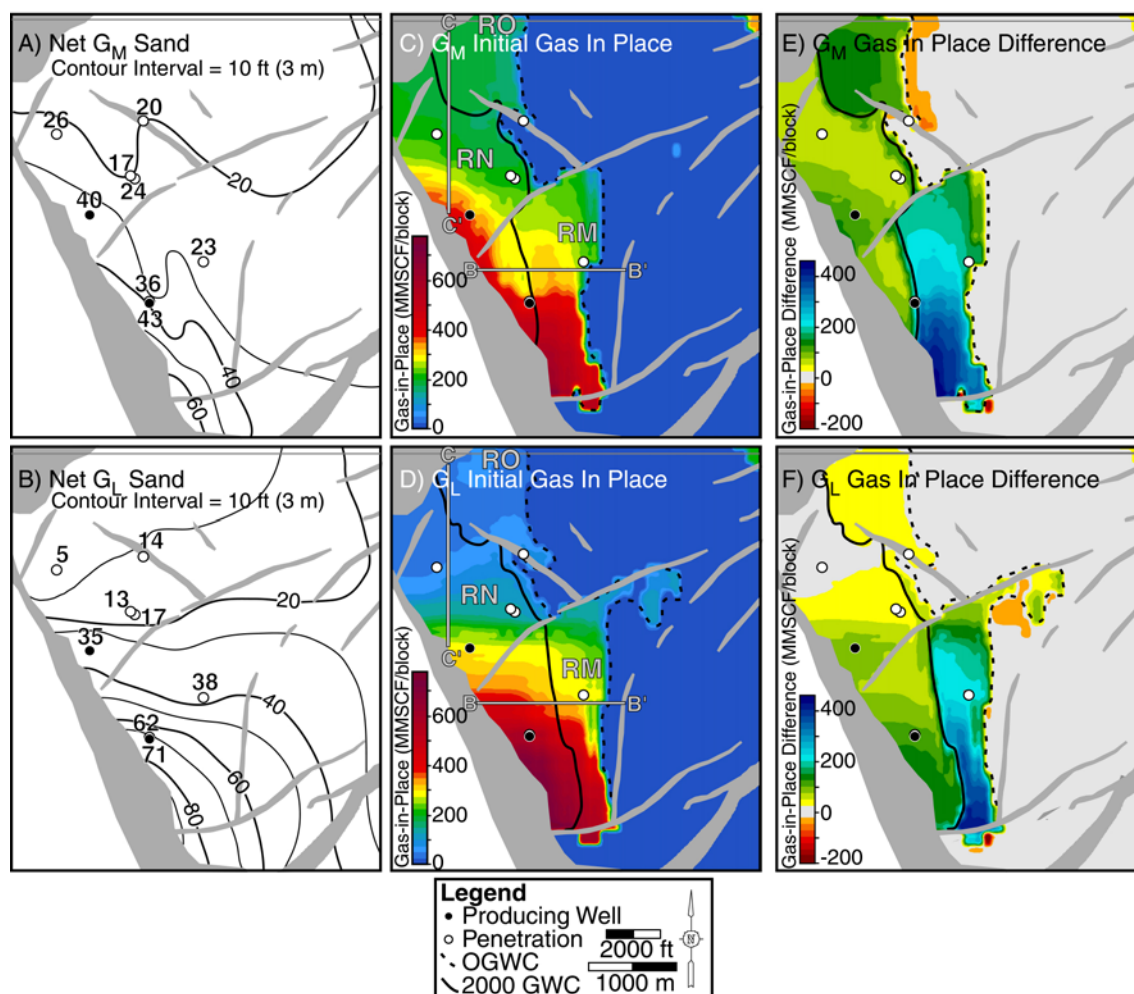
Figure 9: Net sand distributions from the A) G_M facies and the F) G_L facies (from Appendix C) were used in the reservoir simulations. Initial reservoir simulation gas-in-place in the C) G_M layer and the D) G_L layer is calculated within each reservoir simulation grid-block, which average 100 by 100 m. The differences between initial and 2000 gas-in-place are calculated by subtracting 2000 gas-in-place maps from initial gas-in-place maps for the E) G_M layer and F) G_L layer. Both E and F exhibit some areas of negative difference, which is due to the expansion of gas into downdip, water-saturated areas as reservoir pressure decreases. Original and 2000 GWCs (dashed and solid lines, respectively) are interpreted from gas-saturation maps. The G_M and G_L GWCs move 800 m and 550 m updip, respectively. The faults and depth structure for the reservoir simulation were derived from a 1997 dataset that was acquired with a north-south azimuth; hence, most faults do not have the same orientation as those in the 1990 and 2000 datasets. Lines B-B' and C-C' are shown in Figure 10.
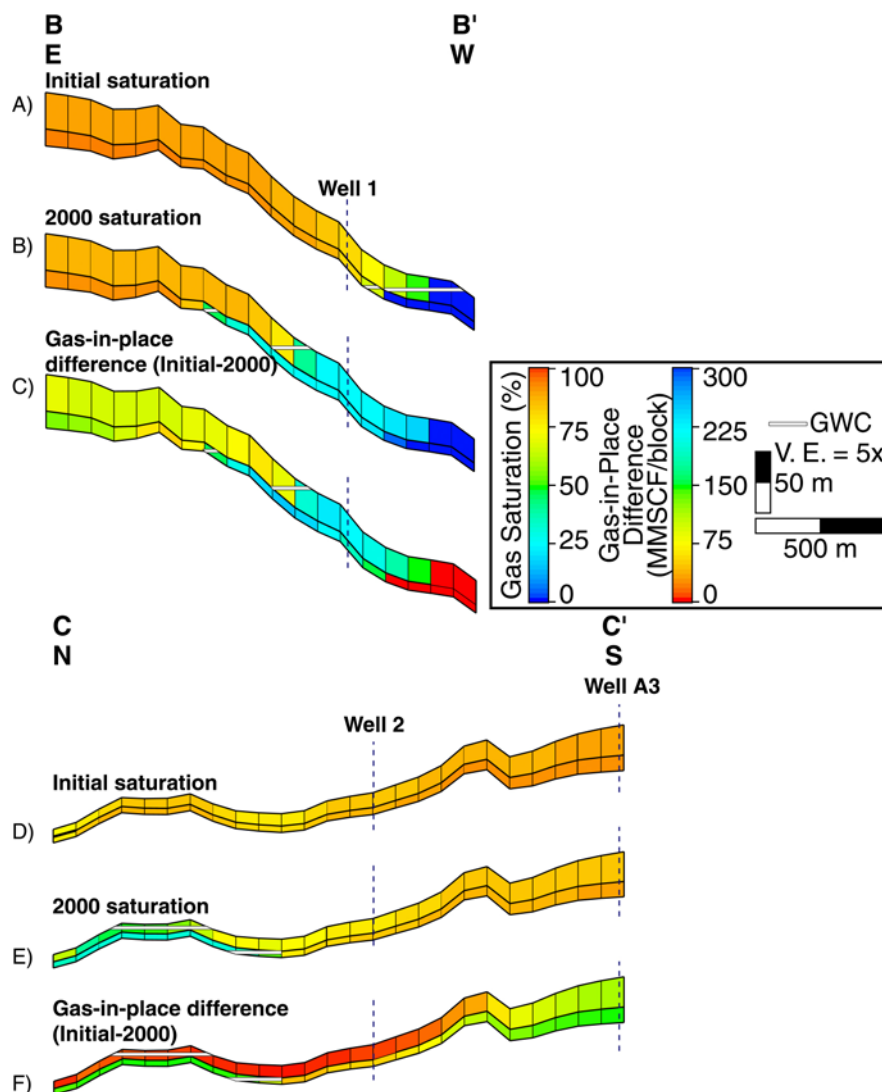
Figure 10: Cross-section of gas-saturation within the RM reservoir A) pre-production and in B) 2000, and C) cross-section of gas-in-place difference, calculated as in Figure 9. The RN reservoir gas-saturation is shown in D) pre-production and in E) 2000, with F) RN reservoir gas-in-place difference. Location of cross-sections B-B' and C-C' shown in Figure 9.

The pressure drop and the subsequent compaction within the water-saturated G-sand cause the impedance of the G_M facies to increase 9.2 % and the impedance of the G_L facies to increase 4.7 % (Fig. 11; Table 6). Regions of the G-sand where gas saturation decreases also increase in impedance (Fig. 11). The G_M facies impedance

increases 10.3 % with gas saturation reduction and pressure decrease, and with

pressure, saturation and compaction decreases, the G_M facies impedance increases

15.3 % (Fig. 11; Table 6). The water-swept G_L facies experiences smaller impedance

increases than the G_M facies. The G_L facies impedance increases 3.6 % with the

pressure and saturation decrease, and it increase 6.6% with reductions in pressure,

saturation, and porosity due to compaction (Fig. 11; Table 6). The region modeled updip

of the 2000 GWC, with constant gas saturation and decreased pressure, experiences

impedance decreases in both facies if compaction is not modeled and impedance

increases if compaction is modeled. Without compaction, average G_M impedance

decreases 1.1 % and the G_L impedance decreases 0.7 % (Fig. 11; Table 6). Impedance

increases 3.9 % and 2.5 % in the G_M and G_L facies, respectively, if the updip reservoir

experiences compaction (Table 6).
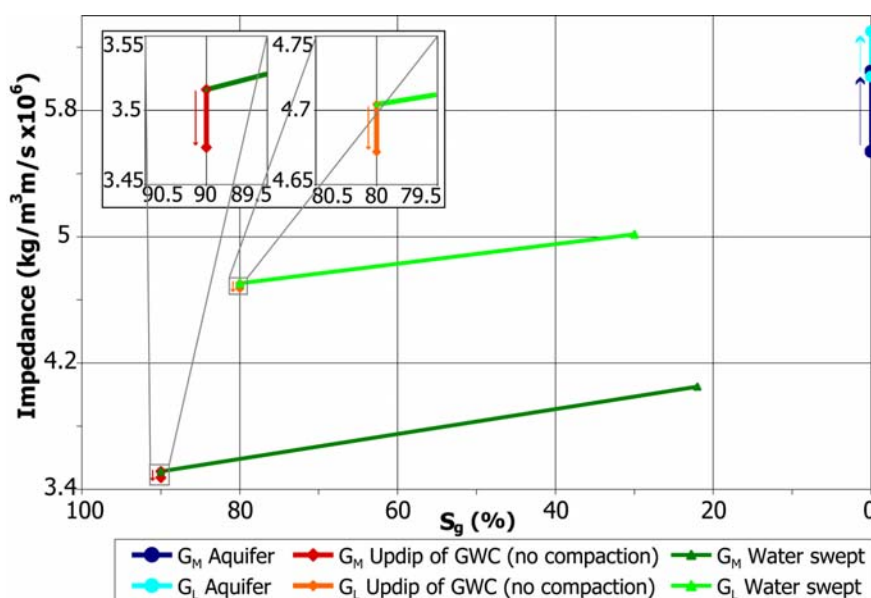
Figure 11: Impedance changes with reductions in pressure and gas saturation for the G_M and G_L facies, based on rock properties described in Table 6. Constant gas saturation and pressure reduction, with no compaction, produces very small decreases in the impedance of both facies.

Table 6: Pressure ($P_{reservoir}$), gas-saturation (S_g), and porosity (Φ_{sand}) of the G_M and G_L facies used in Gassmann fluid substitution, and the initial and 2000 density (ρ_{bulk}), velocity (V_p), and impedance (Z), and the per cent change in impedance (% ΔZ) resulting from differences in initial and 2000 values. Porosity decreases when compaction (comp.) is accounted for in the model. Bold terms indicate 2000 conditions changed from initial conditions to predict differences.

G_M facies	Gas-filled sand					Water-filled sand	
	Initial	Updip of GWC		Water swept		Initial	Comp.
		No comp.	Comp.	No comp.	Comp.		
	1990	2000	2000	2000	2000	1990	2000
$P_{reservoir}$ (MPa)	55.16	**39.99**	**39.99**	**39.99**	**39.99**	55.16	**39.99**
S_g (%)	90	90	90	**22**	**22**	0	0
Φ_{sand} (%)	33	33	**30.6**	33	**30.6**	33	**30.6**
ρ (g/cc)	1.899	1.885	1.942	2.084	2.125	2.151	2.186
v_p (m/s)	1850	1843	1880	1860	1906	2575	2766
Z (kg/m^3 m/s x10^6)	3.514	3.475	3.645	3.876	4.051	5.539	6.047
% ΔZ	--	-1.12	3.87	10.32	15.28	--	9.17

G_L facies	Gas-filled sand					Water-filled sand	
	Initial	Updip of GWC		Water swept		Initial	Comp.
		No comp.	Comp.	No comp.	Comp.		
	1990	2000	2000	2000	2000	1990	2000
P (MPa)	55.16	**39.99**	**39.99**	**39.99**	**39.99**	55.16	**39.99**
S_g (%)	80	80	80	**23**	**23**	0	0
Φ (%)	27	27	**24.9**	27	**24.9**	27	**24.9**
ρ (g/cc)	2.180	2.175	2.199	2.234	2.254	2.271	2.287
v_p (m/s)	2158	2148	2193	2180	2226	2648	2754
Z (kg/m^3 m/s x10^6)	4.704	4.672	4.821	4.871	5.016	6.014	6.299
% ΔZ	--	-0.68	2.48	3.55	6.62	--	4.73

Based on the Gassmann modeling, aquifer regions of the G-sand that experience pressure depletion during production and water-swept reservoir areas increase in impedance. Impedance decreases in regions that are not drained if the rock does not compact with decreased pressure. However, if rock compaction is taken into account, gas-filled sand with diminished pressure will increase in impedance.

Reflection coefficients are derived from original and Gassmann fluid substituted well logs (Appendix B). A wavelet derived from the 1990 seismic dataset is convolved with the reflection coefficients to produce synthetic pre-production and 2000 seismic traces (Fig. 4). When the synthetic traces are differenced, the amplitude differences are consistent with changes in acoustic impedance. Water-swept locations (Well #2 and G_M facies of Well #1), where impedance increases between 1990 and 2000, dim in amplitude when pre-production and 2000 synthetic traces are differenced (Table 7; Figs 4A, 4B). Areas that remain gas-saturated with reduced pressure with decreased impedance (G_L facies of Well #1, Well #A2) show amplitude brightening when synthetic traces are differenced (Table 7; Figs. 4B, 4C).

Table 7: Comparison of amplitude change between synthetic and extracted seismic traces, within the three G-sand reservoir zones. Negative percent differences (% Diff) indicate the 2000 reflection is dimmer than the 1990 reflection.

		Synthetic Traces				Extracted Traces			
		1990	2000	Diff	% Diff	1990	2000	Diff	% Diff
Well #2 Water-Swept	Top/G_L	-4.38	-3.78	-0.60	-14	-6765	-6240	-525	-8
	Base/G_M	6.17	5.00	1.17	-19	11863	7896	3967	-33
Well #1 Water-Swept G_M	Top/G_L	-3.16	-3.39	0.23	7	-6175	-8829	2654	43
	Base/G_M	8.83	8.19	0.64	-7	10017	9171	846	-8
Well #A2 Updip of GWCs	Top/G_L	-3.47	-4.08	0.61	18	-4182	-8903	4721	113
	Base/G_M	8.16	8.79	-0.63	8	10648	11940	-1292	12

DRAINAGE MODEL

We use results from the reservoir simulation and the Gassmann fluid substitution to support interpretation of the drainage behavior imaged in the amplitude-difference maps. The amplitude-difference maps indicate that the massive and laminated facies drain similarly in the RN reservoir and differently in the RM reservoir.

RM Reservoir

We interpret that the GWC within the G_M facies of the RM reservoir moves 750 m west and 100 m vertically between 1996 and 2000, based on the dim Areas C and D (Figs. 5D, 12A). The 2000 GWC follows structure through most of the reservoir, except within Area D, which may be due to thick, clean sands here. Gassmann modeling of water replacing gas in G_M facies supports the interpretation of the GWC movement, as G_M facies impedance increases cause amplitude dimming in synthetic seismic traces (Fig. 4B). Additionally, the reservoir simulation shows large differences in gas-in-place in the downdip regions of the RM reservoir. The region of greatest dimming (Area D, Fig. 5D) corresponds to the region of largest gas-in-place reduction, where differences exceed 300 MMSCF/block gas (Fig. 9E).

Updip of the 2000 GWC, the G_M amplitudes brighten (Fig. 5D); we interpret this is due to a reduction in acoustic impedance caused by expansion of updip gas as the reservoir pressure decreases. The reservoir simulation shows a reduction of gas-in-place in this region, signifying less-dense gas (Fig. 9E). Gassmann modeling of the G_M facies demonstrates that amplitudes brighten when pressure decreases and sand does not compact (Fig. 4C).
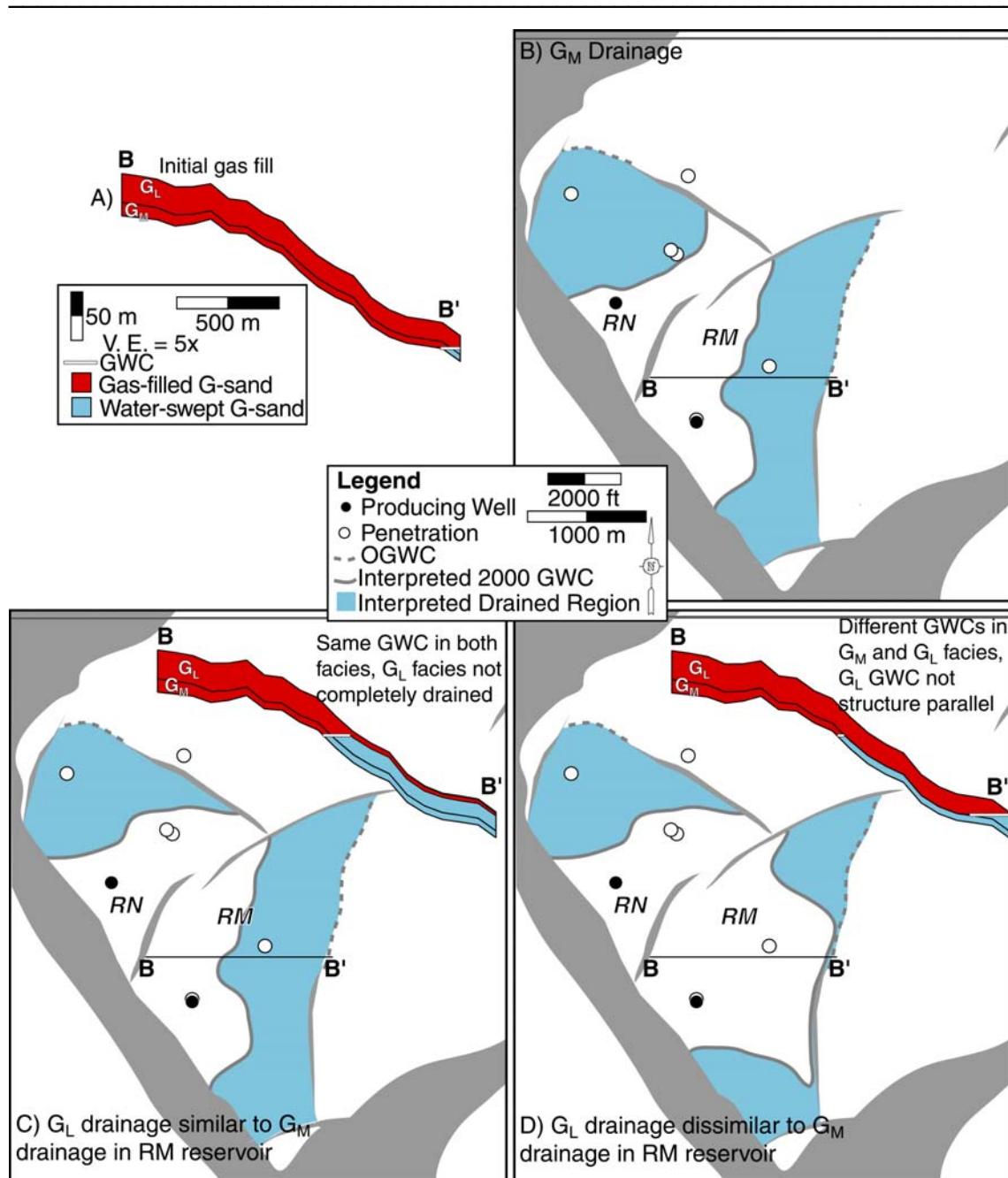
Figure 12: A) Cartoon of initial gas fill in the G_M and G_L facies. B) Areas of water replacement of gas within the G_M facies are highlighted with blue. G_L facies drainage C) similar to the G_M facies in the RM reservoir (sub-parallel to structural contours) and D) dissimilar to G_M facies drainage in the RM reservoir. In this case, the G_L facies GWC migrates up-structure in a non-horizontal manner.

The broad areas of significant (> 99.99 %) Top brightening, with no continuous area of downdip dimming, indicates that the GWC has not moved evenly through the G_L facies (Fig. 6D). The reservoir simulation show reduction of G_L facies gas-in-place in the updip RM reservoir (Fig. 9F); however, the 550 m of GWC movement in the reservoir simulation is not apparent in the amplitude-difference map (Fig. 6D). The interbedded nature of the facies may not allow even water-sweep of all sand layers within the G_L, leaving gas to cause brighter reflections. Additionally, pressure may not be vertically equilibrated within the G_L facies, as in Well #A3 in the RN reservoir (Fig. 13). The pressure gradient between the two facies and the buoyancy of gas may cause water to flow into the G_M facies, causing gas saturation of the G_L facies to increase with production and impedance to decrease.
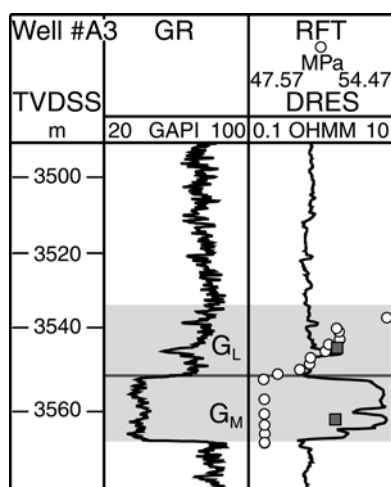
Figure 13: Well #A3 gamma-ray (GR) and resistivity (DRES) well logs, with repeat-formation test (RFT) values overlain. The RFTs were taken in the RN reservoir at Well #A3 in 1998, two years after production began from Well #A2 in the RM reservoir. Pressure within the G_M facies is constant around 48.3 MPa, but the G_L facies pressure is not equilibrated and increases up through the facies. This may indicate that the G_L facies has low vertical permeability, as the pressure decrease experienced from Well #A2 production has only limited effect on pressure within the G_L facies. The G_M and G_L facies pressures from the reservoir simulation are overlain in squares for comparison.

We calculate the gas volumes from the two facies to compare two theories of from where G_L gas drains. The G_M facies drainage is more constrained than G_L drainage, based on the 2000 GWC imaged in the difference map (Figs. 5D, 12). Between 1996 and June 2000, 103 BCF gas were produced from Well #A2 (Table 8). Using the interpreted G_M GWC and average G_M rock properties (33 % porosity, ΔS_g of 68 %), we calculate that 59 BCF gas could be produced from the water-swept region. We assume the remaining 44 BCF came from the G_L facies.

_____

Table 8: Production from the G-sand

Reservoir	Gas Produced by 6/2000 (BCF)	Condensate Produced by 6/2000 (MMSTB)
RM (Well #A2)	103.4	3.3
RN (Well #A3)	42.6	1.1

_____

We first calculate the volume of gas that would be produced if the G_L facies drained similar to the G_M facies (Fig. 12C). Assuming an average gas saturation decrease of 80 to 23 % and porosity of 27 % in the G_L facies sand layers, 57 BCF gas could be extracted from the G_L facies if the GWC moved at the same rate as that of the G_M. Forty-four BCF gas could be produced from the G_L facies if only 77 % of the sand in the laminated facies within the region is drained (Fig. 12C). The RFT data from Well #A3 indicates that sand layers within the G_L facies may not drain as effectively as modeled in the reservoir simulation (Fig. 13). Gas may be trapped in certain sand layers within the facies, and brighten with pressure reduction.

Alternatively, if the two regions of small difference within the G_L amplitude-difference map (Figs. 6D (Areas H and I), 12D) were water-swept, approximately 27 BCF gas would be extracted. The remainder of the gas could come from thinner or more silt-rich reservoir areas, providing the GWC did not follow structure (Fig. 12D).

We observe that the G_M facies GWC moves parallel to structure, while the G_L facies GWC does not, and that the G_M is drained more efficiently than the G_L facies (Figs. 5D, 6D, 12). The vertical variations between G_M and G_L facies drainage in the RM reservoir are analogous to lateral variations in amalgamated channel and overbank deposits drainage behavior in the K40 Sand at the South Timbalier Block 295 field, described by Hoover et al. (1999). They determined that more oil was drained from amalgamated channel sands than from overbank levee and splay sediments, and that contact movement within the overbank deposits was not parallel to structure, due to its lower permeability. The G_M facies behaves similarly to the amalgamated channel sands with GWC movement parallel to structure, and the G_L facies shows signs of poor drainage, similar to the overbank deposits.

RN Reservoir

The RN reservoir dims in both the Top and Base amplitude-difference maps; the dimming is more statistically significant in the Base than in the Top (Figs. 5D, 6D). We attribute that the smaller amount of dimming in the Top is due to the low net-to-gross ratio and thin sand in the G_L facies (Fig. 9A). We interpret that both the Top and Base dim due to water sweep as the GWC moves updip. The difference maps image a 1200 m wide region of drainage in the Base (Figs. 5D (Area A), 12B) and a 1000 m wide region in the Top (Figs. 6D (Area F), 12C); both drained regions extend 50 m vertically.

Gassmann modeling of Well #2 supports the interpretation that water replaces gas in both facies. Synthetic 1990 and 2000 seismic traces from fluid substitution logs show dimming that is similar to the observed 1990 and 2000 traces at Well #2 (Fig. 4A). Areas B and G within the Base and Top difference maps, respectively, show significant

dimming around the A3 well (Figs. 5D, 6D), which may be attributed to compaction and condensate drop-out around the producing well as pressure in the area is lowered.

We compare the known volume of gas produced by Well #A3 (43 BCF gas; Table 8) with the volume of removed gas associated with the interpreted movement of the GWCs in the two facies. We calculate that 29 BCF gas was removed from the G_M facies (based on 30 % porosity and ΔS_g of 67 %), and 8 BCF gas was removed from the G_L facies (based on 27 % porosity and ΔS_g of 57 %). This indicates that the interpretations are feasible because they account for 86 % of the produced volume of gas.

RO Reservoir and Aquifer

Based on the brightening in amplitude-difference maps, we interpret that the gas within the RO reservoir is not produced by the A3 well. This area experiences pressure depletion and subsequently brightens in both Top and Base amplitude-difference maps (Figs. 5D, 6D). Poor velocity control causes the area between the RN and RO reservoir to remain relatively flat when depth-converted. As a result, when establishing the OGWC in the reservoir simulation, gas fills the space between the two reservoirs (Figs. 9, 10). The reservoir simulation models the RO area as water-swept between 1996 and 2000. Alternatively, the RO area brightens due to better imaging in the 2000 data near the regional growth fault to the north.

Compaction of the aquifer east of the RM reservoir within the massive facies causes the small magnitude dimming observed in Area E of the Base amplitude-difference map (Fig. 5D). Modeling of water-saturated sand with Gassmann fluid substitution results in impedance increases when aquifer pressure is reduced and the

sand compacts (Table 6). This is consistent with amplitude dimming between seismic surveys.

CONCLUSIONS

Using the Burkhart et al. (2000) method of poststack data normalization and differencing of amplitude maps, we successfully image differences due to four years of production from a gas-condensate reservoir. The RN reservoir GWCs moved 1000 m updip in the G_L facies and 1200 m updip in the G_M facies; amplitude dimming within the RN reservoir is more significant within the G_M facies than in the G_L facies. Within the G_M facies of the RM reservoir, there is up to 750 m of GWC movement, indicated by amplitude dimming due to impedance increases. Updip of the 2000 GWC, amplitudes brighten as the reduced reservoir pressure causes expansion of the remaining gas and impedance increases. The G_L facies in the RM reservoir does not drain as efficiently as the G_M facies. Inefficient sweep of the laminated facies allows gas to remain in place and causes brightening in the Top amplitude-difference map.   Most amplitude differences can be accounted for with Gassmann fluid substitution modeling, but observed brightening is larger in magnitude than predicted.

REFERENCES

Batzle, M., and Z. Wang, 1992, Seismic properties of pore fluids: Geophysics, v. 57, p. 1396-1408.

Behrens, R. A., P. Condon, W. Haworth, M. Bergeron, Z. Wang, and C. Ecker, 2001, 4D seismic monitoring of water influx at Bay Marchand: The practical use of 4D in an imperfect world: Society of Petroleum Engineers Annual Technical Conference, p. 1-11.

Berni, A. J., J. C. Barros, M. Kohli, T. A. Stelman, and G. E. Perdy, 1997, On the use of data transformation filters in time-lapse imagery: Offshore Technology Conference, p. 153-160.

Burkhart, T., A. R. Hoover, and P. B. Flemings, 2000, Time-lapse (4-D) seismic monitoring of primary production of turbidite reservoirs at South Timbalier Block 295, offshore Louisiana, Gulf of Mexico: Geophysics, v. 65, p. 351-367.

Dean, M. C., M. J. Harris, M. F. Medeiros, and S. Omidele, 2000, Geologic model, reservoir architectures and production performance at Popeye, GC 116 Field, Gulf of Mexico, Annual Meeting Expanded Abstracts - American Association of Petroleum Geologists, vol.2000, p. 37.

Deshpande, A., P. B. Flemings, and J. Huang, 1997, Quantifying lateral heterogeneities in fluvio-deltaic sediments using three-dimensional reflection seismic data: Offshore Gulf of Mexico: Journal of Geophysical Research, v. 102, p. 15,385-15,401.

Fanchi, J. R., 2001, Time-lapse seismic monitoring in reservoir management: The Leading Edge, v. 20, p. 1140-1147.

Gassmann, F., 1951, Elastic waves through a packing of spheres: Geophysics, v. 16, p. 673-685.

Hoover, A. R., T. Burkhart, and P. B. Flemings, 1999, Reservoir and production analysis of the K40 Sand, South Timbalier 295, offshore Louisiana, with comparison to time-lapse (4-D) seismic results: AAPG Bulletin, v. 83, p. 1624-1641.

Johnston, D. H., J. E. Eastwood, J. J. Shyeh, R. Vauthrin, M. Kahn, and L. R. Stanley, 2000, Using legacy seismic data in an integrated time-lapse study: Lena Field, Gulf of Mexico: The Leading Edge, v. 19, p. 294-302.

Kaleta, N., 2001, Time-lapse (4D) Seismic Investigation of the I3 and TA2 Sands, Kilauea Field, Green Canyon Block 6, Gulf of Mexico: Masters degree thesis, Pennsylvania State University, University Park, PA.

Koster, K., P. Gabriels, M. Hartung, J. Verbeek, G. Deinum, and R. Staples, 2000, Time-lapse seismic surveys in the North Sea and their business impact: The Leading Edge, v. 19, p. 286-293.

Kragh, E., and P. Christie, 2001, Seismic repeatability, normalized RMS and predictability: 71st Annual International Meeting of the Society of Exploration Geophysicists, p. 1656-1659.

Landmark Graphics Corporation, 2003, 3D Poststack Regrid, ProMAX 4D Reference Manual, Landmark Graphics Corporation, p. 2175-2188.

Lumley, D. E., 2001, Time-lapse seismic reservoir monitoring: Geophysics, v. 66, p. 50-53.

Lumley, D. E., 2002, Synergies in time-lapse seismic, medical, and space imaging: The Leading Edge, v. 21, p. 599-606.

Lygren, M., K. Fagervik, T. S. Valen, A. Hetlelid, G. Berge, G. V. Dahl, L. Sonneland, H. E. Lie, and I. Magnus, 2003, A method for performing history matching of

reservoir flow models using 4D seismic data: Petroleum Geosciences, v. 9, p. 85-90.

Nur, A., 1989, Four-dimensional seismology and (true) direction detection of hydrocarbons: The Leading Edge, v. 8, p. 30-36.

Pfeiffer, D., B. Mitchell, and G. Yevi, 2000, Mensa, Mississipi Canyon block 731 field, Gulf of Mexico-an integrated field study: GCSSEPM Foundation 20th Annual Research Conference, Deep-water Reservoirs of the World, p. 756-775.

Rafalowski, J. W., B. W. Regel, D. L. Jordan, and D. O. Lucidi, 1996, Green Canyon Block 205 lithofacies, seismic facies, and reservoir architecture: AAPG Studies in Geology, v. 42, p. 133-142.

Rickett, J. E., and D. E. Lumley, 1998, A cross-equalization processing flow for off-the-shelf 4D seismic data: 68th Annual International Meeting, Society of Exploration Geophysicists, p. 16-19.

Rickett, J. E., and D. E. Lumley, 2001, Cross-equalization data processing for time-lapse reservoir monitoring: A case study from the Gulf of Mexico: Geophysics, v. 66, p. 1015-1025.

Robinson, E. A., and S. Treitel, 1967, Principles of digital Wiener filtering: Geophysical Prospecting, v. 15, p. 312-333.

Ross, C. P., G. B. Cunningham, and D. P. Weber, 1996, Inside the cross-equalization black box: The Leading Edge, v. 15, p. 1233-1240.

Sengupta, M., G. Mavko, and T. Mukerji, 2003, Quantifying subresolution saturation scales from time-lapse seismic data: A reservoir monitoring case study: Geophysics, v. 68, p. 803-814.

Swanston, A., 2001, Imaging Drainage of Turbidite Reservoirs Through Time-Lapse Seismic Analysis at Bullwinkle, Green Canyon Block 65, Offshore Gulf of Mexico:

Master's Degree thesis, The Pennsylvania State University, University Park, PA, 112 p.

Swanston, A. M., P. B. Flemings, J. T. Comisky, and K. D. Best, 2003, Time-lapse imaging at Bullwinkle field, Green Canyon 65, offshore Gulf of Mexico: Geophysics, v. 68, p. 1470-1484.

Varnai, P., N. Hurley, and P. Weimer, 1998, Three-dimensional seismic stratigraphic expression of Pliocene-Pleistocene turbidite systems, northern Green Canyon (offshore Louisiana), northern Gulf of Mexico: AAPG Bulletin, v. 82, p. 986-1012.

Waggoner, J. R., A. Cominelli, R. H. Seymour, and A. Stradiotti, 2003, Improved reservoir modeling with time-lapse seismic data in a Gulf of Mexico gas condensate reservoir: Petroleum Geosciences, v. 9, p. 61-72.

Wang, Z., 2001, Fundamentals of seismic rock physics: Geophysics, v. 66, p. 398-412.

Wang, Z., W. K. Hirsche, and G. Sedgwick, 1991, Seismic monitoring of water floods? A petrophysical study: Geophysics, v. 56, p. 1614-1623.

APPENDIX A

DERIVATION AND APPLICATION OF A MATCH FILTER

INTRODUCTION

The cross-equalization filter (cross-equalization, Wiener, Wiener shaping, or Wiener matching filter) (Robinson and Treitel, 1967) is used to remove differences in the source wavelet and processing differences between two seismic datasets. It is typically used to make two datasets as similar as possible in terms of phase, time, and amplitude of the seismic traces. The match filter is derived from the comparison of two traces, the input trace and the desired output trace; it is then applied to the input trace. The filter is calculated by minimizing energy differences between the actual and desired filter outputs with the least-squares method in the time domain (Robinson and Treitel, 1967). The application of the match filter should correct differences in the embedded wavelet (phase and amplitude magnitude) and static time shifts between datasets. We detail the derivation and application of the match filter using single seismic traces extracted from two different 3D seismic surveys at the same CDP location.

DERIVATION OF THE MATCH FILTER

The mathematical derivation of the match filter that follows is in the form of Robinson and Treitel (1980). The input signal is represented by b (b_0, b_1, …, b_n) and the desired output is represented by d (d_0, d_1, …, d_{m+n}) where m and n are nonnegative integers (Table A-1). We derive a filter, f, that when applied to b, the actual output (c) is

the least-squares approximation to the desired output, d. The actual output, c, is derived by convolving the f with b, which can be expressed as

$$c_t = \sum_{s=0}^{m} f_s b_{t-s},$$
(A-1)

for $t = 0, 1, 2, \ldots, m+n$. We find the error between the desired and actual outputs, then sum and square the errors (J),

$$J = \sum_{t=0}^{m+n} (d_t - c_t)^2 = \sum_{t=0}^{m+n} \left(d_t - \sum_{s=0}^{m} f_s b_{t-s} \right)^2.$$
(A-2)

The least-squares theory states that the sum of squared errors is the minimum if and only if

$$\frac{\delta J}{\delta f_i} = 0$$
(A-3)

for $i = 0, 1, 2, \ldots, m$. From this theory, we differentiate the above equations (A-2 and A-3) to calculate the normal equation

$$-2 \sum_{t=0}^{m+n} \left(d_t - \sum_{s=0}^{m} f_s b_{t-s} \right) b_{t-i} = 0,$$
(A-4)

where Equation A-4 is a set of linear simultaneous equations whose solution represents a least-squares fit (Sheriff, 1991).

The auto-correlation of the input signal is r_s, where

$$r_s = \sum_{t=0}^{n} b_{t+s} b_t = b_s b_0 + b_{1+s} b_1 + \ldots + b_n b_{n-s}$$
(A-5)

and g_s denotes the cross-correlation of the desired output with the input signal, where

$$g_s = \sum_{t=0}^{n} d_{t+s} b_t = d_{t+s} b_t + d_{1+s} b_1 + \ldots + d_{n+s} b_n$$
(A-6)

and s = 0, 1, 2, …, m. If f_s denotes the filter (f_s = f_0, f_1, …, f_m), then the normal equation in terms of the auto-correlation and cross-correlation becomes
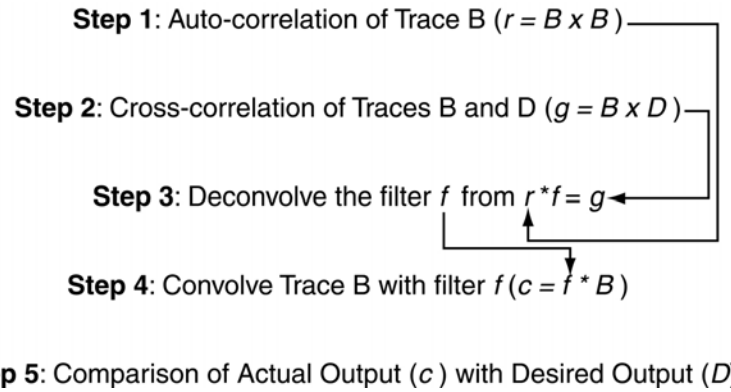
$$\sum_{s=0}^{m} f_s r_{i-s} = g_i$$

(A-7)

for i = 0, 1, 2, …, m. We solve the equation for the filter f_s through deconvolution.

APPLICATION OF THE MATCH FILTER

The match filter (f) is used to match the characteristics of one seismic trace to the characteristics of another trace. Two seismic traces are used in this exercise; the desired result is for Seismic Trace B (b) to have the same characteristics as Seismic Trace D (d) after the application of the match filter. Trace B is auto-correlated in order to determine the wavelet within the trace. The derived wavelet is then deconvolved from the cross-correlation of Traces B and D, which results in the match filter. The deconvolution of the wavelet from the cross-correlated traces is done using Levinson recursion, which simultaneously solves two sets of linear equations (Hayes, 1996). The match filter is convolved with Trace B to produce the actual output (c) (Fig. A-1).

We perform the match filter derivation and application on Traces B and D four different ways. The filter is derived using the original Traces B and D, 5 s in length, and a 1 s subset of the original traces. We also apply a static shift, based on cross-correlation results, and phase rotation to Trace B, then use Trace D and the modified 5 s and 1 s Trace B to derive a match filter for the respective trace pairs. The results obtained from calculating the match filter using the modified Trace B are statistically better than the results from using the original Trace B.

Step 1: Auto-correlation of Trace B ($r = B \times B$)

Step 2: Cross-correlation of Traces B and D ($g = B \times D$)

Step 3: Deconvolve the filter f from $r * f = g$

Step 4: Convolve Trace B with filter f ($c = f * B$)

Step 5: Comparison of Actual Output (c) with Desired Output (D)

Figure A-1: Summary of the match filter derivation process. The filter is calculated from the auto-correlation of the input trace and the cross-correlation of the input and desired output traces. It is then convolved with the input trace (Yilmaz, 1987).

In order to quantify the success of the match filter application on a trace-by-trace basis, we employ qualitative and statistical methods of comparison. The mean and root-mean square operator of each trace (b, d, and c) are calculated, and the correlation coefficient and the covariance are determined between sets of traces (b and d, c and d).

Statistical Tools

The root-mean square (RMS) operator is defined as

$$RMS(x) = \sqrt{\frac{\sum_{i=1}^{n}(x_i^2)}{n}}$$

(A-10)

where n is the number of samples in x, the seismic trace (Swanston, 2001). This is equivalent to the standard deviation of a trace. The covariance between the two seismic traces is a measure of joint variability between two variables, and is quantified by

$$\sigma_{bd} = \frac{\sum_{i=1}^{n}(x_{ib} - \bar{x}_b)(x_{id} - \bar{x}_d)}{n-1}$$

(A-11)

where x_{ib} and x_{id} are incremental samples of the traces and $\overline{x}_b$ and $\overline{x}_d$ are the means of b and d, respectively (Middleton, 2000). Correlation between two traces is measured with the correlation coefficient, defined as

$$r = \frac{\sigma_{bd}}{\sigma_b \cdot \sigma_d}$$

(A-12)

where σ_b and σ_d are the standard deviations of b and d, respectively (Burkhart et al., 2000). If $r = 1$, the two seismic traces correlate perfectly; low values of r indicate the seismic traces do not correlate. For r = -1, the seismic traces vary with exactly 180° phase difference.

Table A-1: Nomenclature.

b	Input trace (Trace B)
d	Desired output trace (Trace D)
c	Actual output trace
f	Match filter
i, m, n, s, t	Nonnegative integers
J	Sum and square of error value
r_s	Auto-correlation of b
g_s	Cross-correlation of b and d
x_{ib}	Incremental samples of b
x_{id}	Incremental samples of d
$\overline{x}_b$	Mean of b
$\overline{x}_d$	Mean of d
σ_b	Standard deviation of b
σ_d	Standard deviation of d
b_5	5-second input trace
d_5	5-second desired output trace
c_5	5-second actual output trace
b_5'	5-second phase-rotated trace, static shifted input trace
c_5'	5-second actual output trace using b_5' for filter derivation
b_1	1-second input trace
d_1	1-second desired output trace
c_1	1-second actual output trace
b_1'	1-second phase-rotated trace, static shifted input trace
c_1'	1-second actual output trace using b_1' for filter derivation

Example

Two different traces, B and D, were used to model the derivation and application of the match filter. Within these examples, the match filter (f) is applied to Trace B (b). A major difference between the Traces B and D is the phase of the data; Trace B is zero-phase RFC seismic data and Trace D is an integrated RFC trace (Deshpande et al., 1997), which is approximately a -90° phase shift from zero-phase RFC data. Both traces were band-pass filtered with filter corner frequencies of 0-5-40-45 Hz. To compare

results, we compare the mean and standard deviation of individual traces. We also compare the correlation coefficient and covariance between the input and desired output (*b* vs. *d*) with the desired output and the actual output (*c* vs. *d*).

Five second trace: A qualitative comparison of the match filter application shows favorable results, but this qualitative analysis is limited to judgment of the reservoir region (3900-4000 ms) and the seafloor (1000 ms) (Fig. A-2). The application of the match filter rotates the phase of the zero-phase RFC Trace B so that its phase matches that of the integrated RFC phase of Trace D. The magnitude of the reservoir reflection is increased when comparing b_5 with the output trace (c_5). The seafloor reflections of b_5 and d_5 are very different in frequency and amplitude, the match filter does mute the reflection seen in b_5, but does not match the spike seen at the seafloor in d_5.

The similarity of b_5 and d_5 increase quantitatively, as shown in Table A-2. The correlation coefficient increases from 0.319 to 0.885 with the application of the match filter. The covariance between Traces B and D also increases from 21.713 to 51.573 with the application of the match filter (Table A-2). The increase in covariance and correlation coefficients between Traces B and D with the application of the match filter indicate that the match filter has transformed b_5 into a trace which is more representative of d_5.
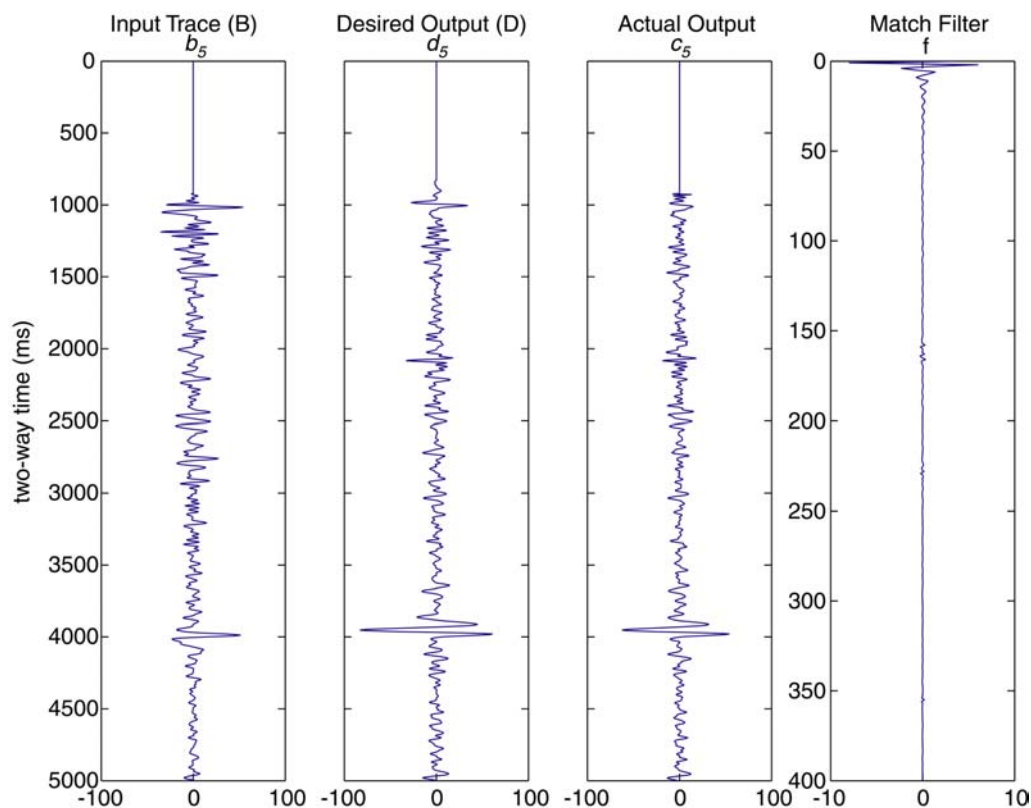
Figure A-2: Input (b_5), desired (d_5), and actual output (c_5) traces used in the five-second long experiment using Traces B and D. The match filter is shown on the right.

Table A-2: Statistical results of match filter application on 5 s traces. The prime symbol after b_5 and c_5 indicates that Trace B was phase rotated and static time shifted prior to match filter derivation.
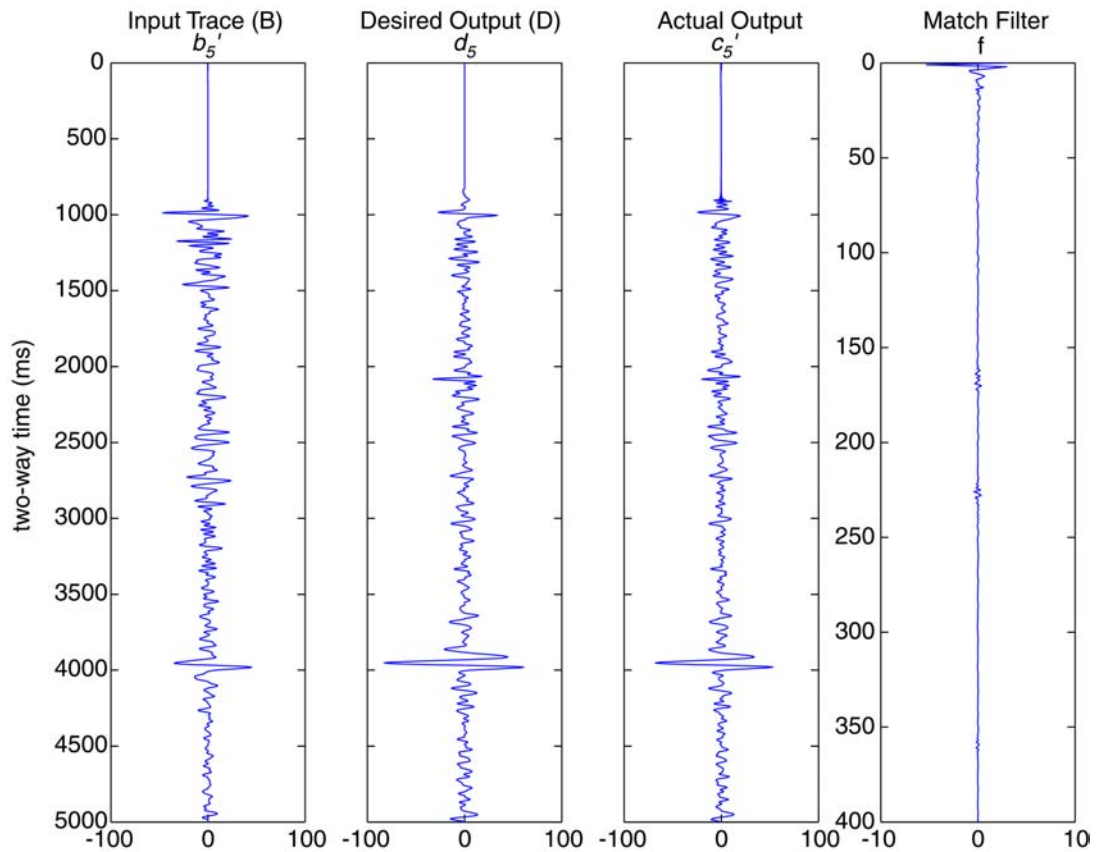
	5 s traces		5 s traces, phase rotated and shifted	
	b_5xd_5	c_5xd_5	$b_5'xd_5$	$c_5'xd_5$
Correlation Coefficient	0.319	0.885	0.457	0.913
Covariance	21.713	51.573	30.677	56.575

Five second shifted and phase-rotated trace: To maximize similarity between the Traces B and D (b_5 and d_5) before derivation and application of the match filter, a phase rotation of -90° and a static shift was applied to Trace B. To determine the

amount of static shift, the two band-pass filtered traces (b_5 phase rotated by -90° and d_5) were cross-correlated, the result of which was plotted on a scale indicating the amount of shift. The maximum correlation occurred at -20 ms, and Trace B was shifted that amount. After the static shift was applied to the phase rotated Trace B (now b_5'), the match filter was derived using b_5' and d_5. The application of the static shift and phase rotation to Trace B increased the correlation coefficient between the input and desired output traces by 43 %, from 0.319 to 0.457 (Table A-2).

After Trace B was shifted and phase rotated, the match filter was derived and applied (Fig. A-3). The statistical comparison of b_5' vs. d_5 and c_5' vs. d_5 show improvement of the input and output traces when compared to b_5 vs. d_5 and c_5 vs. d_5 (Table A-2). The correlation coefficient between Traces B and D increased from 0.457 to 0.913 with the application of the match filter; this correlation coefficient is higher than that obtained by using only the match filter. Covariance increased from 30.677 to 56.575.

The correlation coefficient and covariance between b_5' and d_5 and d_5 and c_5' are higher than those of the non-modified traces. These results indicate that the improvement in similarity between Traces B and D by static shift and phase rotation improves the similarity between the match-filtered Trace B and Trace D.

Figure A-3: Input (b_5'), desired (d_5), and actual output (c_5') traces used in the five-second long shifted and phase-rotated trace experiment. The input trace has been phase rotated by -90° and shifted -20 ms. The match filter is shown on the right.

One second trace: The same process of match filter derivation and application was performed on a one-second subset of the five-second traces, from 3300 to 4300 ms, which is the time unit used in the 4D analysis in Chapter 2. The application of the match filter changes the phase and reduces the magnitude of the reservoir event and the frequency spectrum of the output trace, c_1 (Fig. A-4; Table A-3). The filter does not perfectly match reservoir events of the desired and actual output traces (d_1 and c_1) (Fig. A-4), but does improve the similarity. However, with the application of the match filter, the correlation coefficient between Traces B and D is increased by 43 %, from 0.528 to

0.755. The covariance between the 1997 and 1984 trace also increased from 75.578 to 129.281 with the application of the match filter.
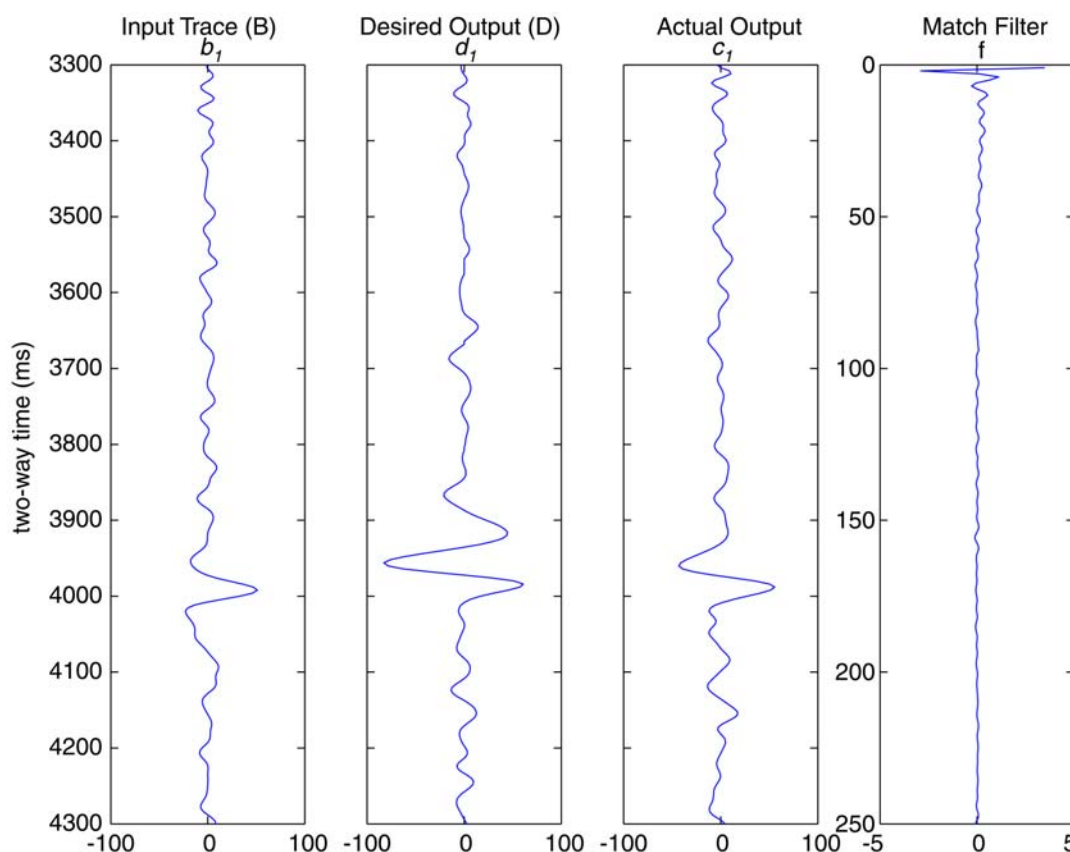
Figure A-4: Input (b_1), desired (d_1), and actual output (c_1) traces used in the one-second long trace experiment. The match filter is shown on the right.

Table A-3: Statistical results of match filter application on 1 s traces. The prime symbol after b_5 and c_5 indicates that Trace B was phase rotated and static time shifted prior to match filter derivation.
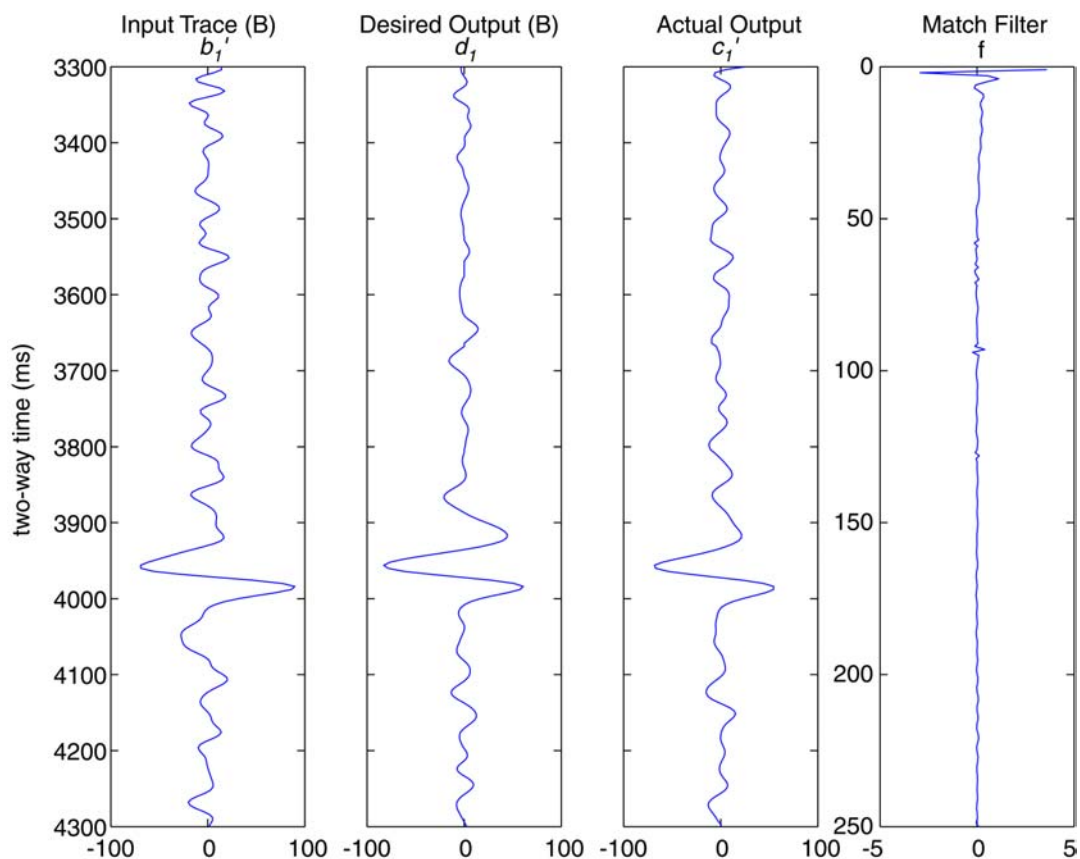
	1 s traces		1 s traces, phase rotated and shifted	
	b_1xd_1	c_1xd_1	$b_1'xd_1$	$c_1'xd_1$
Correlation coefficient	0.528	0.755	0.738	0.865
Covariance	75.578	129.281	104.202	183.843

One second shifted and phase-rotated trace: The same -90° phase rotation and -20 ms static time shift was applied to Trace B as in the previous section, before the derivation and application of the match filter on the one-second long trace. The phase rotated and shifted Trace B is termed b_1' (Table A-1). The application of the phase rotation and the shift results in a correlation coefficient between b_1' and d_1 of 0.738, 40 % larger than the correlation coefficient between b_1 and d_1 (Table A-3). The actual output trace (c_1') is the best match to the desired output over all other input or output one-second long traces, when correlation coefficients and covariance values are compared (Table A-2). The correlation coefficient between Trace D and the modified Trace B increases from 0.738 to 0.865, and the covariance improves by 76 % (Table A-3). When traces b_1', b_1', d_1 and c_1' are compared, it is apparent that the combination of phase rotation, static time shifts, and match filtering achieve the best match between two different traces (Fig. A-5). When the actual output c1' is compared with c1, from the unmodified Trace B, a significant improvement in the shape of the trace at the reservoir interval is visible (Figs. A-4, A-5).

Limitations of Method

The match filter process is not typically very sensitive to the amount of delay needed, once it's close to the optimum delay (Yilmaz, 1987). Better results are obtained if a constant time shift is applied. Additionally, if both *b* and *d* have large spikes in the same region (the reservoir), and a filter is derived using the two traces, the derived match filter applied to another "test" trace cannot create a large spike in the reservoir region, if the "test" data does not contain a reservoir region. The filter does not contain the information to scale any region of the "test" data; it fixes differences between the embedded (source) wavelets within the datasets. It does not necessarily make one

trace automatically look like the other; instead, it shapes and scales the embedded

wavelet within the output trace so that the *d* and *c* have the same embedded wavelet.

Figure A-5: Input (b_1'), desired (d_1), and actual output (c_1') traces used in the one-second shifted and phase rotated trace experiment. The input trace has been phase rotated by -90° and shifted -20 ms. The match filter is shown on the right. The phase rotation and static shift allows for a better match in reservoir events (3950 ms) between desired and actual outputs than those in Figure A-4.

REFERENCES

Burkhart, T., A. R. Hoover, and P. B. Flemings, 2000, Time-lapse (4-D) seismic monitoring of primary production of turbidite reservoirs at South Timbalier Block 295, offshore Louisiana, Gulf of Mexico: Geophysics, v. 65, p. 351-367.

Deshpande, A., P. B. Flemings, and J. Huang, 1997, Quantifying lateral heterogeneities in fluvio-deltaic sediments using three-dimensional reflection seismic data: Offshore Gulf of Mexico: Journal of Geophysical Research, v. 102, p. 15,385-15,401.

Hayes, M. H., 1996, Statistical Digital Signal Processing and Modeling: New York, John Wiley and Sons, Inc., 608 p.

Middleton, G. V., 2000, Data Analysis in the Earth Sciences Using MATLAB: Upper Saddle River, NJ, Prentice Hall, 260 p.

Robinson, E. A., and S. Treitel, 1967, Principles of digital Wiener filtering: Geophysical Prospecting, v. 15, p. 312-333.

Robinson, E. A., and S. Treitel, 1980, Geophysical Signal Analysis: Prentice-Hall Signal Processing Series: Englewood Cliffs, NJ, Prentice-Hall, Inc., 466 p.

Sheriff, R. E., 1991, Encyclopedic Dictionary of Exploration Geophysics: Tulsa, OK, Society of Exploration Geophysicists, 384 p.

Swanston, A., 2001, Imaging Drainage of Turbidite Reservoirs Through Time-Lapse Seismic Analysis at Bullwinkle, Green Canyon Block 65, Offshore Gulf of Mexico: Master's Degree thesis, The Pennsylvania State University, University Park, PA, 112 p.

Yilmaz, O., 1987, Seismic Data Processing: Investigations in Geophysics: Tulsa, OK, Society of Exploration Geophysicists, 526 p.

APPENDIX B

GASSMANN FLUID SUBSTITUTION MODELING

Refer to pocket insert.

APPENDIX C

INTEGRATION OF GEOLOGIC MODEL AND RESERVOIR SIMULATION, POPEYE FIELD, GREEN CANYON BLOCK 116

Refer to pocket insert.

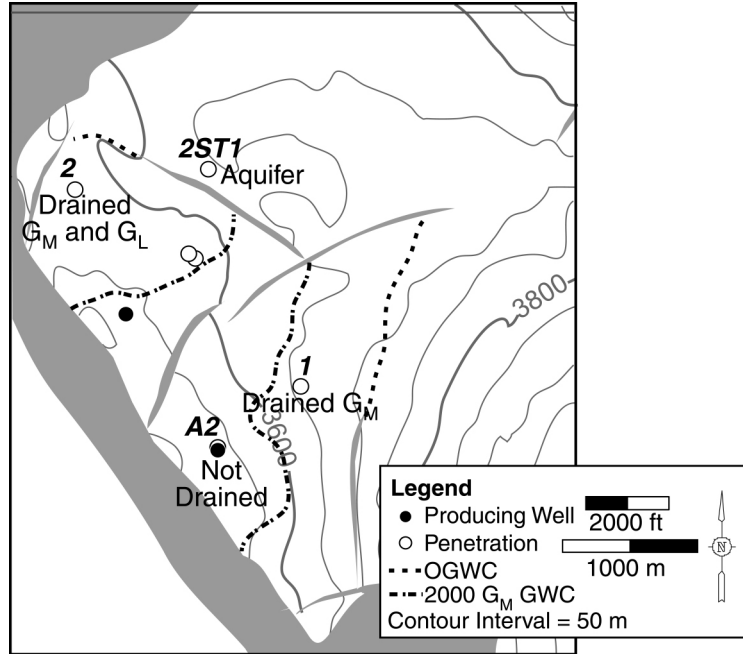## APPENDIX B—GASSMANN FLUID SUBSTITUTION MODELING

INTRODUCTION

We use Gassmann fluid substitution modeling to relate time-lapse results to changes in acoustic properties of the G-sand. Fluid saturation and pressure changes induced by production of hydrocarbons can have a significant effect on the acoustic properties of unconsolidated sand reservoirs (Domenico, 1977).

Gassmann's equation (1951) relates the bulk p-wave modulus of a fluid-saturated rock to its porosity and the bulk moduli of the mineral matrix, fluid, and dry rock. We first determine for the dry rock bulk modulus for the in-situ pre-production scenario when all the other above parameters are known (Zhu et al., 1990). We can then predict the bulk p-wave modulus of the saturated rock as a function of any pressure and pore fluid. The new compressional velocity of the fluid substituted rock is then calculated from the new bulk p-wave modulus and the new density of the saturated rock. We incorporate the effect of pressure changes on porosity, dry bulk modulus, and pore fluid properties (including the condensation of gas), so that the fluid substitution model is comprehensive.

The lithological differences of the two G-sand facies require that they be modeled separately, as they have different model inputs of pressure and fluid saturations at the same lateral position because of different drainage behaviors. Application of Gassmann modeling is straight-forward for the G_M because it is a clean massive sand that meets the model assumptions summarized by Wang (2001). However, Gassmann's equations often produce unreliable results when applied to shaley sands because the basic assumptions are not valid (Smith et al., 2003). The G_L violates the assumptions that the rock is homogeneous and isotropic and that the pores are interconnected and communicating.

We model the G_L using a laminar mode of mixing where the large grains and small grains fill space separately as alternating laminae of shale and sand on a scale much less than the seismic wavelength. A net-to-gross thickness value is used to separate sands and silty shales. The sand portion of the G_L is fluid substituted; we assume that no changes occur in the silty shales. The porosity of the sand portion is calibrated by core samples. The effective bulk density of the G_L is calculated as the volumetrically-weighted average of shale density and fluid-substituted sand density. The effective compressional velocity is calculated using the Backus average of shale velocity and fluid-substituted sand velocity (Mavko et al., 1998). We model the effective acoustic properties of the G_L as one unit, rather than at each sample of the well logs or for each sand and shale layer.

We generalize the behavior of the G-sand through production with three regions: the aquifer below the original GWC that experiences only pressure depletion, a region swept by water as the GWC moves updip, experiencing reductions in pressure and gas saturation, and areas above GWCs that only experience pressure depletion. Four well locations, in the three regions of the reservoir conditions, are modeled at pre-production and 2000 conditions (Figure B-1). The water-saturated well 2ST1 represents aquifer regions. Water-swept regions are modeled with well 2, where both the G_M and G_L facies are downdip of the 2000 GWC, and at well 1, where the G_M facies is water-swept and the G_L facies remains gas-saturated. Well A2 does not experience water-sweep in either facies, and we use it to understand the regions above the 2000 GWC. The wells are modeled with initial fluid and pressure conditions and then with fluid-substituted conditions.

Figure B-1: Wells modeled with Gassmann fluid substitution represent three regions of G-sand with initial and 2000 GWCs in the G_M facies. Well 2ST1 represents the G-sand aquifer, wells 1 and 2 characterize water swept regions, and well A2 represents undrained reservoir regions.

_____

EFFECTS OF AQUIFER PRESSURE DEPLETION
Well 2ST1

We model the effects of pressure reduction within the aquifer using the rock properties from well 2ST1, which is 100 % water saturated. The pressure reduction causes the water density to slightly decrease and become more compressible. However, sand within the facies compacts and stiffens with the pressure drop, which has a greater effect on the bulk G-sand properties. The net effect of pressure decrease at the 2ST1 well is an increase in density, velocity, and impedance. Figure B-2 shows the results of lowering aquifer pressure from 8000 to 5000 psi in the G_M and G_L facies. Both facies

experience increases in density and velocity with decreasing pressure, which causes the impedance of the facies to increase.
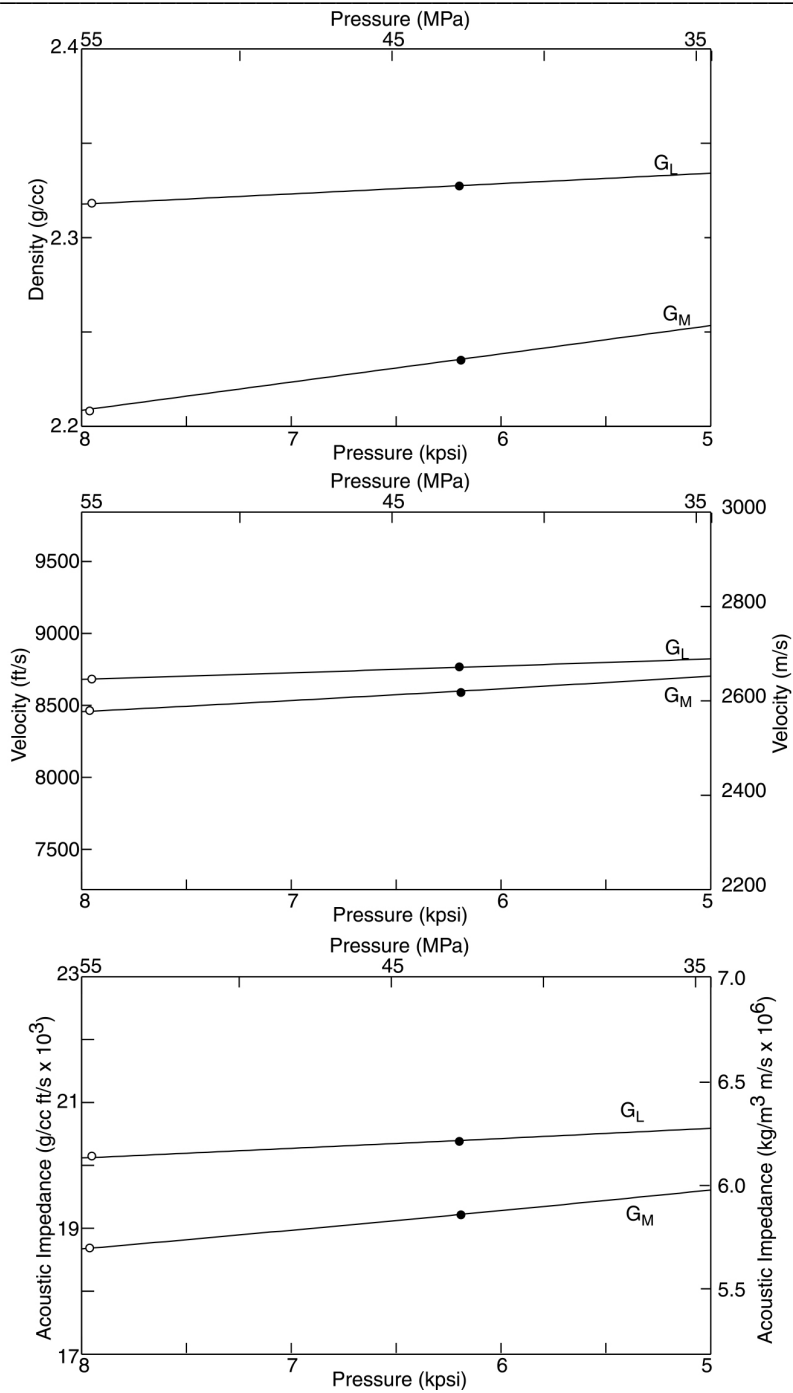
Figure B-2: As pressure decreases in well 2ST1, density, velocity, and impedance all increase due to compaction and frame stiffening. There are minimal fluid effects since the well is water saturated at all times and water has low compressibility. Pre-production density, velocity and impedance are marked with white circles, 2000 density, velocity are indicated with black circles.

Between 1996 and 2000, pressure within the G_M at well 2ST1 decreases from 7961 to 6191 psi and from 7951 to 6199 psi in the G_L facies. This change causes an 8.8 % increase of the G_M impedance, as velocity increases by 187 m/s and density increases 0.031 g/cc (Table B-1). The bulk G_L impedance increases 2.1 % due to the 103 m/s increase in velocity and the 0.024 g/cc increase in density within the G_L sand (Table B-1, Figure B-3). The RFCs of the G-sand are low magnitude because the sand is water-saturated (Figure B-3).

Table B-1: Reservoir properties at well 2ST1.

Parameter		G_M		G_L			
		Initial	2000	Initial		2000	
Stress	P_p (psi)	7961	6191	7951		6199	
Fluid	S_w	1	1	1		1	
	S_g	0	0	0		0	
	S_o	0	0	0		0	
	$?_f$ (g/cc)	1.128	1.124	1.128		1.124	
	K_f (MPa)	3356	3335	3356		3335	
Matrix	$?_m$ (g/cc)	2.650		2.650			
	K_m (MPa)	38,000		38,000			
Skeleton	K_{dry} (MPa)	4239	4485	1389		1482	
	$??$	0.195		0.195			
	$?$ (%)	29.1	27.3	25.0		23.4	
	c_p (psi^{-1})	49.464 x10^{-6}		49.464 x10^{-6}			
Bulk	M (GPa)	16.25	17.107	12.100		13.345	
				Sand	Bulk	Sand	Bulk
	$?_b$ (g/cc)	2.202	2.233	2.269	2.318	2.293	2.327
	V_p (m/s)	2579	2766	2309	2626	2412	2670
	Z (kg/m^3·m/s x10^6)	5.679	6.178	5.240	6.086	5.532	6.214
	Net-to-gross ratio	1		0.4			
Shale	$?_{sh}$ (g/cc)	2.350					
	V_{sh} (m/s)	2903					
	Z_{sh} (kg/m^3·m/s x10^6)	6.822					
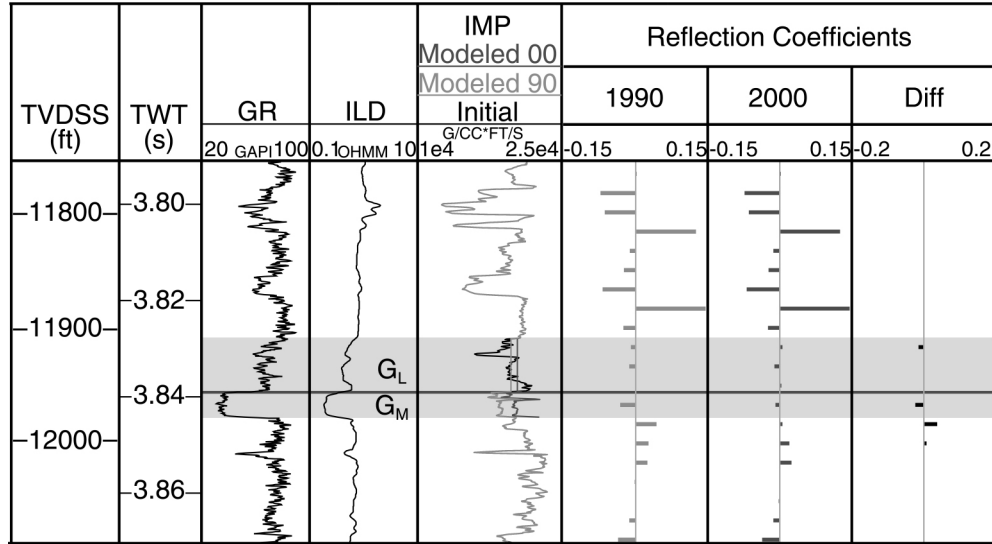
Figure B-3: Well 2ST1 gamma ray (GR), resistivity (ILD), and impedance (IMP) logs in the depth domain and reflection coefficients in the time domain. The G_L facies is modeled as the effective acoustic impedance; these averaged values are used to derive RFCs. The water-saturated nature of the G-sand at well 2ST1 causes low-valued RFCs, differences between 1990 and 2000 RFCs are also small at the G-sand interval

---

EFFECTS OF WATER SWEEP

G_M Facies—Well 1

We model the effects of reducing the gas saturation (91 % to 23 %) and the pressure (7980 to 6391 psi) in the G_M facies, while maintaining initial gas saturation (68 %) and reducing the pressure (7970 to 6227 psi) within the G_L facies (Table B-2). Initial pressure and saturation values were measured at the well. Pressure and G_M gas saturation for the year 2000 are based on reservoir simulation results; we maintain initial G_L gas saturation in the 2000 fluid substitution to force an impedance decrease. The pressure reduction within the G_M facies causes compaction and stiffening of the rock frame; these effects are not accounted for within the G_L facies. Only the effect of pressure reduction on fluid properties is modeled in the G_L facies. Even when saturation is held constant,

changes in the elastic properties of the saturating fluid, due to pressure changes, affect the acoustic velocity of the rock (Clark, 1992; Alberty, 1996; Jones et al., 1998).

A generalized model for the G-sand as saturation and pressure are varied shows that most of the velocity and impedance change occurs between gas saturations of 0 to 0.15 (Figure B-4). Between gas saturations of 0.15 to 1.0, velocity does not change much (Domenico, 1976) and changes in impedance are largely driven by density changes. In fact, as gas saturations decrease from 1.0, compressional velocity decreases slightly first before it increases. This is because initially density increases at a greater rate than the effect of compressibility reduction; then they switch and velocity increases. This model also shows that lower net-to-gross thickness ratios result in smaller amounts of impedance change as saturation is varied and higher overall impedance (Figure B-5). This is because there is less sand to fluid-substitute and have less effect on the overall bulk rock properties.

The 68 % saturation decrease and 20 % pressure reduction within the G_M facies cause a bulk density increase of 0.113 g/cc and a velocity increase of 61 m/s (Table B-2). Reducing the pressure 22 % within the G_L facies caused a decrease of 0.003 g/cc in bulk density and a decrease of 48 m/s in velocity (Table B-2). The pressure and fluid saturation changes increase the acoustic impedance of the massive facies and decrease the impedance of the laminated facies (Table B-2). Both G_M and G_L layers experience low magnitude changes in acoustic impedance because seismic velocities remain relatively low through a wide range of gas saturations (Figure B-5). When compaction is accounted for in the G_L facies, impedance increases between initial and 2000 conditions.

Table B-2: Reservoir properties at well 1.

Parameter		G_M		G_L			
		Initial	2000	Initial		2000	
Stress	P_p (psi)	7980	6391	7970		6227	
Fluid	S_w	0.09	0.76	0.32		0.31	
	S_g	0.91	0.23	0.68		0.68	
	S_o	0	0.01	0		0.01	
	$?_f$ (g/cc)	0.356	0.921	0.551		0.525	
	K_f (MPa)	190	487	249		176	
Matrix	$?_m$ (g/cc)	2.650		2.650			
	K_m (MPa)	38,000		38,000			
Skeleton	K_{dry} (MPa)	3094	3251	3480		3480	
	??	0.195		0.195			
	? (%)	33.0	31.3	30.0		30.0	
	c_p (psi^{-1})	49.464 x10^{-6}		49.464 x10^{-6}			
Bulk	M (GPa)	6.734	7.851	7.572		7.514	
				Sand	Bulk	Sand	Bulk
	$?_b$ (g/cc)	1.996	2.109		2.188		2.185
	V_p (m/s)	1865	1926		2153		2105
	Z (kg/m^3·m/s x10^6)	3.735	4.064		4.711		4.600
	Net-to-gross ratio	1		0.5			
Shale	$?_{sh}$ (g/cc)	2.290					
	V_{sh} (m/s)	2438					
	Z_{sh} (kg/m^3·m/s x10^6)	5.584					
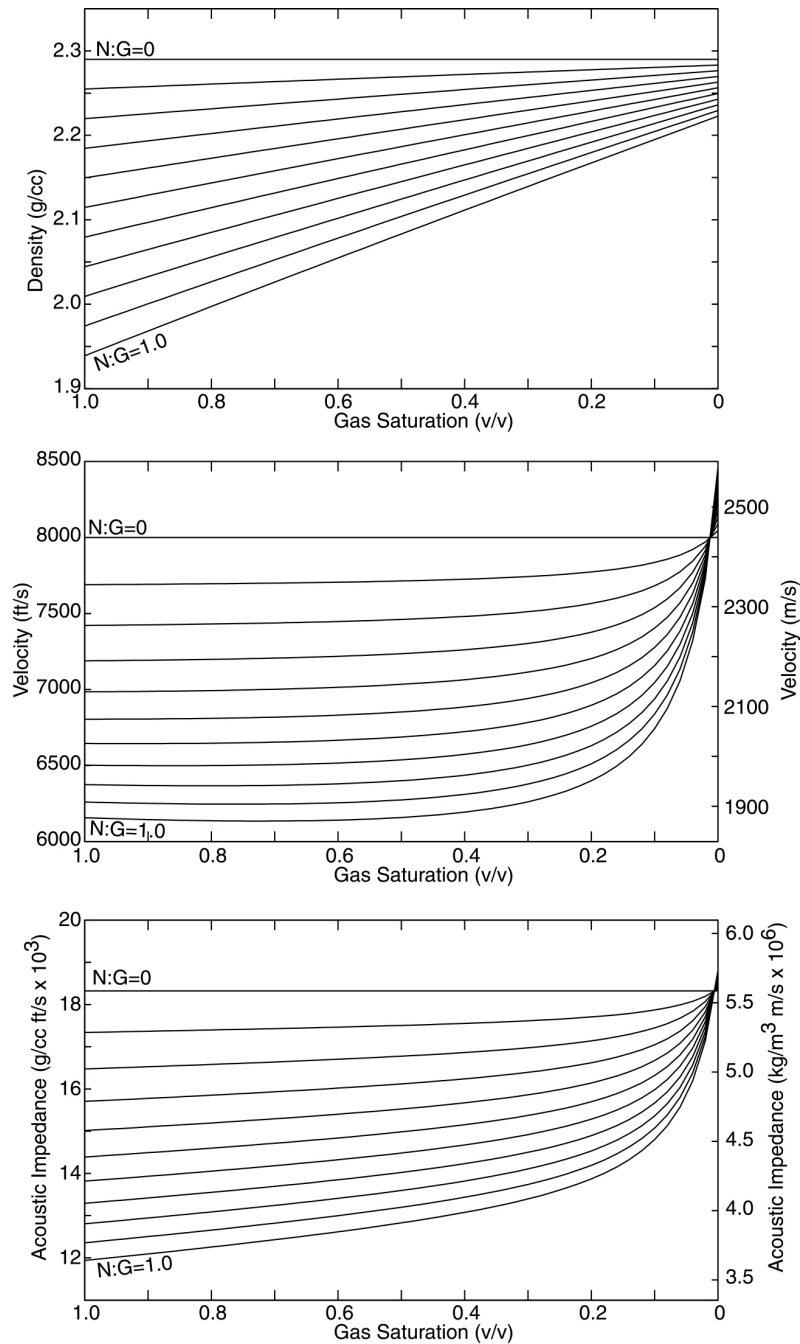
Figure B-4: A generalized acoustic model of the G-sand incorporates pressure reduction from 8000 to 6000 psi and fluid changes from all gas to mostly brine, with oil saturation increasing from 0 to 0.01 and porosity decreasing from 0.30 to 0.28 within the sand. We assume pure shale with no fluid flow (N:G=0), fluid substitute pure sand (N:G=1), and then mix the sand and shale at N:G intervals of 0.1.
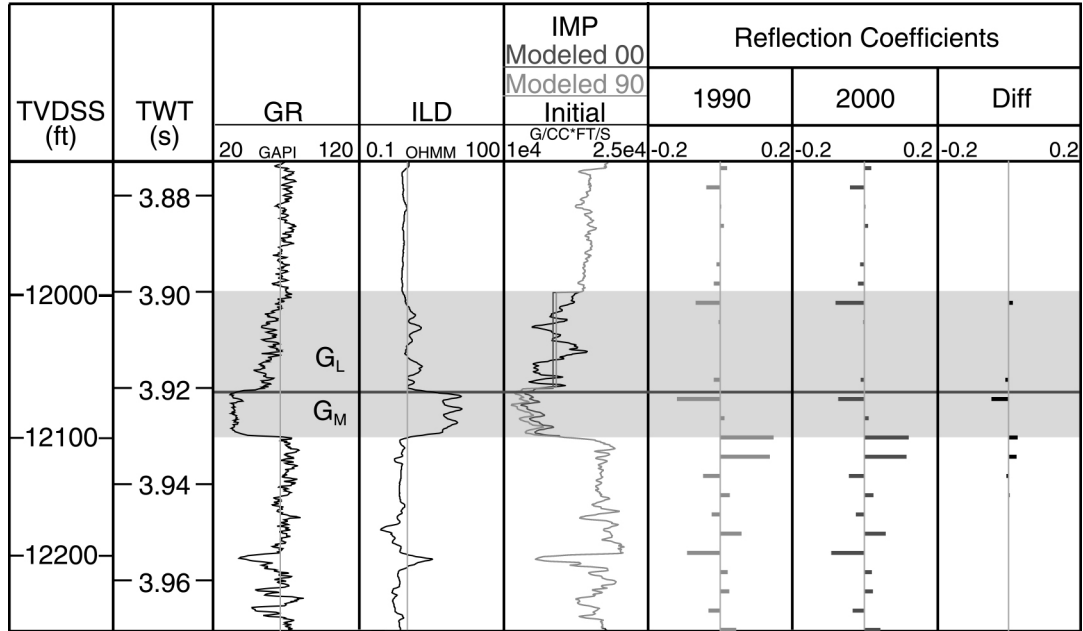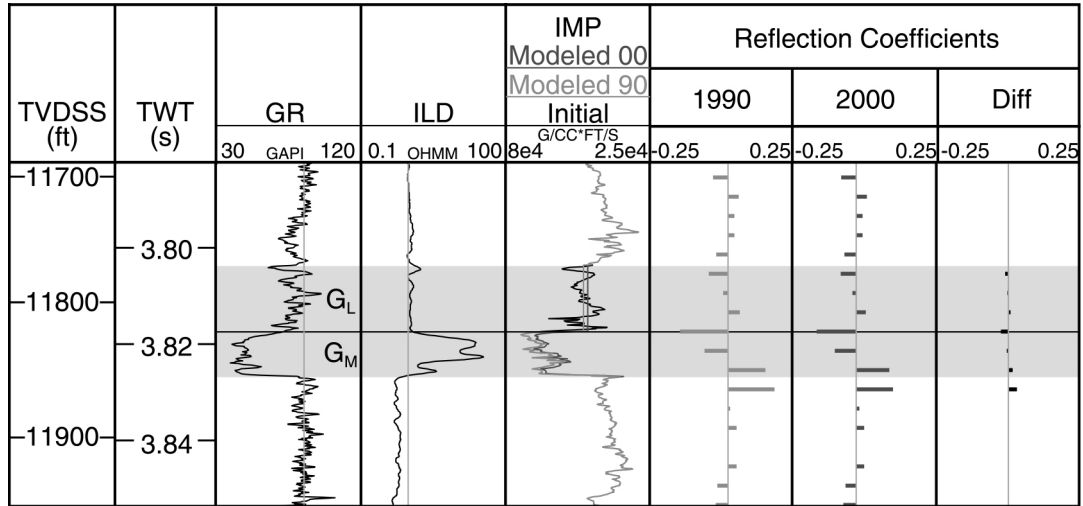
Figure B-5: Well 1 gamma ray (GR), resistivity (ILD), and impedance (IMP) logs in the depth domain and reflection coefficients in the time domain. The G_L facies is modeled as the effective acoustic impedance; these averaged values are used to derive RFCs. The transformation of the impedance log from a sample interval of 0.5 ft in depth to a less frequent sample of 4 ms in time causes band-limiting which smears the reflection response in time. Hence, the time and depth samples do not line up and the G_M base RFCs extend across two time samples.

G_M and G_L Facies—Well 2

The G_M and G_L facies are thin at well 2 (9.4 m total net sand) (Figure B-6), additionally, the net-to-gross ratio of the G_L facies is only 10 % (Table B-3). We interpret that both facies were water-swept by 2000, reducing gas saturation in the G_M facies from 90 to 23 % and from 60 to 23 % in the G_L sand layers (Table B-3). Year 2000 gas saturations are based on residual gas saturations at well 1 within the reservoir simulation. We model that reservoir pressure in the G_M decreased from 7935 to 5302 psi, and the pressure within the G_L decreased from 7924 to 5301 psi, based on initial and

2000 reservoir simulation results. Compaction is accounted for in both facies, which

causes reduction of porosity (Table B-3) and stiffening of the rock frame.

Figure B-6: Well 2 gamma ray (GR), resistivity (ILD), and impedance (IMP) logs in the depth domain and reflection coefficients in the time domain. The impedance values of the G_M and G_L increase between initial and 2000 conditions. The difference between time and depth domains is explained in Figure B-5.

The decrease in reservoir pressure and gas saturation causes velocity and density

to increase in both G_M and G_L facies. The impedance of the G_M facies increases 10.8 %

while the G_L facies impedance increases only 1.4 % (Table B-6). The small amount of

change within the G_L occurs because only 10 % of the unit is affected by water sweep

and compaction.

EFFECTS OF GAS EXPANSION

G_M and G_L Facies: Well A2

Neither facies of the G-sand in well A2 was water-swept by 2000; we model

constant gas saturation and diminished reservoir pressure. Figure B-7 shows the effects

within the G_M and G_L facies of decreasing reservoir pressure; each facies in the plots of Figure D are represented with two lines. The dashed line for each facies represents the modeled behavior of density, velocity, and impedance as pressure is reduced, accounting only for changes in fluid properties. As pressure decreases along this trend, density, velocity, and impedance decrease. The solid line of each facies predicts the rock properties as pressure decreases, accounting for fluid property changes and compaction. When compaction effects are incorporated, density, velocity and impedance increase as reservoir pressure decreases (Figure B-7).

_____

Table B-3: Reservoir properties at well 2.

Parameter		G_M		G_L			
		Initial	2000	Initial		2000	
Stress	P_p (psi)	7935	5302	7924		5301	
Fluid	S_w	0.10	0.76	0.40		0.76	
	S_g	0.90	0.23	0.60		0.23	
	S_o	0	0.01	0		0.01	
	$?_f$ (g/cc)	0.364	0.910	0.619		0.910	
	K_f (MPa)	191	379	278		379	
Matrix	$?_m$ (g/cc)	2.650		2.650			
	K_m (MPa)	38,000		38,000			
Skeleton	K_{dry} (MPa)	3159	3443	3029		3314	
	??	0.195		0.195			
	? (%)	30.1	27.4	28.0		25.4	
	c_p (psi^{-1})	49.464 x10^{-6}		49.464 x10^{-6}			
Bulk	M	6.924	8.126	6.810		7.910	
				Sand	Bulk	Sand	Bulk
	$?_b$ (g/cc)	2.076	2.173	2.081	2.264	2.208	2.281
	V_p (m/s)	1845	1913	1809	2311	1893	2359
	Z (kg/m^3·m/s x10^6)	3.830	4.161	3.765	5.232	4.179	5.383
	Net-to-gross ratio	1		0.10			
Shale	$?_{sh}$ (g/cc)	2.290					
	V_{sh} (m/s)	2438					
	Z_{sh} (kg/m^3·m/s x10^6)	5.584					

_____
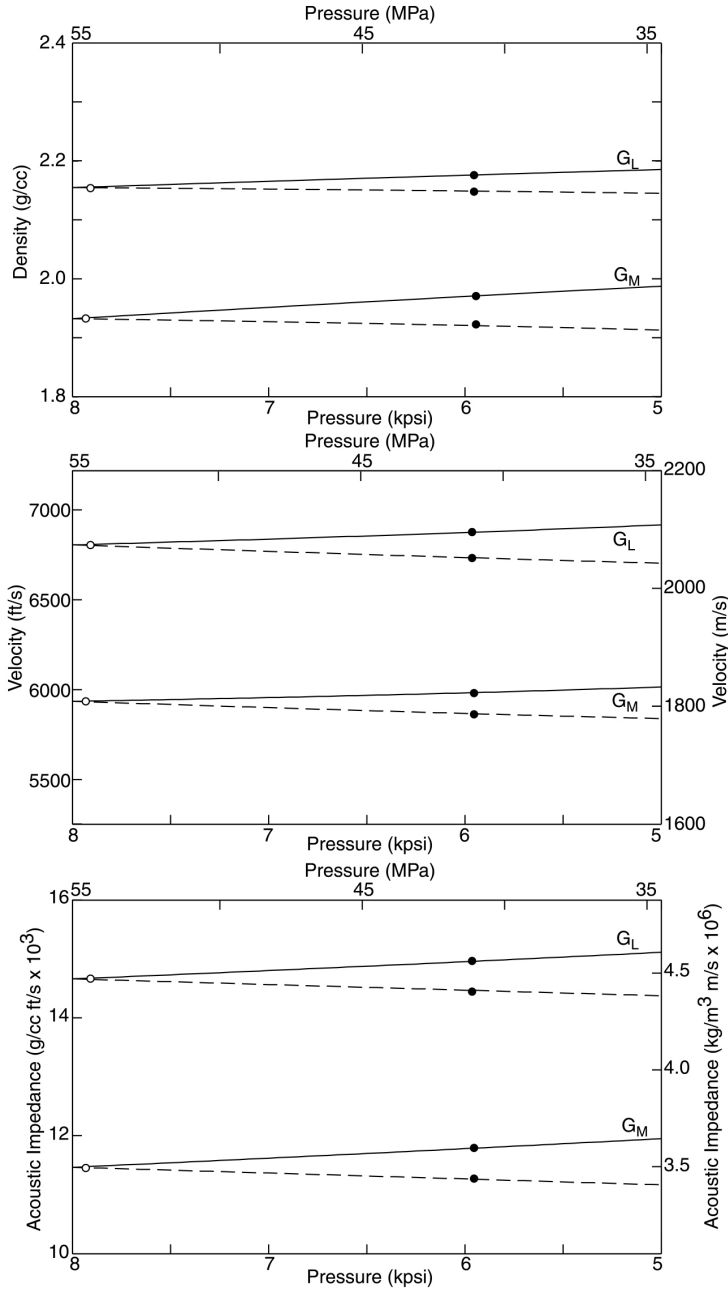
Figure B-7: Effects of pressure reduction on the velocity, density, and impedance of the G_M and G_L facies with pressure reduction at well A2. Density, velocity, and impedance increase with decreasing pressure when changes in fluid properties and compaction are modeled (solid lines). When only fluid property changes are accounted for in the model, density, velocity, and impedance decrease with decreased reservoir pressure (dashed lines). Initial reservoir pressure at well A2 is marked with white circles, 2000 reservoir pressure is indicated with black circles.

At well A2 between 1996 and 2000, reservoir pressure decreases from 7932 to 5954 psi in the G_M facies and from 7908 to 5964 psi in the G_L facies. To force impedance decrease, we model that gas saturation remains constant in both facies (85 %) and that compaction does not affect the sands. If these pressure changes are modeled (allowing gas expansion), impedance decreases by 1.1 % in the G_M facies and by 6.2 % in the G_L facies, if compaction of the sand is not taken into account (Table B-4B, Figure B-8). We also model the difference between initial and 2000 conditions considering the effects of compaction, and that gas saturation in the G_M and G_L facies decreases from 85 to 82 %, based on reservoir simulation results. The impedance of the G_M and G_L facies increases 3.7 and 3.3 %, respectively, when compaction and fluid effects are considered (Table B-4B).
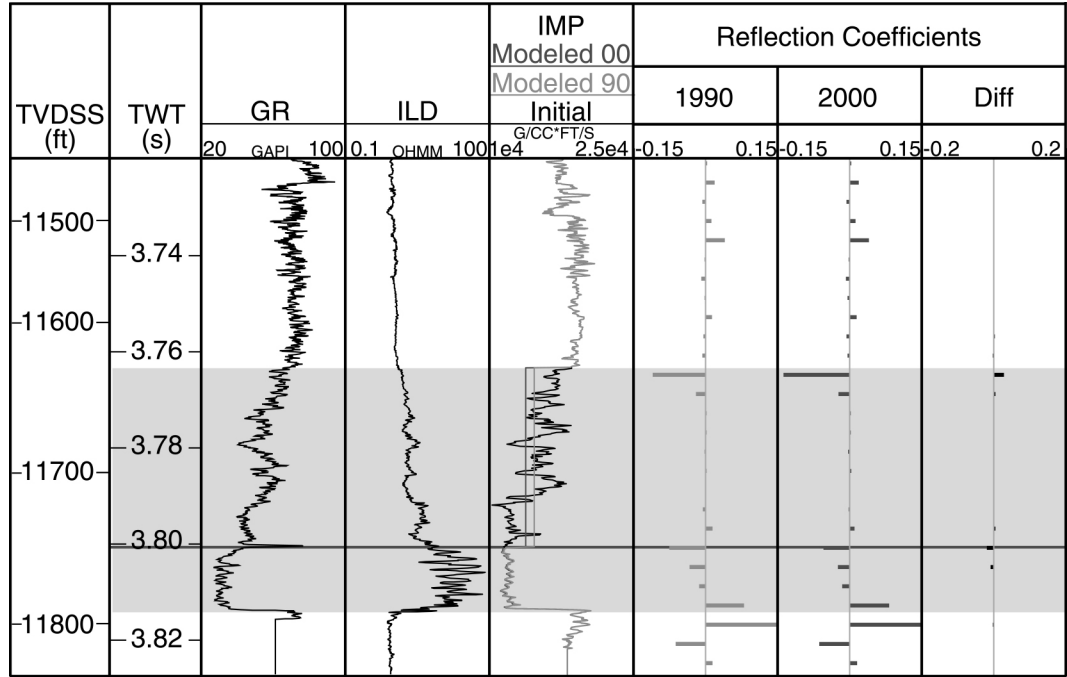
Figure B-8: Well A2 gamma ray (GR), resistivity (ILD), and impedance (IMP) logs in the depth domain and reflection coefficients in the time domain. The impedance values of the G_L decrease between initial and 2000 conditions, GM impedance decreases only 1.1 %. The difference between time and depth domains is explained in Figure B-5.

Table B-4A: Reservoir properties at well A2, saturation constant and no compaction effects.

Parameter		G_M		G_L sand			
		Initial	2000	Initial		2000	
Stress	P_p (psi)	7932	5954	7908		5964	
Fluid	S_w	0.15	0.14	0.15		0.142	
	S_g	0.85	0.85	0.85		0.85	
	S_o	0	0.01	0		0.01	
	$?_f$ (g/cc)	0.407	0.371	0.406		0.370	
	K_f (MPa)	201	134	200		133	
Matrix	$?_m$ (g/cc)	2.650		2.650			
	K_m (MPa)	38,000		38,000			
Skeleton	K_{dry} (MPa)	2835		2806			
	??	0.195		0.195			
	??(%)	33.2		27			
	c_p (psi^{-1})	49.464 x10^{-6}		49.464 x10^{-6}			
Bulk	M	6.240	6.075	6.201		6.092	
				Sand	Bulk	Sand	Bulk
	$?_b$ (g/cc)	1.902	1.890	2.044	2.154	2.035	2.149
	V_p (m/s)	1808	1787	1742	2071	1730	1955
	Z (kg/m^3·m/s x10^6)	3.416	3.380	3.560	4.461	3.520	4.201
	Net-to-gross ratio	1		0.60			
Shale	$?_{sh}$ (g/cc)	2.320					
	V_{sh} (m/s)	2721					
	Z_{sh} (kg/m^3·m/s x10^6)	6.314					

Table B-4B: Reservoir properties at well A2, saturation decrease and compaction.

Parameter		G_M		G_L sand			
		Initial	2000	Initial		2000	
Stress	P_p (psi)	7932	5954	7908		5964	
Fluid	S_w	0.15	0.14	0.15		0.142	
	S_g	0.85	0.82	0.85		0.82	
	S_o	0	0.01	0		0.01	
	ρ_f (g/cc)	0.407	0.397	0.406		0.397	
	K_f (MPa)	201	138	200		138	
Matrix	ρ_m (g/cc)	2.650		2.650			
	K_m (MPa)	38,000		38,000			
Skeleton	K_{dry} (MPa)	2.835	3.018	2806		3001	
	α	0.195		0.195			
	ϕ (%)	33.2	31.2	27.0		25.1	
	c_p (psi^{-1})	49.464 x10^{-6}		49.464 x10^{-6}			
Bulk	M	6.240	6.474	6.201		6.528	
				Sand	Bulk	Sand	Bulk
	ρ_b (g/cc)	1.902	1.948	2.044	2.154	2.084	2.179
	V_p (m/s)	1808	1817	1742	2071	1770	2115
	Z (kg/m^3·m/s x10^6)	3.416	3.542	3.560	4.461	3.689	4.609
	Net-to-gross ratio	1		0.60			
Shale	ρ_{sh} (g/cc)	2.320					
	V_{sh} (m/s)	2721					
	Z_{sh} (kg/m^3·m/s x10^6)	6.314					

REFERENCES

Alberty, M., 1996, The influence of the borehole environment upon compressional sonic logs: The Log Analyst, v. 37, p. 30-45.

Clark, V. A., 1992, The effect of oil under in-situ conditions on the seismic properties of rocks: Geophysics, v. 57, p. 894-901.

Domenico, S. N., 1976, Effect of brine-gas mixture on velocity in an unconsolidated sand reservoir: Geophysics, v. 41, p. 882-894.

Domenico, S. N., 1977, Elastic properties of unconsolidated porous sand reservoirs: Geophysics, v. 42, p. 1339-1368.

Gassmann, F., 1951, Elastic waves through a packing of spheres: Geophysics, v. 16, p. 673-685.

Jones, S. M., C. McCann, T. R. Astin, and J. Sothcott, 1998, The effects of pore-fluid salinity on ultrasonic wave propagation in sandstones: Geophysics, v. 63, p. 928-934.

Mavko, G., T. Mukerji, and J. Dvorkin, 1998, The Rock Physics Handbook; Tools for Seismic Analysis in Porous Media: Cambridge, United Kingdom, Cambridge University Press, 329 p.

Smith, T. M., C. H. Sondergeld, and C. S. Rai, 2003, Gassmann fluid substitution: a tutorial: Geophysics, v. 68, p. 430-440.

Wang, Z., 2001, Fundamentals of seismic rock physics: Geophysics, v. 66, p. 398-412.

Zhu, X., G. A. McMechan, and Anonymous, 1990, Direct estimation of the bulk modulus of the frame in a fluid-saturated elastic medium by Biot theory, SEG Abstracts, vol.60: International Meeting and Exposition, Society of Exploration Geophysicists, p. 787-790.

INTEGRATION OF GEOLOGIC MODEL AND RESERVOIR SIMULATION, POPEYE FIELD, GREEN CANYON 116

Beth Yuvancic-Strickland[1], Eric Kuhl[2], Tin-Wai Lee[1], Benjamin Seldon[1], Peter B. Flemings[1], and Turgay Ertekin[2]

[1]Pennsylvania State University, Department of Geosciences, University Park, PA 16802; E-mail: flemings@geosc.psu.edu
[2]Pennsylvania State University, Department of Petroleum and Natural Gas Engineering, University Park, PA 16802; E-mail: turgay@pnge.psu.edu

ABSTRACT

Small variations in fault length, channel permeability, and aquifer volume defined in our geologic model of the G-sand strongly influence flow characteristics, and hence the predicted recovery from the RA reservoir in the Popeye field (Gulf of Mexico, GC 72/116). A history-matched base-case reservoir simulation, with structure and rock properties derived from the geologic model, results in a volume of bypassed gas-condensate in the RA reservoir. Turbidite gravity flows entered the basin from the north and deposited amalgamated sheet sands. This was overlain by channels that bypassed the Popeye area, depositing interbedded very fine-grained sands and silts in levee-overbank environments. A channel and impermeable faults compartmentalize the G-sand into four gas-condensate reservoirs (RA, RB, RM and RN). By increasing the distance between two faults separating the RA and RB reservoirs, decreasing the RA aquifer volume, or increasing channel permeability in the reservoir model, flow characteristics in the RA reservoir change. These changes, which reflect the geologic uncertainties in our interpretation, result in economically significant differences in total recovery.

INTRODUCTION

Numerous reservoirs are found in turbidite deposits within minibasins on the continental slope of the northern Gulf of Mexico deep-water (Fig. 1). In this tabular-salt minibasin province, intraslope minibasins develop from salt withdrawal due to sediment loading (Diegel et al., 1995). The resultant bathymetry focuses gravity flows into these areas of localized accommodation (Rowan and Weimer, 1998). This depositional process accumulated the high quality sands described at Bullwinkle (Holman and Robertson, 1994), Genesis (Rafalowski et al., 1994), Mensa (Pfeiffer et al., 2000), Mars (Mahaffie, 1994), and Auger fields (Booth et al., 2000; McGee et al., 1994).

Characterizations of the Weyburn (Elsayed et al., 1993) and Ram-Powell (Lerch et al., 1996) fields and a depositional model for the Bullwinkle field (Holman and Robertson, 1994) were created
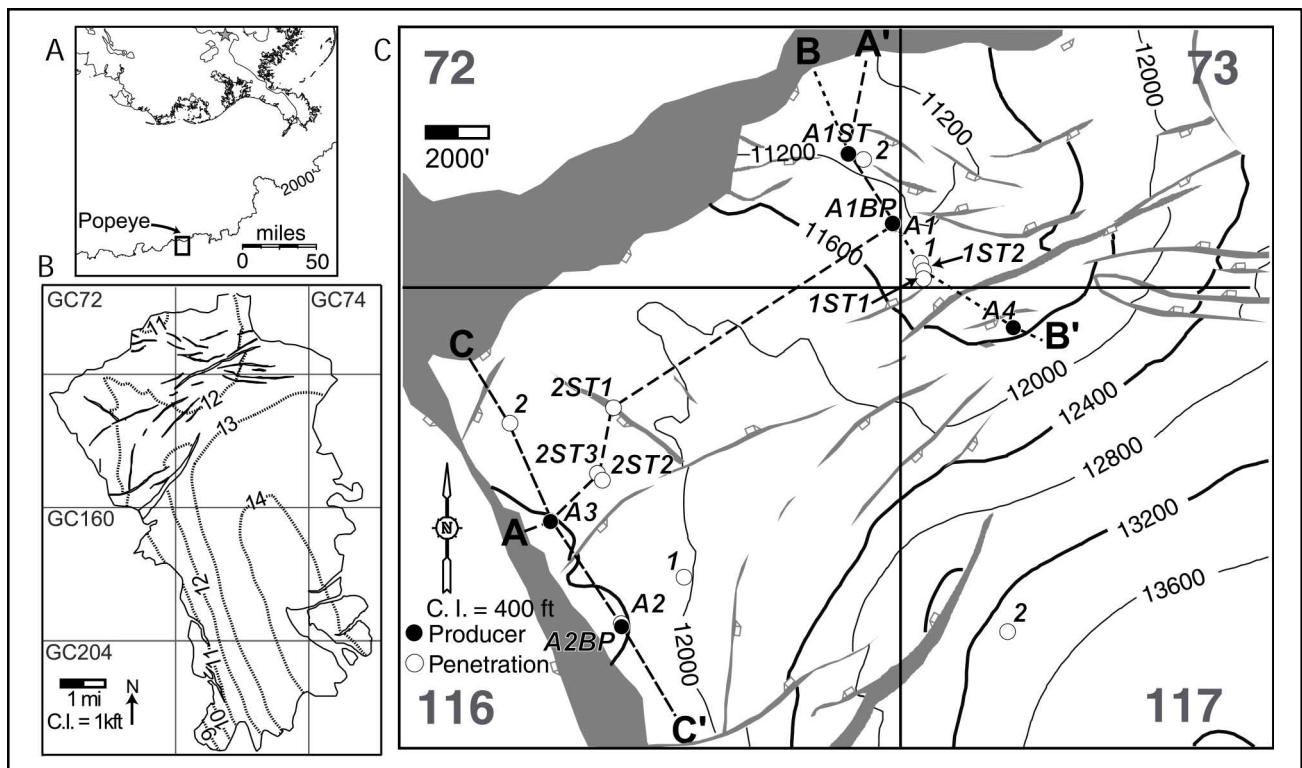
Figure 1: A) The Popeye field is located 140 miles southwest of New Orleans in 2000 ft of water. B) Structure map of vertical subsea depth (TVDSS) to the top of the G-sand in the minibasin. This map was created by mapping the trough minima of the G-sand reflector and depth-converting it using known penetration depths at well locations. C) Expanded view of structure map, focused on the Popeye field. Line A-A' is displayed on Figure 3; A-A', B-B', and C-C' are displayed on Figure 7.

by integrating seismic, well, core and production data. These analyses served as a foundation for reservoir simulations. At Mensa, integration of engineering data into reservoir simulations further refined the geologic model (e.g. Pfeiffer et al., 2000).

This study incorporates geological, geophysical and engineering data to characterize the G-sand reservoir at Popeye. The reservoir is complicated by lithologic variation, fault compartmentalization and an erosional channel. Reservoir simulations are used to refine our geologic model and identify a volume of bypassed reserves. Modification of uncertain geologic properties affects the producibility of these reserves.

GEOLOGIC OVERVIEW

Regional Setting

Popeye is a subsea development located in Green Canyon Blocks 72, 73, 116 and 117 (Fig. 1). It is in the northern, proximal, part of a larger minibasin (Figs. 1B, 1C) that includes the Genesis field (GC 205/161) on the western flank of the minibasin (Varnai, 1998; Rafalowski et al., 1994). Gas and condensate are produced from the late Pliocene (Fig. 2) G-sand reservoir, at 11,500 ft (3505 m) depth (Fig. 1). Production from the four G-sand reservoir compartments (RN and RM in the west, RA and RB in the northeast) (Fig. 3) is tied back to the Cougar platform in South Timbalier Block 300, 24 miles (38.6 km) to the north.

The Popeye field is situated between a salt-stock system to the west and an extensional salt tongue to the east (Weimer et al., 1998). The field is on the southern downthrown side of a regional growth fault (Fig. 3). The RM and RN reservoirs are bounded on the west by a normal fault that dips to the southwest. Smaller faults and a channel compartmentalize the G-sand into four reser-
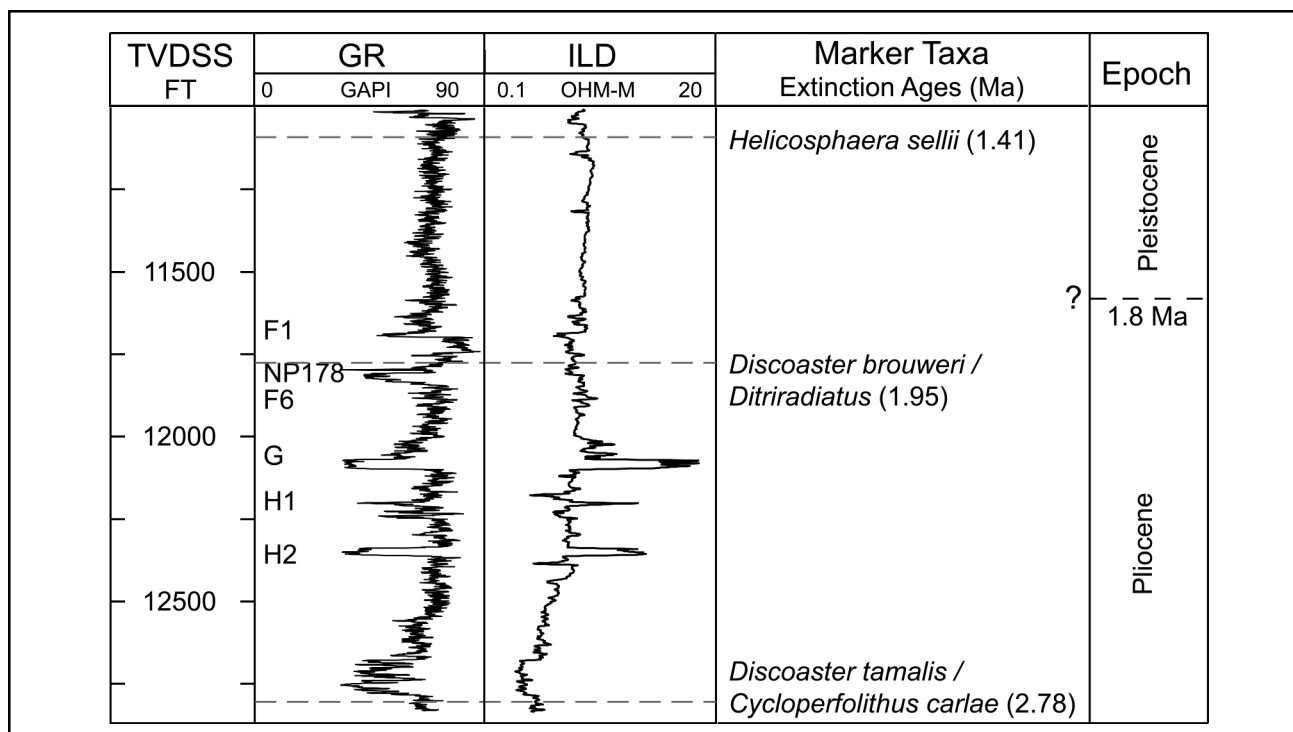
Figure 2: Gamma-ray (GR) and resistivity (ILD) logs for the 116-1 well (located in Figure 1). Biostratigraphic markers and correlated extinction ages (Styzen, 1996) are shown. The projection of the Pliocene-Pleistocene boundary is estimated.

voirs (Fig. 3). Large negative amplitudes delineate gas accumulations in the structural highs of these compartments; the gas-water contacts (GWCs) are generally parallel to depth-structure contours (Figs. 3, 4).

The G-Sand

Well-log data reveal that the G-sand reservoir consists of laminated facies (G_L) and an underlying massive facies (G_M) that averages 75 ft (22.9 m) in gross thickness (Fig. 5). The G_L is a very fine-grained, high porosity sandstone that is interbedded with silty shale (Fig. 5; Table 1). The G_M is a fine-grained, clean sandstone with no internal structure and moderate sorting (Table 1). It has a clean, blocky log signature with a sharp base (Fig. 5).

Table 1. G_L and G_M Rock Properties

Facies	Bedding	Net-to-Gross (%)	Sand Grain Size	Sand Porosity (%)	Sw (%)
GL	cm scale beds	11 - 79	very fine	25 - 30	13 - 40
GM	massive	88 - 100	fine	30 - 35	6 - 15

The G_L is mostly shale in the RN reservoir and has the most sand in the RA reservoir (Fig. 5). The G_L in the RM compartment becomes sandier with depth, indicated by a ramped log signature (Fig. 5B). Across much of the RA compartment, the G_L is capped by a clean, 10-ft sand (Fig. 5, red arrow). Beneath this sand, the G_L also has a ramped signature (Fig. 5C). Velocity and density are highest where the G_L is shaliest (RN) (Fig. 5A) and lowest where the G_L is sandiest (RA) (Fig. 5C). As a result, the G_L has the highest acoustic impedance in the RN reservoir, is intermediate in the RM reservoir, and is lowest in the RA reservoir.
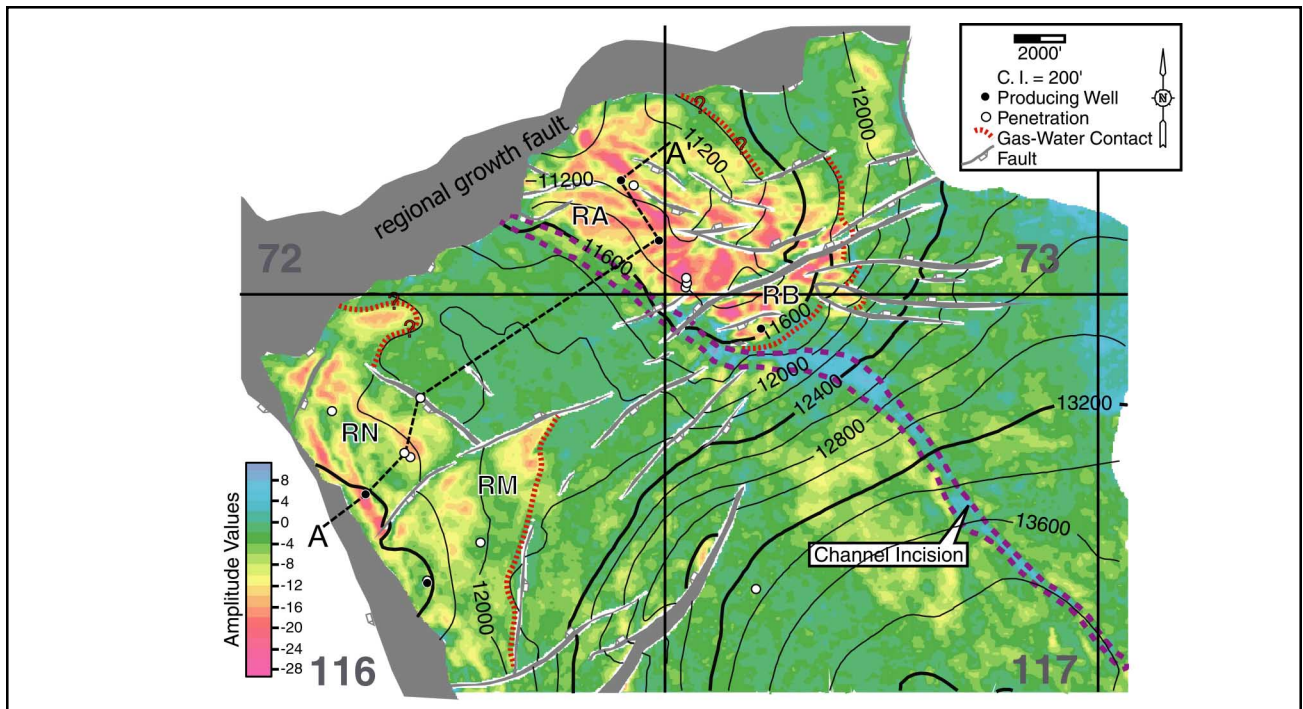
Figure 3: The amplitude of the G-sand trough with contours of the depth (TVDSS) to the top of the G_L.
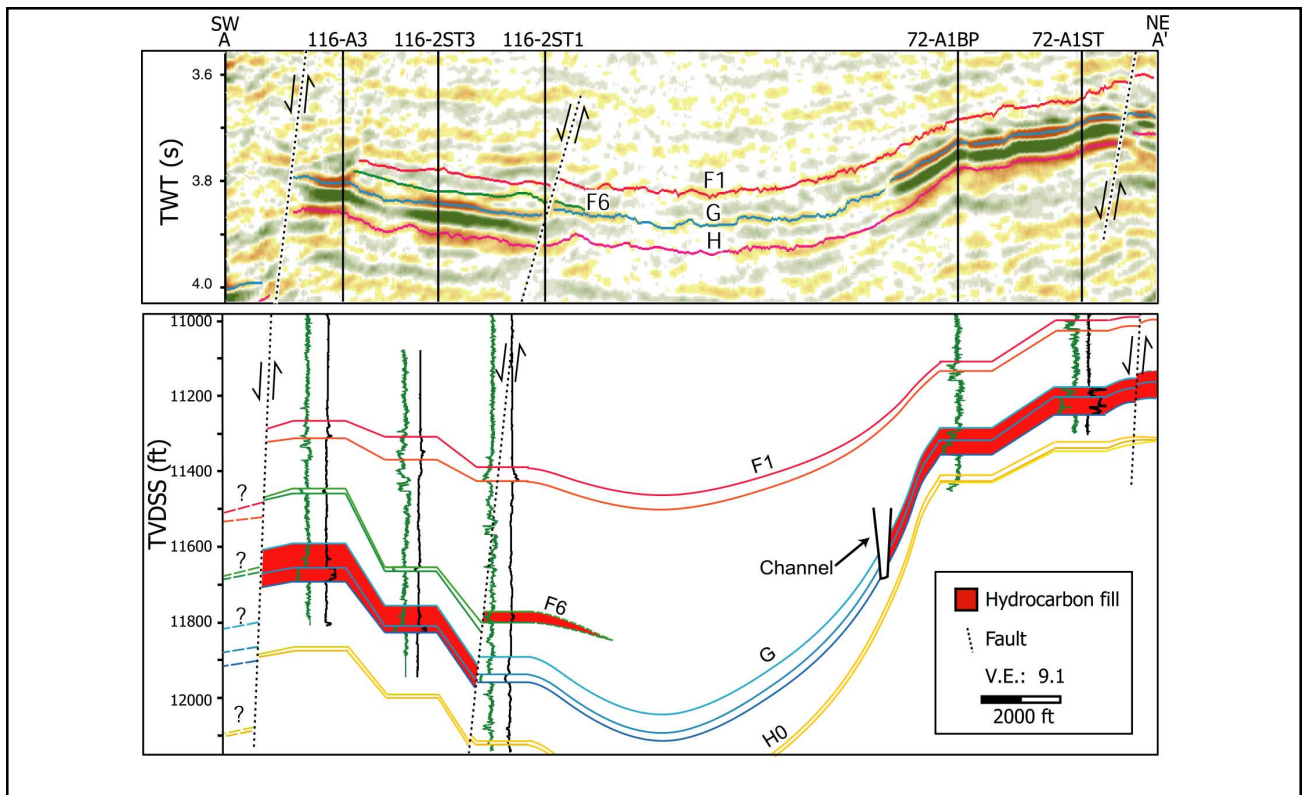
Figure 4: A) Seismic cross-section A-A' (located in Figure 1). Reds are negative values (troughs) and blues are positive values (peaks). The aquifer area between the RN and RA reservoirs exhibits a chaotic, discontinuous, low amplitude response. The H0, H1, and H2 sands cannot be distinguished in seismic data and are mapped as the H-group sands. B) Structural cross-section along A-A'. The erosional channel is the western limit of gas accumulation in the RA/RB reservoirs.
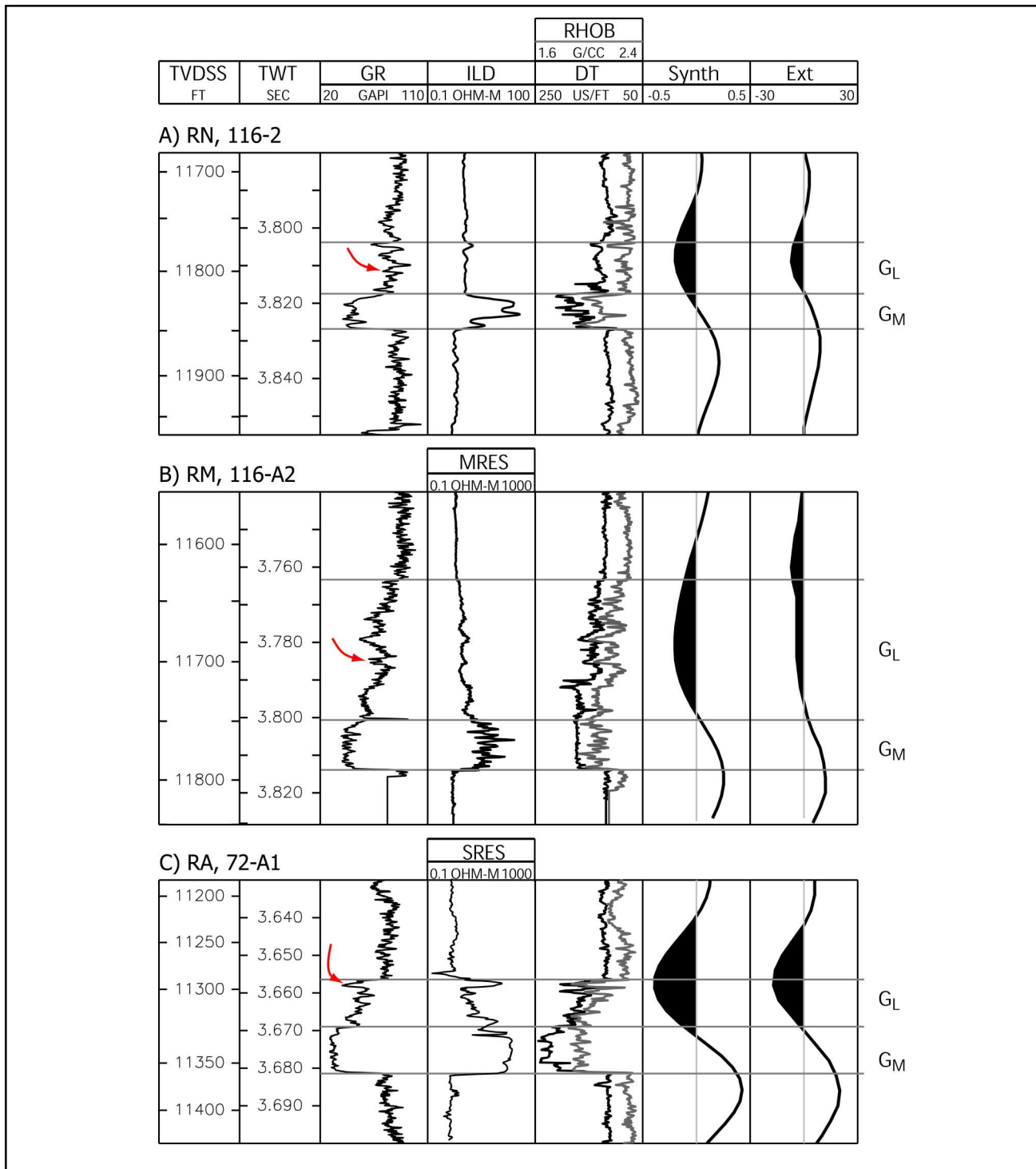
Figure 5: Seismic and log response (located in Figure 1C) in each compartment. The synthetic (Synth) and extracted (Ext) seismograms are zero-phase and were created with a 12-Hz Ricker wavelet. The extracted seismograms were shifted up 46 ms at well 116-2, 116 ms up at well 116-A2, and 58 ms up at well 72-A1 relative to the synthetic seismograms, due to poor velocity control. The correlatable sand body discussed in text is identified by red arrows on GR log. A) The G_L is not imaged in the RN reservoir. B) In the RM compartment, the trough is broad and asymmetric. C) The entire G-sand is imaged with a strong trough at the top and a strong peak at the base.

The relationship between seismic loop and sand geometry varies across the field. In the RN reservoir there is little impedance contrast between the G_L and the overlying shales, and a strong contrast between the G_L and G_M (Fig. 5A). As a result, the G_L is not seismically imaged and the G_M drives the seismic response. The G_M is also below tuning thickness (~80 ft or 24 m), so the seismic trough is above the top of the G_M and the seismic peak is below the G_M base. In the RM compartment, the thick G_L that shales upwards produces synthetic seismograms that show a broad, asymmetric trough whose minima is below the top of the G_L and a narrow peak that aligns with the base of the G_M (Fig. 5B). Although the RM reservoir has more sand in the G_L than the RN reservoir, amplitudes of the RN and RM reservoirs are comparable. The RA reservoir has the greatest impedance contrast between the G_L and the overlying shales due to the capping sand, and the smallest impedance contrast between the G_L and G_M (Fig. 5C). Seismograms in the RA show symmetric troughs that align with the top of the G_L and peaks that align with the base of the G_M. The RA compartment has the most negative amplitudes in the field.

No simple correlation between seismic attributes (e.g. amplitude and loop thickness) and log properties (gross thickness, net thickness, and net-to-gross ratio) of the G-sand or its individual facies was found. The only general trend is that the thick, clean sands of the RA compartment have brighter amplitudes. As a result, there was no consistent way to use seismic attributes to map the thickness or quality of the G-sand away from the well penetrations.

Repeat formation tests (RFTs), taken prior to production, were used to characterize Popeye reservoir pressures (Fig. 6). Gas-phase pressures were extrapolated vertically from their well locations along a gas gradient (0.13 psi/ft, 5.7 MPa/m) to each components GWC and reservoir crest. Pressures within the aquifer were assumed to follow a hydrostatic gradient (0.465 psi/ft, 20.5 MPa/m) with the water pressure equal to the gas pressure at the GWC. The RA and RN water pressures are similar. In contrast, the RM aquifer pressures are approximately 150 psi (1.03 MPa) lower (Fig. 6). The pre-production RM pressures do not follow a gas gradient and we debate the quality of these data.
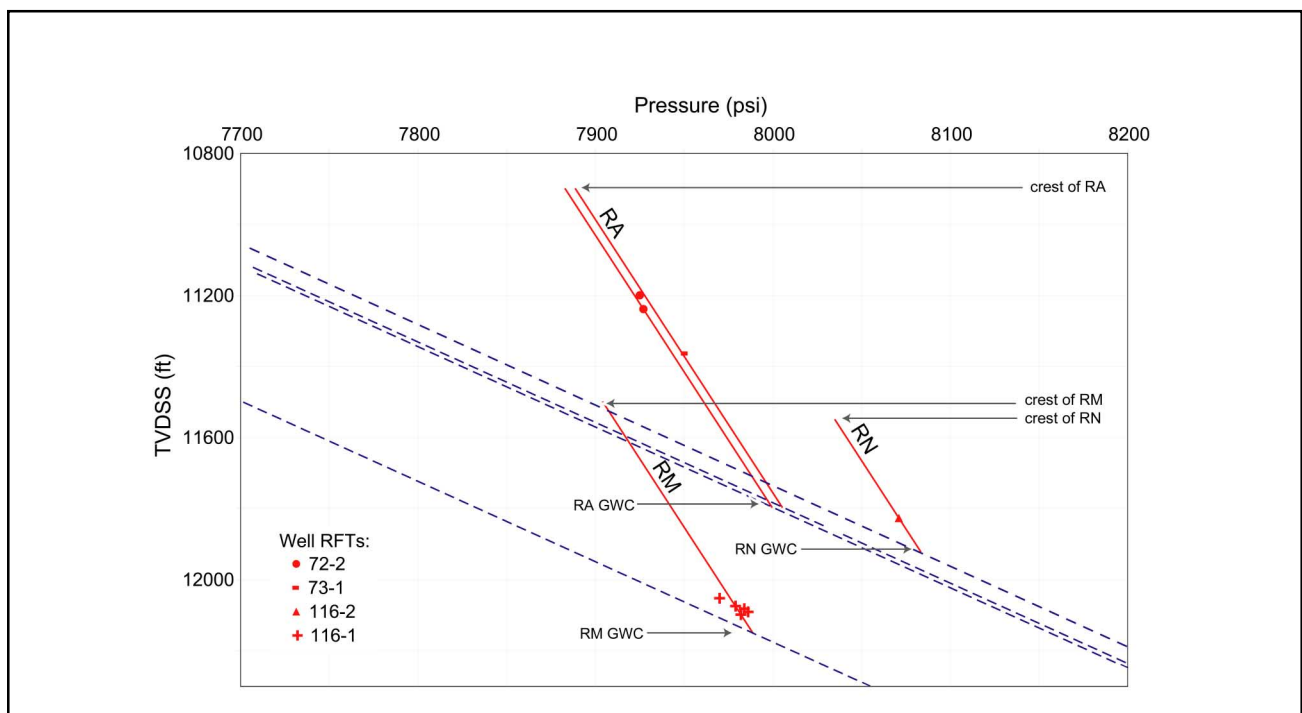
Figure 6: Initial pressures in the G-sand at Popeye. Gas pressures (red) and inferred aquifer pressures (blue solid lines) intersect at mapped GWCs. The RA and RN have similar aquifer pressures whereas the RM reservoir has a lower aquifer pressure.

GEOLOGIC OBSERVATIONS AND DEPOSITIONAL MODEL

The RA and RB reservoirs contain the thickest G_M deposits; the G_L is thickest in the southwest area of the field (Figs. 7, 8). The G_M is thickest along a northwest-southeast trend through the RA and RB reservoirs (Figs. 7A, 7B). The G_L thins from the southwest to the northeast decreasing away from the RM reservoir (Figs. 7C, 7D, 8A, 8C). In the RA reservoir, the G_M has the lowest gamma-ray values, velocity, density, and the brightest amplitudes (Fig. 5C), which indicate the G_M is cleaner here than elsewhere in the field.
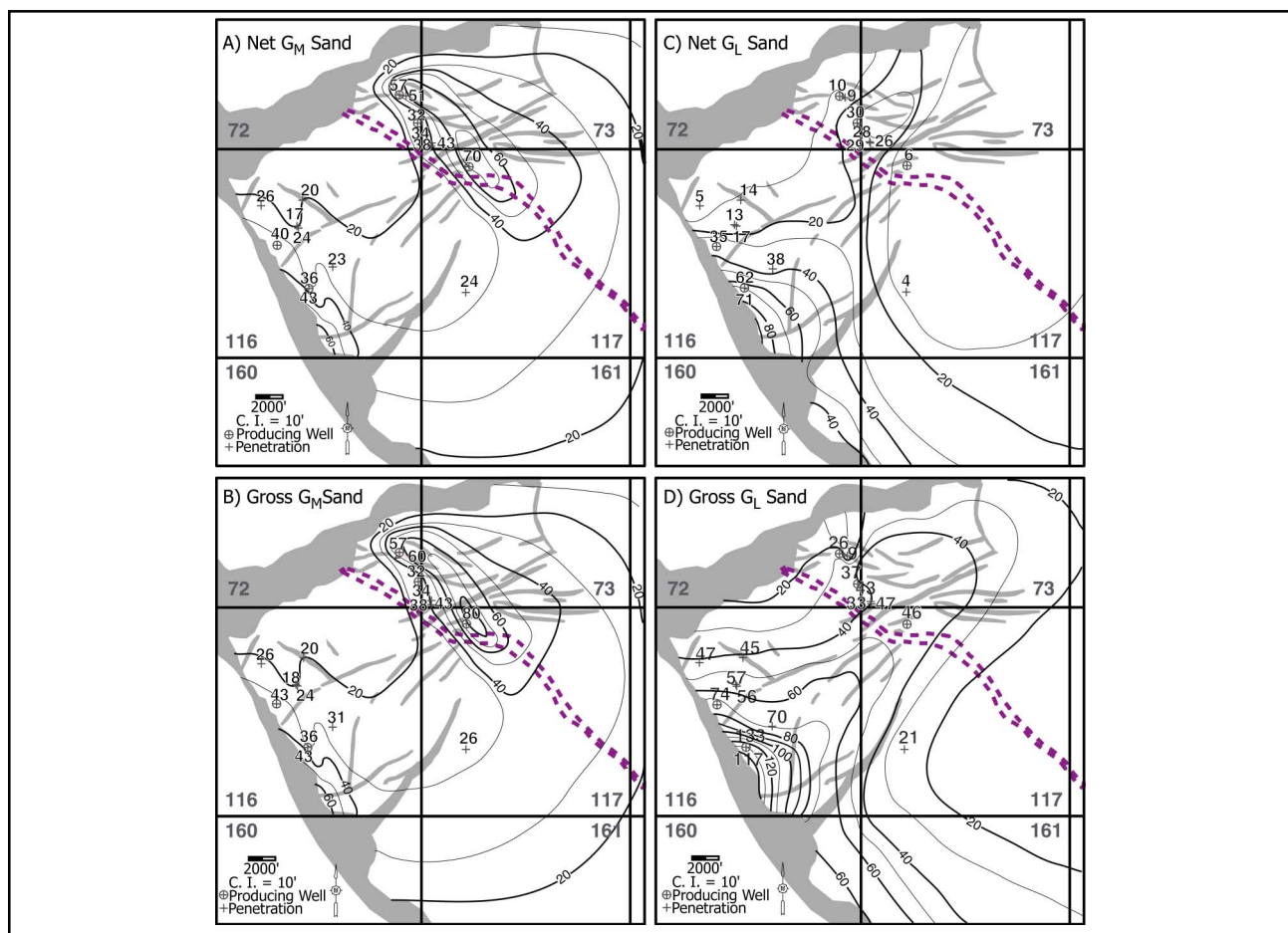
Figure 7: Net and gross G-sand thicknesses based on well data, seismic reflection character and depositional model. A and B) Net and gross G_M distributions are similar due to the high G_M net-to-gross ratio. C and D) Thickest net and gross G_L are located in the RM reservoir.

A sand body is correlated across the RA, RN, and RM reservoirs within the G_L facies (Figs. 5, 8). This sand is observed at the top of the G_L within the RA reservoir, and is thinner and located in the middle of the G_L in the RM and RN reservoirs (Figs. 5, 8). The G_L below this sand body has constant thickness from northeast to southwest across the field (Fig. 8A).

Due to the variability of seismic attributes in relation to G_L and G_M thickness and sand quality, sand distribution maps were largely based on well penetration information, a depositional model, and general trends in the seismic response. The lithologic and pore fluid variations of the G-sand and resulting seismic response are reflected in map view (Fig. 3). Aquifer regions contain small amplitudes with coherent reflections south of the RB and RM compartments. However, the aquifer region between the RA and RN reservoirs has a chaotic, discontinuous seismic reflection (Fig. 4). The G-sand seismic loop thins, amplitudes decrease, and the reflection becomes less continuous down to the south and east in the minibasin.

Positive amplitudes (Fig. 3) show a small channel of different lithology running through the center of the field. This indicates the channel was filled by sediments post-dating the G-sand with higher acoustic impedance properties. A seismic reflection isochron map between the G-sand and the underlying H-Sands reveals the geometry of a channel within the G-sand entering the basin south of the RM reservoir, oriented northwest southeast (Fig. 9).

Interpretation

The difference in sand thickness trends between the G_M and G_L are interpreted to record two different depositional mechanisms. Gravity flows at G-sand time entered the basin north of well A1ST and deposited thick sheet sands (Figs. 10, 11). We infer low-relief bathymetry within the slope accommodation space slowed gravity flows, depositing sand while finer-grained sediments continued downslope. The localized linear pattern of the thickest G_M occurrences (Figs. 7A, 7B) indicates that the G_M was deposited in a bathymetric low, produced either by erosion from prior flows or the flows themselves. Abrupt changes in local gradients, such as the northern growth fault (Fig. 3), have been shown to cause incision and flow confinement (Friedmann et al., 2000).

After the local accommodation space was filled with the G_M, sediment entry into the minibasin changed. The G_L was deposited by levee-overbank sedimentation from the channel south of the RM reservoir and by channels traveling through the central part of the field (Figs. 7, 11). The chaotic nature of the G-sand reflection indicates that post-depositional erosion of the G_M by channels bypassing this area disrupted sand continuity (Figs. 10, 11). The vertical position of the correlatable sand within the G_L (Fig. 8) indicates that overbank sedimentation from the channel south of the RM reservoir provided the last significant G_L deposits in the Popeye area (Figs. 8, 11).

Features interpreted at Popeye are consistent with nearby fields and regional trends. The Genesis field, seven miles south of Popeye, contains sinuous, elongate channels that trend northwest to southeast in reservoir sands (Rafalowski et al., 1994), indicating a consistent sediment transport direction through this area. Winker and Booth (2000) describe how in a proximal, typically bypass facies assemblage area of a minibasin, ponded sediment such as the G_M can accumulate. A small change in relief south of the Popeye reservoir area induced sand to drop from gravity flows, depositing the G_M (Fig. 10). Once slope equilibrium was reached, levee deposits covered the area forming the G_L.

Prather et al. (1998) suggests that a lithologic transition analogous to the G_M-to-G_L change records the natural fill progression of accommodation in a slope minibasin. Alternatively, a eustatic interpretation suggests that rapid sea level fall forced erosion of the shelf, sourcing the turbidite sheet sands on the continental slope. This is followed in late lowstand by deposition of finer sediments in channel-levee complexes (Posamentier et al., 1991; Carminatti and Scarton, 1991).

PRODUCTION HISTORY

Production from Popeye began in January 1996 from wells A1BP and A2BP. As of June 2003, the field produced 329 billion cubic feet (BCF) of gas from 5 wells. The A3 well went online in January 1998, has produced 68 BCF, and currently produces 20 million standard cubic feet per day (MMSCF/D) (6/25/03). The A1BP well was shut-in due to completion problems in January 1999 after producing 47 BCF. It was replaced by well A1ST which produces 59 MMSCF/D (6/25/03) and has produced 75 BCF (6/25/03). In April 2002, the A2BP well was shut-in due to water production; it produced 125 BCF. At this time the A4 well came online, now producing 29 MMSCF/D (6/25/03) with cumulative production of 17 BCF (6/25/03).

RESERVOIR SIMULATION

Base-Case Model Description

A three-dimensional, compositional reservoir simulator is used to match production and pressure data. The G_L and G_M are represented by separate layers; each layer has its distinct and constant

rock properties (Table 2), relative permeability curves, and is divided into 10,000 grid blocks. Layer thicknesses are derived from Figure 7, structural geometry from Figure 3, and relative permeabilities from a database constrained by absolute permeability and fluid type. Core experiments provide capillary curves, used to determine initial water saturations (Fig. 13B) and a compaction model (Ostermeier, 1993; Ostermeier, 2001).

Table 2. Constant Property Values Assigned to Simulation Layers in Reservoir Model.

Layer	Porosity (%)	k_h (mD)	k_v (mD)	Sw_{irr}	Sg_r	Initial Compressibility (1/psi)
G_L	25	500	0.1	0.143	0.021	$22.21*10^{-6}$
G_M	30	1200	500	0.119	0.022	$22.21*10^{-6}$

The four hydrocarbon compartments are assumed to be in pressure communication through a common down-dip aquifer (Fig. 6). The G-sand is represented by six equalization regions composed of four reservoir compartments and two aquifer regions, each with different initial compositions, PVT properties, and GWCs (Fig. 13A).   Grid boundaries and faults are assumed to be impermeable (Figs. 13A, 13B).

An Equation of State (EOS) model is created for each reservoir compartment based on fluid samples taken from producing wells. These EOS models are simplified into a set of six pseudo-components whose properties are varied to match the behavior of the original fluid samples in PVT experiments, using a process similar to that of Coats (1985).

The history match for the field is based on bottom-hole pressures, daily production rates, and cumulative production. History matching was an iterative process of modifying the geologic model, the GWCs, and aquifer support. The historical data are matched for the field, with the gas rates specified (Fig. 12).

The reservoir model is used to predict future well performance. The most intriguing result of the base-case simulation is that a pocket of gas will not be produced south of the A1ST well in the RA reservoir (Fig. 13C). The A1ST well is offset 900 ft (274 m) southwest and 80 ft (24 m) deeper than the crest of the RA anticline. A cluster of faults is oriented parallel to the anticline; these faults slow fluid flow through the area which causes the development of two primary flow paths (Fig. 13A). Pathway A develops just up-dip from the RA-RB bounding fault and Pathway B is north of the fault cluster. In this initial simulation, Pathway B dominates and well A1ST waters out before the gas, structurally beneath the well, is produced (Fig. 13C).

Modifications of the Base-Case Model

Simulations were performed to understand how 1) flow path constriction into the RA reservoir, 2) aquifer thickness, and 3) channel permeability, affect the drainage behavior. Each of these properties was varied and history matches were obtained, allowing for comparisons of unproduced reserves in the RA reservoir. Pathway A runs between the two faults that separate the RB and RA reservoirs (Fig. 13A, purple arrow). If the separation of these two faults is increased, then aquifer support to the RA reservoir is increased and flow along Pathway A dominates (Fig. 13A). As a result, more of the gas pocket is produced by the present well than in the base case scenario (Table 3). If the thickness of the northeast portion of the RA reservoir, represented by a dim amplitude area, (Figs. 3, 13) is decreased by 50%, the flow along Pathway B is reduced and more of the gas pocket can be produced by the present wells (Table 3). Finally, if the channel west of the RA reservoir is only partially sealing (transmissibility multiplier of 0.01) there is added water drive from the west. This eliminates the pocket of bypassed reserves south of the A1ST; reserves remain north of the A1ST well (Table 3).

Table 3. Difference in RA Reservoir Production for Simulations with Uncertain Reservoir Properties.

Simulation	Initial Gas Volume in RA Reservoir (MMSCF)	Production from RA Reservoir	Difference (MMSCF)
Base Case	304,867	219,989	84,887
Fault Separation Increase	304,867	224,963	79,913
Decrease in RA Aquifer Thickness	285,698	227,773	57,925
Channel Transmissibility Increase (*0.001)	304,867	218,959	85,917

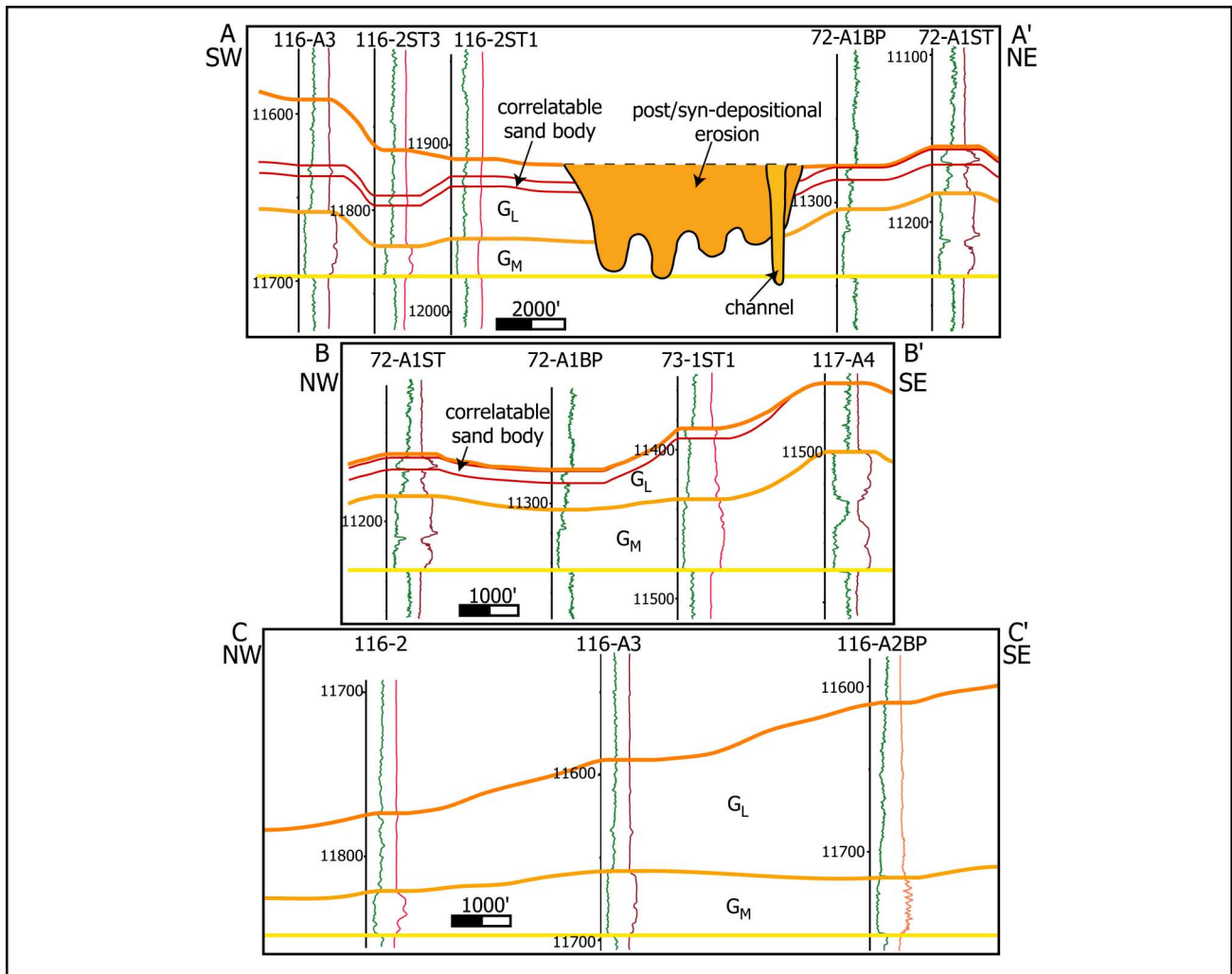*Figure 8: Stratigraphic cross-sections flattened to the G-sand base. A) G_L thickens to the southwest, closer to the channel that sourced levee deposits. B) Although well 72-A1ST is closest to sediment-entry point, the thickest G_M accumulations occur in RB, possibly due to preexisting bathymetry. C) G_L deposits thicken towards the channel that enters basin south of RM reservoir. Sections are located in Figure 1.*
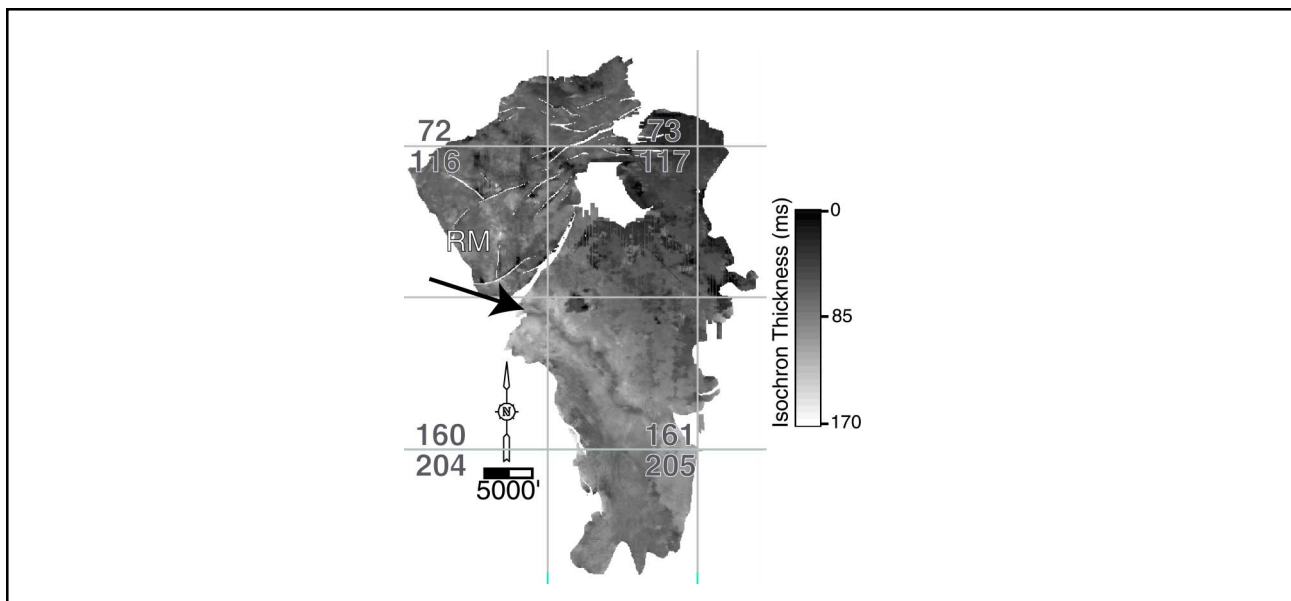
Figure 9: Isochron map in two-way time (ms) between the G-sand and underlying H-sands. A channel bypassing the Popeye area at G-sand time enters the basin south of the RM reservoir, providing significant G_L sediments to the RM reservoir.
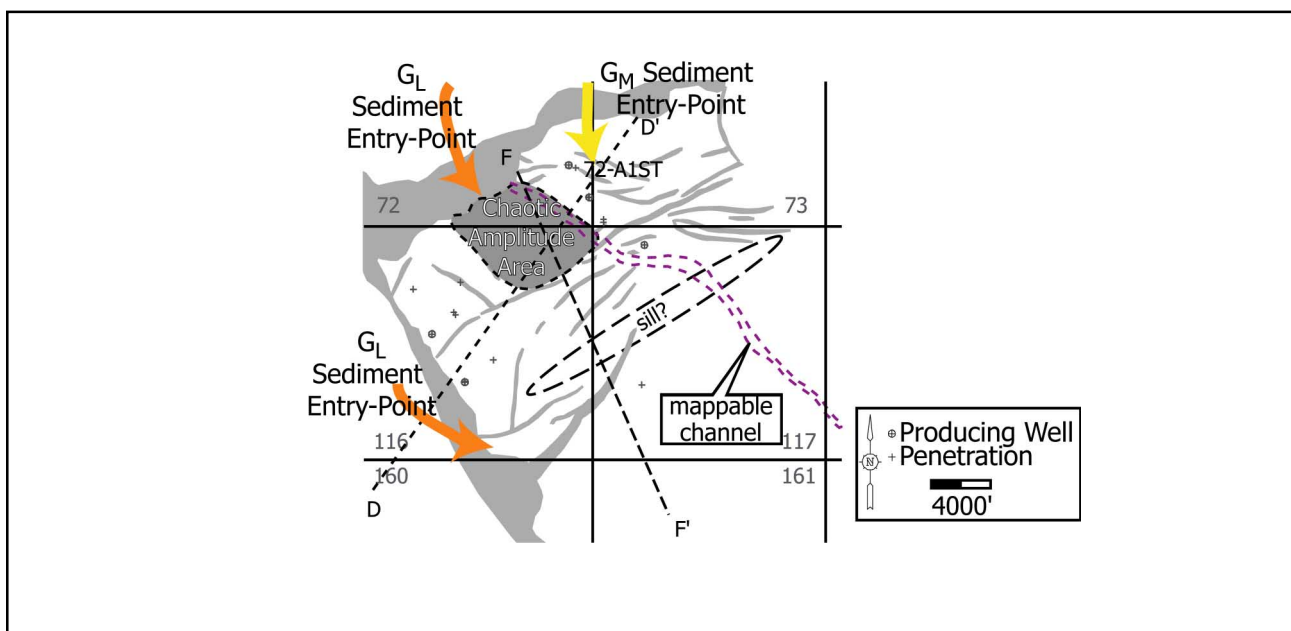
Figure 10: Interpreted features of the G-sand. The colored arrows identify sediment-entry points in our depositional model.

These simulations illustrate that uncertainty in the geologic model propagates to uncertainty in reservoir performance. Simulations show that future pressure measurements from well A1ST should distinguish between the four simulation scenarios, however, the down-hole and tubing head pressure gauges have failed and a special effort would be required to obtain these data. In addition, a more detailed analysis of fault throw might be used to better constrain zones of fault imperme-ability. Unfortunately, there are no well penetrations in the aquifer east of the RA to better constrain the thickness. Finally, while it is geologically reasonable that the channel is impermeable, further investigation using time-lapse seismic or well test analysis might verify fluid displacement and determine the permeability of the channel.
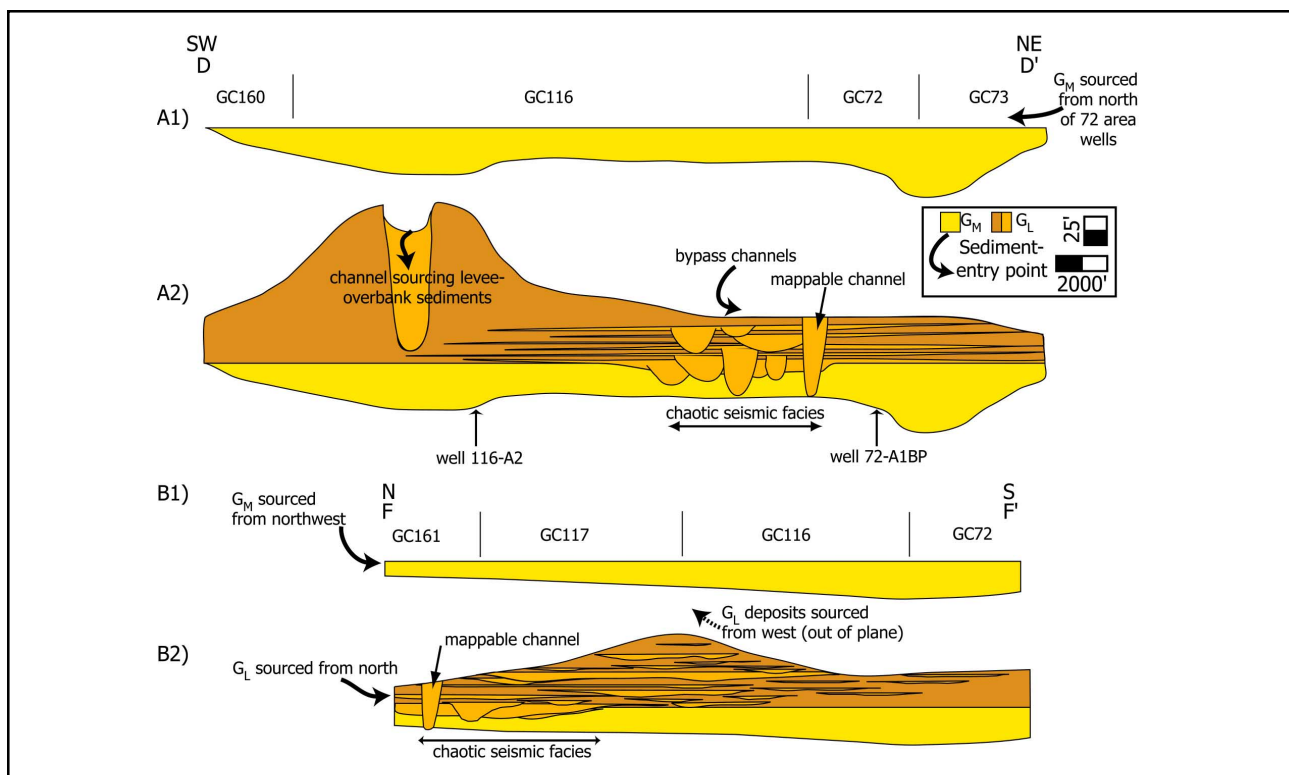
Figure 11: Model of G-sand deposition, in strike view (A, B) and dip view (C, D). A, C) Sediment enters basin as sheet flows from an area north of well 72-A1ST (Fig. 10). Successive flows into the basin amalgamate, forming the G_M. B, D) The sediment-entry point switches to the central portion of the field and channels bypass the Popeye area. Levee deposits accumulate across the field, thickest in the southwest. Bypassing channels incise deposits and create a chaotic seismic signature. Sediment input ends and the G-sand is capped by mud. The locations of cartoon cross-sections are in Figure 10.

Figure 12: History match for the Popeye field from January 1996 to December 2002.

Figure 13: A) Equalization regions and boundary conditions for the Popeye reservoir simulator. The hydrocarbon bear regions are 1, 2, 4, and 5; 3 and 6 are aquifer regions. B) Initial gas saturation in the G_M layer (01/01/1996). Initially there is 761 BCF gas in place. C) Final gas sa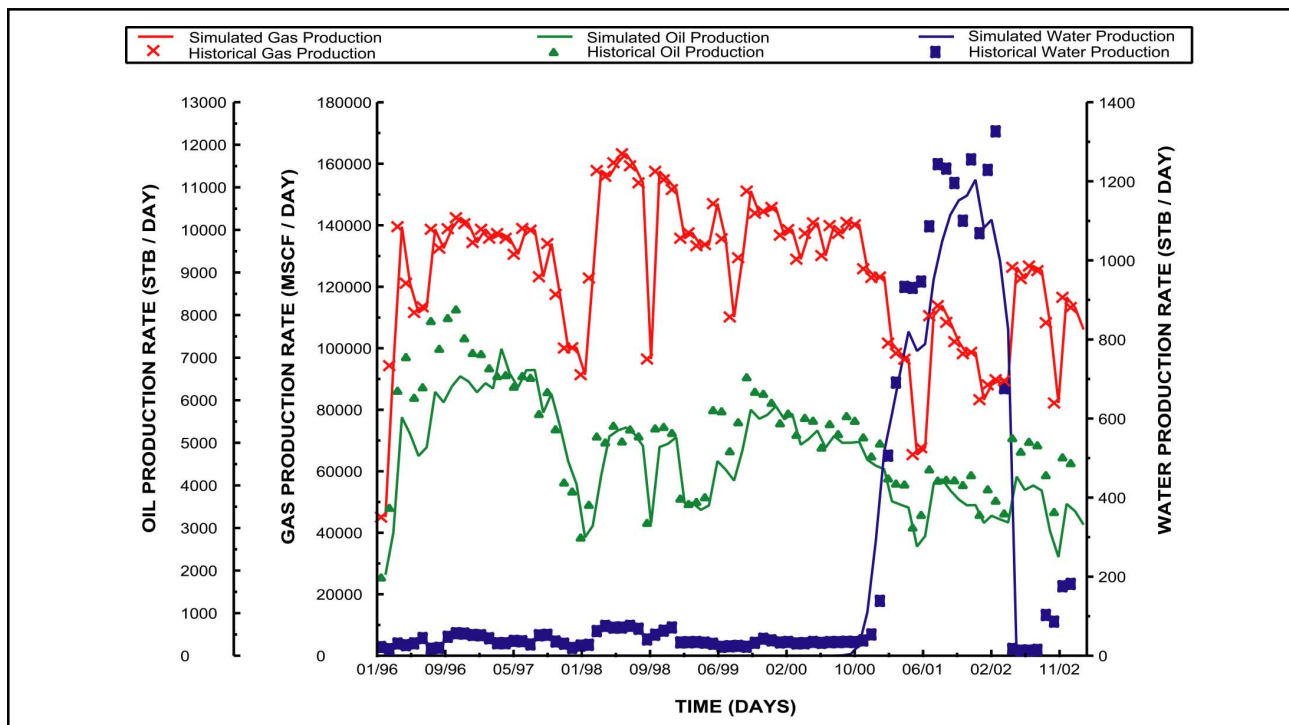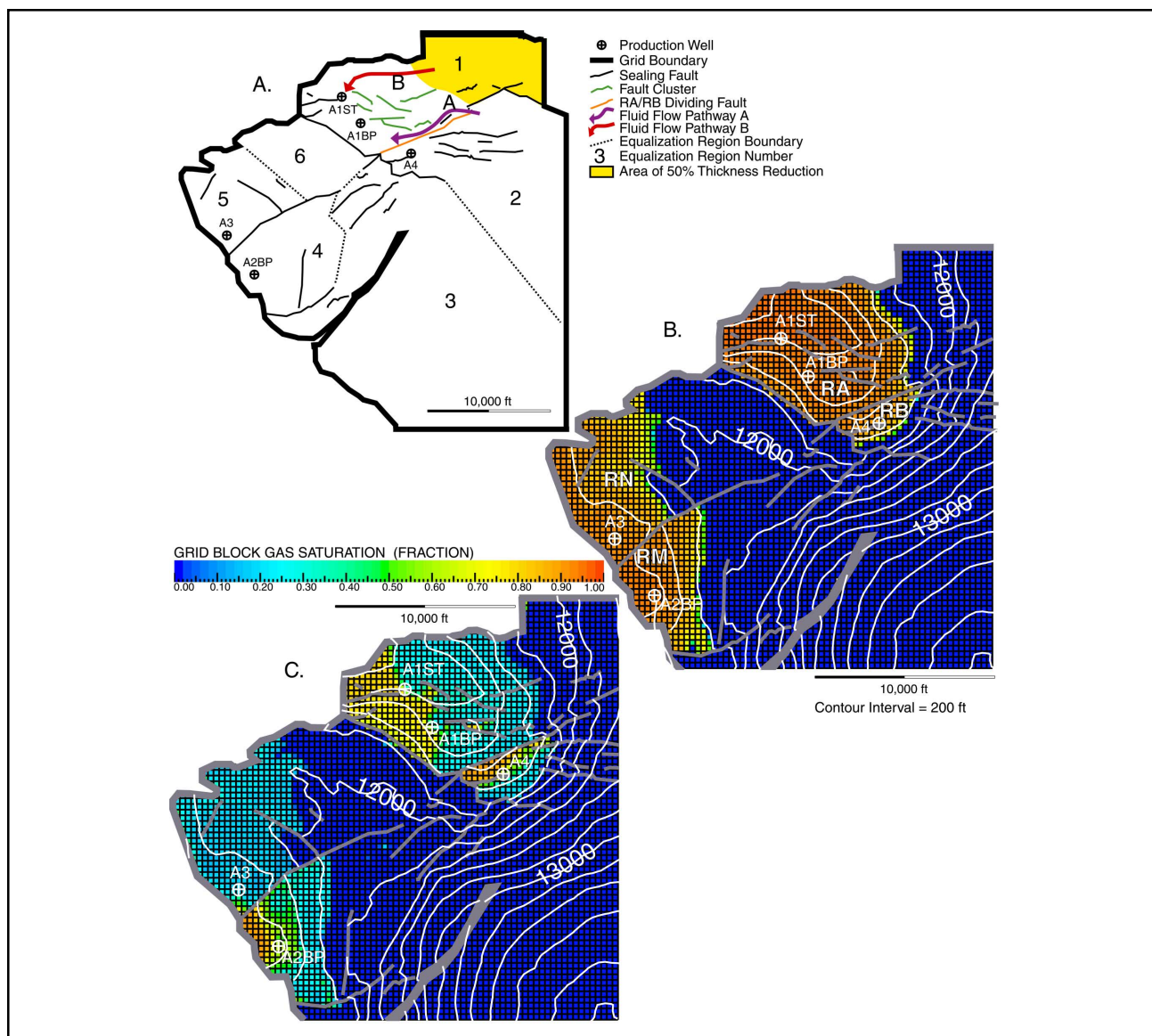turation of the G_M layer using the current producing wells (09/01/2001). Notice the pocket of non-produced hydrocarbons to the west and south of the A1BP well.

CONCLUSIONS

Well log, engineering, and seismic data were integrated to develop a depositional model. The massive facies (G_M) was deposited by gravity flows that entered the basin north of the RA reservoir. These amalgamated sheet sands were overlain by laminated sands (G_L) and silts deposited by levee-overbank sedimentation from bypass channels. This depositional model provides constraints for the sand distribution interpretations used in reservoir simulations.

The base-case reservoir simulation results in a volume of bypassed reserves within the RA reservoir. The simulated location and amount of unrecovered reserves can differ based on the modeled fault separation between the RA and RB reservoirs, RA aquifer volume, and channel transmissibility. Expanding the distance between the two faults separating the RA and RB reservoirs or decreasing the RA aquifer volume increases the volume of bypassed reserves, while in-

creasing the channel permeability changes the location of unrecovered reserves. These reasonable variations in the geologic model significantly influence reservoir drainage behavior.

ACKNOWLEDGMENTS

REFERENCES

Booth, J., DuVernay III, A., Pfeiffer, D., and Styzen, M., 2000. Sequence stratigraphic framework, depositional models, and stacking patterns of ponded and slope fan systems in the Auger basin: central Gulf of Mexico slope: GCSSEPM Foundation 20th Annual Research Conference, Deep-water Reservoirs of the World, p. 82-103.

Carminatti, M. and Scarton, J. C., 1991. Sequence stratigraphy of the Oligocene turbidite complex of the Campos Basin, offshore Brazil: An overview, in Weimer, P. and Link, M. H., eds., Seismic Facies and Sedimentary Processes of Submarine Fans and Turbidite Systems: New York, Springer-Verlag, p. 241-246.

Coats, K. H., 1985. Simulation of gas condensate reservoir performance: Journal of Petroleum Technology, vol. 37, no. 11, p. 1870-1885.

Diegel, F.A., Karlo, J. F., Schuster, D. C., Shoup, R. C., and Tauvers, P. R., 1995. Cenozoic structural evolution and tectonostratigraphic framework of the northern Gulf Coast continental margin, in Jackson, M. P. A., Roberts, D. G., and Snelson, S., eds., Salt Tectonics: A Global Perspective: Tulsa, OK, AAPG, p. 109-151.

Elsayed, S. A., Baker, R., Churcher, P. I., and Edmunds, A. C., 1993. Multidisciplinary characterization and simulation study of the Weyburn Unit: Journal of Petroleum Technology, vol. 45, no. 10, p. 930-934, 973.

Friedmann, S. J., Beaubouef, R. T., Pirmez, C., and Jennette, D. C., 2000. The effects of gradient changes on deep-water depositional systems: an integrated approach: AAPG 2000 annual meeting, vol. 2000, p. 51.

Holman, W. E. and Robertson, S. S., 1994. Field development, depositional model, and production performance of the turbidic "J" sands at Prospect Bullwinkle, Green Canyon 65 fields, outer-shelf Gulf of Mexico, in Weimer, P., Bouma, A. H., and Perkins, B. F., eds., Submarine Fans and Turbidite Systems—Sequence Stratigraphy, Reservoir Architecture, and Production Characteristics: GCSSEPM, 15th Annual Research Conference, p. 139-150.

Lerch, C. S., Bramlett, K. W., Butler, W. H., Scales, J. N., Stnd, T. B., and Glandt, CA., 1996. Integrated 3D reservoir modeling at Ram-Powell field: A turbidite reservoir in the eastern Gulf of Mexico: Proceedings— SPE Annual Technical Conference and Exhibition, vSigma, p. 477-492.

Mahaffie, M. J., 1994. Reservoir classification for turbidite intervals to the Mars discovery, Mississippi Canyon 807, Gulf of Mexico, in Weimer, P., Bouma, A. H., and Perkins, B. F., eds., Submarine Fans and Turbidite Systems—Sequence Stratigraphy, Reservoir Architecture, and Production Characteristics: GCSSEPM, 15th Annual Research Conference, p. 233-244.

McGee, D. T., Bilinski, P. W., Gary, P. S., Pfeiffer, D. S., and Sheiman, J. L., 1994. Geologic models and geometries of Auger field, deep-water Gulf of Mexico, in Weimer, P., Bouma, A. H., and Perkins, B. F., eds., Submarine Fans and Turbidite Systems—Sequence Stratigraphy, Reservoir Architecture, and Production Characteristics: GCSSEPM, 15th Annual Research Conference, p. 245-256.

Ostermeier, R.M., 1993. Deep-water Gulf of Mexico turbidites: compaction effects on porosity and permeability: SPE Formation Evaluation, vol. 10, no. 2, p. 79-85.

Ostermeier, R.M., 2001. Compaction effects on porosity and permeability: Deep-water Gulf of Mexico turbidites: Journal of Petroleum Technology, vol. 53, no. 2, p. 68-74.

Pfeiffer, D., Mitchell, B., and Yevi, G., 2000. Mensa, Mississipi Canyon block 731 field, Gulf of Mexico—an integrated field study: GCSSEPM Foundation 20th Annual Research Conference, Deep-water Reservoirs of the World, p. 756-775.

Posamentier, H. W., Erskine, R. D., and Mitchum Jr., R. M., 1991. Models for submarine-fan deposition with in a sequence stratigraphic framework, in Weimer, P. and Link, M. H., eds., Seismic Facies and Sedimentary Processes of Submarine Fans and Turbidite Systems: New York, Springer-Verlag, p. 127-136.

Prather, B. E., Booth, J. R., Steffens, G. S., and Craig, P.A., 1998. Classification, lithologic calibration and stratigraphic succession of seismic facies of intraslope basins, deep-water Gulf of Mexico: AAPG Bulletin, v.82, no. 5A, p. 701-728.

Rowan, M. and Weimer, P., 1998. Salt-sedimentation interaction, northern Green Canyon and Ewing Bank (offshore Louisiana), northern Gulf of Mexico: AAPG Bulletin, v. 82, no. 5B, p. 1055-1082.

Rafalowski, J. W., Regel, B. W., Jordan, D. L., and Lucidi, D. O., 1994. Green Canyon Block 205 lithofacies, seismic facies, and reservoir architecture, in P. Weimer and T. L. Davis, eds., AAPG Studies in Geology 42, Tulsa, OK, AAPG/SEG, p. 133-142.

Styzen, M., 1996. Late Cenozoic chronostratigraphy of the Gulf of Mexico: GCSSEPM Foundation, Houston, TX.

Varnai, P., 1998. Three-dimensional seismic stratigraphic expression of Pliocene-Pleistocene turbidite systems, northern Green Canyon (offshore Louisiana), Northern Gulf of Mexico: AAPG Bulletin, v. 82, no. 5B, p. 986-1012.

Weimer, P., Rowan, M. G., McBride, B. C., and Kligfield, R., 1998. Evaluating the petroleum systems of the northern deep Gulf of Mexico through integrated basin analysis: an overview: AAPG Bulletin, v. 82, no. 5B, p. 865-877.

Winker, C. and Booth, J., 2000. Sedimentary dynamics of salt-dominated continental slope, Gulf of Mexico: integration of observations from the seafloor, near-surface, and deep subsurface: GCSSEPM Foundation 20th Annual Research Conference, Deep-water Reservoirs of the World, p. 1059-1086.